Characterization of Nb_3Sn and Multilayer Thin Films for SRF Applications

Dissertation
zur Erlangung des Grades eines Doktors
der Naturwissenschaften

vorgelegt von
M.Sc. Sebastian Keckert

eingereicht bei der Naturwissenschaftlich-Technischen Fakultät
der Universität Siegen
Siegen 2019

Betreuung und Erstgutachten:	Prof. Dr. Jens Knobloch (Universität Siegen)
Zweitgutachten:	Prof. Dr. Ursula van Rienen (Universität Rostock)
Tag der mündlichen Prüfung:	03. März 2020
Promotionskommission:	Prof. Dr. Andreas Jankowiak (Humboldt-Universität zu Berlin) Prof. Dr. Wolfgang Kilian (Universität Siegen) Prof. Dr. Markus Risse (Universität Siegen)

Abstract

Basic R&D on materials for superconducting radio frequency (SRF) applications requires RF measurements on samples with high resolution. The Quadrupole Resonator (QPR) at Helmholtz-Zentrum Berlin is a dedicated test cavity, enabling RF characterization of samples in a wide parameter space of temperature and RF field strength at three frequencies. Thereby, the instrument covers typical real-life accelerator conditions without being limited to it.

Within the scope of this thesis, the QPR measurement capabilities were continuously expanded and improved, allowing calorimetric measurements of RF surface resistance at all three operating frequencies. Furthermore, magnetic penetration depth, critical temperature (T_c) and the RF critical field can be studied. From those directly measured values, superconducting and normal conducting quantities such as DC critical fields, Ginzburg-Landau parameter, mean free path and normal state resistivity can be derived, yielding a multi-parameter characterization of the investigated sample.

In this work, two superconducting coatings were characterized: One single layer of Nb_3Sn and a NbTiN on Nb multilayer structure. Nb_3Sn is one of the most promising alternative materials to niobium and already showed high quality factors in coated research cavities. The sample investigated here underscores the potential of this high-T_c material for low surface resistance. Ultimately, this could enable low-loss continuous-wave particle accelerators. However the SRF performance failed to reach theoretical values, presumably due to off-stoichiometric areas that were subsequently identified using surface analysis. Furthermore, the RF quench field measurement indicated practical difficulties in reaching the superheating critical field of Nb_3Sn with the current coating process.

Multilayer structures of superconducting thin films are expected to increase the superheating critical field of a bulk superconductor, corresponding to higher maximum achievable accelerating gradients. With the second sample characterized in this work, the theoretical descriptions of magnetic penetration depth and superheating field for multilayer structures can be confirmed. The observation of non-monotonic surface resistance as a function of temperature reveals additional contributions that are not included in current theories and opens a promising field for future studies.

Zusammenfassung

Grundlagenforschung an Materialien für supraleitende Hochfrequenzfeldanwendungen erfordert hochauflösende Messungen an Proben in Hochfrequenzfeldern. Der Quadrupolresonator (QPR) am Helmholtz-Zentrum Berlin ist ein spezialisierter Hohlraumresonator, der die Charakterisierung von Proben in einem großen Parameterraum von Feldstärke und Temperatur sowie bei drei Frequenzen ermöglicht. Damit deckt das Instrument typische Betriebsbedingungen von Teilchenbeschleunigern ab, ohne darauf beschränkt zu sein.

Im Rahmen dieser Arbeit wurden die Messmöglichkeiten des QPR kontinuierlich weiterentwickelt und ermöglichen nun die Messung des Hochfrequenzoberflächenwiderstands bei allen drei Betriebsfrequenzen. Außerdem können die magnetische Eindringtiefe, die Sprungtemperatur und das kritische Magnetfeld in Hochfrequenzfeldern untersucht werden. Von diesen Messgrößen können charakteristische Materialparameter sowohl für den supraleitenden als auch für den normalleitenden Zustand abgeleitet werden, wie z. B. kritische (statische) Magnetfelder, Ginsburg-Landau-Parameter, mittlere freie Weglänge und elektrische Leitfähigkeit.

In dieser Arbeit wurden zwei supraleitende Beschichtungen charakterisiert: Eine einzelne Nb_3Sn-Schicht sowie eine mehrlagige Struktur aus NbTiN und Nb. Nb_3Sn ist derzeit die vielversprechendste Alternative zu Niob und beschichtete Testkavitäten haben schon hohe Resonanzgüten demonstriert. Die in dieser Arbeit untersuchte Probe unterstreicht das Potential dieses Supraleiters mit vergleichsweise hoher Sprungtemperatur für kleine Oberflächenwiderstände. Perspektivisch können dadurch verlustarme Dauerstrichbeschleuniger ermöglicht werden. Allerdings wurden bei dieser konkreten Probe nicht-stöchiometrische Bereiche mittels Oberflächenanalyse festgestellt, die die supraleitende Leistungfähigkeit limitieren. Außerdem weist die Messung des Hochfrequenzquenchfelds auf praktische Schwierigkeiten in der Erreichbarkeit des überhitzten kritischen Magnetfelds von Nb_3Sn mit dem aktuellen Beschichtungsprozess hin.

Mehrlagige Strukturen aus dünnen supraleitenden Schichten sollen das überhitzte kritische Magnetfeld eines massiven Supraleiters aus Vollmaterial erhöhen und damit zu höheren maximal erreichbaren Beschleunigungsfeldstärken führen. Mit der zweiten im Rahmen dieser Arbeit untersuchten Probe konnten die theoretischen Beschreibungen der magnetischen Eindringtiefe und des überhitzten kritischen Magnetfelds für mehrlagige Systeme bestätigt werden. Die Beobachtung von Oberflächenwiderstand mit nicht-monotonem Temperaturverhalten deutet auf weitere Widerstandsbeiträge außerhalb der bisherigen Theorie hin und eröffnet ein vielversprechendes Feld für weitere Untersuchungen.

Contents

List of Figures

List of Tables

List of Abbreviations

BCP Buffered Chemical Polishing

BCS Bardeen, Cooper and Schrieffer

CERN European Organization for Nuclear Research

CW Continuous Wave

DAC Digital-to-Analog Converter

DC Direct Current

DFE (Number of) Degrees of Freedom

EB Electron Beam

EDS Energy Dispersive X-ray Spectroscopy

EP Electro-polishing

ERL Energy Recovery Linear Accelerator

ESS European Spallation Source

FIB Focused Ion Beam

FM Frequency Modulation

FRIB Facility for Rare Isotope Beams

GL Ginzburg-Landau Theory

HZB Helmholtz-Zentrum Berlin

LCLS-II Linear Coherent Light Source II

LEP Large Electron-Positron Collider

LF Lorentz Force

LHC Large Hadron Collider

LHeC Large Hadron Electron Collider

PLL phase-locked loop

QPR Quadrupole Resonator

RF Radio Frequency

RMSE Root Mean Squared Error

RRR Residual Resistance Ratio

SEM Scanning Electron Microscopy

SRF Superconducting Radio Frequency

SSE Sum of Squared Errors

UHV Ultra-High Vacuum

VLN Vortex Line Nucleation

VNA Vector Network Analyzer

XFEL X-Ray Free-Electron Laser

1 Introduction and Motivation

Superconducting radio-frequency (SRF) cavities are crucial components that enable advanced particle accelerators: When combining long-pulse or continuous-wave (CW) operation with accelerating gradients above a few MV/m, RF losses in normal conducting structures become unmanageable [1]. The European X-Ray Free-Electron Laser (XFEL) [2] and the Linear Coherent Light Source II (LCLS-II) [3] are two examples of state-of-the-art electron accelerators that provide extraordinary beam parameters using SRF technology. In the field of hadron accelerators, SRF cavities are used for accelerating protons as well as ion beams, e.g. the European Spallation Source (ESS) [4] and the Facility for Rare Isotope Beams (FRIB) [5]. The combination of CW operation with high quality factors enables efficient Energy Recovery Linear Accelerators (ERLs): The accelerated beam is recirculated and passes the cavities a second time with 180° phase shift, now experiencing a deceleration. As a result of the high intrinsic quality factor of SRF cavities, the beam energy is stored in the electro-magnetic field and transferred to the next particle bunch for acceleration. Such configurations are, for example, very attractive for future electron-hadron colliders such as the Large Hadron Electron Collider (Large Hadron Electron Collider (LHeC)) [6] or the Electron-Ion Collider (e-RHIC) [7].

Currently, niobium is the material of choice for SRF cavity production. It has the highest critical temperature and the highest critical magnetic field of all elemental superconductors, providing best SRF performance. Thanks to its metallic nature, SRF cavities can be fabricated from sheet or bulk material. Given by the small penetration depth of magnetic fields into superconductors ($\approx 100\,\mathrm{nm}$), the preparation of the surface layer is critical. In the past decades, much effort has been invested in overcoming various limitations, e.g. impurities, defects, roughness or contaminants [8]. Today, R&D cavities perform close to the theoretical limit, both in terms of surface RF magnetic field, limiting the achievable accelerating gradient [9, 10], as well as surface resistance, defining the quality factor [11]. Much effort is therefore expended to explore new materials that can outperform niobium. Of interest are not only materials that can go to higher field but also those that have reduced losses and can be operated at higher temperature.

The QPR – enabling systematic R&D on SRF materials

Such exploration of different materials requires extensive measurement series. However, the production and operation of SRF cavities is complex as well as costly and eventually only a limited parameter space is accessible, especially regarding operating temperature and RF frequency. Hence, systematic studies of SRF properties require dedicated sample tests on comparatively small scale structures and simpler geometries. Worldwide, this research is based on only few sample test cavities [12]. The Helmholtz-Zentrum Berlin (HZB) built and operates a Quadrupole Resonator (QPR) [13, 14]. Based on the initial development at CERN [15], it allows high resolution measurements of a flat circular surface at three RF frequencies in a wide parameter space spanned by temperature and RF field strength. Thereby, the instrument covers typical real-life accelerator operating parameters without being limited to them.

Within the scope of this thesis, the QPR measurement capabilities were continuously expanded and improved. The outcome of the process will be presented in Chapter 3, where the QPR at HZB and its measurement techniques are discussed in detail. An RF upgrade enabling measurements at two higher harmonic frequencies is presented. Furthermore, major effort was spent evaluating measurement uncertainties and identifying systematic limitations. Today, besides calorimetric measurements of the RF surface resistance with high-precision, further quantities such as magnetic penetration depth, critical temperature (T_c) and the RF critical field can be studied. From those directly measured values, superconducting and normal conducting quantities such as DC critical fields, Ginzburg-Landau parameter, mean free path and normal state resistivity can be derived, yielding a multi-parameter characterization of the investigated sample.

Thin film coatings for next generation SRF cavities

The penetration depth in superconductors is only in the range of 40 to 300 nm [16], confining any electromagnetic activity to a thin surface layer. Hence, superconducting coatings are one attractive alternative to bulk niobium. This concept was already successfully applied in the form of µm-thick niobium coatings on copper substrates. Niobium on copper cavities are routinely operated, e.g. in the Large Electron-Positron Collider (LEP) [17] and the Large Hadron Collider (LHC) [18] at CERN. An additional advantage of coating technologies is that they increase the number of material candidates, for instance those ones not suited for mechanical processing can be deposited on a substrate that already provides the final shape. The applications for new material SRF cavities are versatile. Higher critical temperatures could decrease RF losses, allowing for increased operating temperature. The cryogenic cooling required for today's SRF accelerators is a major contribution to both, capital and operating costs. Increasing

the operating temperature from 1.8 to 4.2 K holds the potential to save millions of Euros. At the same time, simplified cryo plants would open new fields of application such as small-scale SRF accelerators for industry or medicine.

Besides high T_c, which is necessary for higher operating temperature at low cryogenic load, such materials may provide a higher critical magnetic field H_c. Thanks to that, a higher superheating critical field H_{sh} is predicted which is expected to be the fundamental limit for a flux-free Meissner state – a prerequisite for cavity operation. H_{sh} thus determines the maximum achievable accelerating gradient, hence also the fundamental limit on accelerator length and eventually the facility size. However, coated samples and cavities are currently limited at RF quench fields that are significantly below H_{sh}. Besides the use of bulk-like coatings where all RF fields are screened in one layer, multi-layered systems of thin films provide an additional route to push the limits of bulk niobium [19]. Such structures gain only little in surface resistance, but might be less susceptible to early flux penetration due to coating flaws [20, 21]. This is especially relevant given the comparatively low values of H_{c1} for extreme type-II superconductors [16].

In this work, two superconducting coatings were characterized: One single thick layer of Nb_3Sn on Nb (Chapter 4) and a multilayer structure consisting of a thin NbTiN film on an AlN insulating layer on bulk Nb (Chapter 5). For both samples, RF measurement data on surface resistance, penetration depth and critical field is available which is discussed in detail.

Nb_3Sn is one of the most promising alternative materials to niobium and already showed high quality factors in coated research cavities. Theoretically, it should outperform niobium in terms of both achievable accelerating gradient as well as operating temperature. The sample investigated here underscores the potential of this high-T_c material for low surface resistance. Ultimately, this could enable low-loss CW particle accelerators. However the SRF performance failed to reach theoretical values, presumably due to off-stoichiometric areas that were subsequently identified using surface analysis. Furthermore, the RF quench field measurement indicated practical difficulties in reaching the superheating critical field of Nb_3Sn with the current coating process.

With the second sample characterized in this work, recent theoretical models of magnetic penetration depth and superheating field for multilayer structures can be confirmed. For the first time, such a thin-film system was investigated using the wide parameter space of a quadrupole resonator. The observation of non-monotonic surface resistance as a function of temperature reveals additional mechanisms that are not included in current theories and opens a promising field for future studies.

In Chapter 6 a summary of the main outcomes of this thesis is given. The outlook focuses on the lessons learned specifically with the HZB-QPR design and provides the groundwork for future quadrupole resonator developments.

Note that the structure of this thesis separates instrumentation and methods from experimental results of specific samples and it does not represent a chronology. Some techniques or setups were not yet available for the Nb_3Sn sample. That includes measurements of surface resistance at the second harmonic frequency (near 1.3 GHz) and measurements of the penetration depth with high precision. Given the promising results obtained so far, this is one possible activity for further continuation of the QPR research program at HZB.

2 Theory

The development of theoretical models explaining the experimental discovery of superconductivity took several tens of years. Intermediate results describing certain limiting cases or phenomenological approaches turned out to have a variety of applications, often with the advantage of providing analytical formulas. In the following, the historical development is sketched very briefly, focusing on those formulas that are used later on to interpret measurement data. Details are provided by numerous text books such as [22].

In 1911, H. Kamerlingh Onnes observed vanishing resistivity of mercury while trying to liquefy helium [23]. About 20 years later, Meissner and Ochsenfeld discovered the effect of perfect diamagnetism on cylindrical samples of lead and tin, thereby underscoring the fact, that superconductivity represents a new electronic phase, rather than merely perfect conductivity [24]. The phenomenological model by F. and H. London in 1935 [25] extends Maxwell's electrodynamics by two assumptions: The first London equation

$$\frac{\partial}{\partial t}\boldsymbol{J}_\mathrm{s} = \frac{n_\mathrm{s}e^2}{m}\boldsymbol{E} \tag{2.1}$$

describes infinite conductivity of the superconducting current density $\boldsymbol{J}_\mathrm{s} = -n_\mathrm{s}e\boldsymbol{v}$ with charge carrier density n_s, positron charge e, mass m and velocity $\boldsymbol{v}$. Charge carriers are accelerated freely and respond immediately to the electric field $\boldsymbol{E}$. The Meissner effect is included with the second London equation, requiring

$$\nabla \times \boldsymbol{J}_\mathrm{s} + \frac{n_\mathrm{s}e^2}{m}\frac{\partial}{\partial t}\boldsymbol{B} = 0 \tag{2.2}$$

with an external magnetic field $\boldsymbol{B}$. Within Maxwell's electrodynamics, only the time derivative of Eq. 2.2 is equal to zero. The important difference becomes visible when a superconductor is cooled through the transition temperature T_c in an external magnetic field: The perfect conductor "traps" all field inside and acts as permanent dipole magnet once the external field is switched off. A London superconductor expels the internal magnetic field during transition as observed by Meissner and Ochsenfeld. Furthermore, the characteristic length scale λ_L is obtained, describing the exponential decay of magnetic fields penetrating a semi-infinite superconductor. The very successful two-fluid model by Gorter and Casimir [26, 27], explains vanishing DC resistance by two parallel currents – or fluids – one lossless supercurrent and one normal lossy current. The inertia of the supercurrent causes an AC surface resistance that is rising quadratically with frequency.

The temperature dependent superconducting fluid density yields for the London penetration depth

$$\lambda_{\mathrm{L}}(T) = \frac{\lambda_{\mathrm{L}}}{\sqrt{1 - \left(\frac{T}{T_{\mathrm{c}}}\right)^4}}. \tag{2.3}$$

The London equations require a "local" response of the superconductor to an external field. Pippard introduced the coherence length ξ, a second characteristic length scale, enabling non-local electrodynamics and taking into account a finite mean free path ℓ via [28]

$$\frac{1}{\xi} = \frac{1}{\xi_0} + \frac{1}{\ell} \tag{2.4}$$

with the material-specific value ξ_0 in the clean limit of $\ell \to \infty$. Furthermore, this increases the observed penetration depth to be [29]

$$\lambda(T, \ell) = \lambda_{\mathrm{L}}(T)\sqrt{1 + \frac{\pi}{2}\frac{\xi_0}{\ell}}. \tag{2.5}$$

In 1950, Ginzburg and Landau developed a macroscopic theory of superconductivity by investigating the phase transition in terms of an order parameter at the critical temperature T_{c} [30]. Their coherence length ξ_{GL}, describing the spacial development of the superconducting state, was later found to be connected to ξ_0. At that time, only type-I superconductors were known, exhibiting a phase transition if the external magnetic field exceeds a value of

$$H_{\mathrm{c}}(T) = H_{\mathrm{c}}(0) \cdot \left(1 - \left(\frac{T}{T_{\mathrm{c}}}\right)^2\right). \tag{2.6}$$

Abrikosov showed, that the Ginzburg-Landau parameter $\kappa = \lambda/\xi_{\mathrm{GL}}$ distinguishes between superconductivity of type-I and II with the limiting value of $\kappa = 1/\sqrt{2}$ [31]. In case of $\xi_{\mathrm{GL}} < \sqrt{2}\lambda$ the surface energy at the boundary of normal and superconducting domains becomes negative. External magnetic fields larger than a lower critical field $H_{\mathrm{c1}} < H_{\mathrm{c}}$ may enter the superconductor forming a triangular lattice of quantized flux lines with diameter determined by ξ_{GL}. This mixed state extends up to the upper critical field $H_{\mathrm{c2}} > H_{\mathrm{c}}$ above which superconductivity breaks down. The Ginzburg-Landau theory has still wide validity since Gor'kov proved its connection to the microscopic quantum formalism of Bardeen, Cooper, and Schrieffer [32].

In this first microscopic theory – named BCS after its discoverers – an attractive force between electrons is mediated by the surrounding atomic lattice, leading to an energy gap and the formation of so-called Cooper pairs of electrons [33, 34]. The coherence length ξ_0 that was introduced by Pippard can now be interpreted as the size of a Cooper pair. In order to break such a pair, the external energy of 2Δ, corresponding to the superconducting gap of the electronic energy spectrum, has to be expended. The energy gap is closely related to the critical temperature T_c of the superconductor by [22]

$$\frac{\Delta}{k_\mathrm{B} T_\mathrm{c}} = 1.764. \tag{2.7}$$

with Boltzmann constant k_B.

An important experimental confirmation was the observation of decreasing T_c at higher isotope mass, and hence the contribution of the atomic lattice to superconducting parameters [35, 36]. Based on BCS, Mattis and Bardeen derived the microwave surface resistance that is then important for the application to SRF cavities [29, 37]. As a result of the technological progress of SRF cavities, especially when using niobium, the achievable RF magnetic field strength reached a level where its impact on the superconducting state itself may not longer be neglected. Advanced theoretical calculations are available considering e.g. effects such as a modified density of states or imperfect surfaces [38, 39].

2.1 SRF Loss Mechanisms and Surface Resistance

SRF cavities are primarily used for acceleration of charged particle beams. Hence, a beam axis is defined where strong longitudinal electric fields are requested. Given by geometry of the cavity, an infinite set of resonant modes can be excited. Usually, only the mode with lowest frequency is used for acceleration and excited intentionally. Even though having no electrical resistivity for direct currents, superconductors experience dissipative heating due to the oscillating magnetic field according to

$$P_{\mathrm{diss,RF}} = \frac{1}{2} \iint R_{\mathrm{S}} \left|\boldsymbol{H}\right|^2 \mathrm{d}S \tag{2.8}$$

with surface resistance R_{S}. Regarding cavities as resonant circuits leads to the corresponding quality factor

$$Q_0 = \frac{f}{\Delta f} = \frac{\omega U}{P_{\mathrm{diss}}} \tag{2.9}$$

with bandwidth Δf and stored energy U. In order to separate RF field distribution and material specific surface resistance, the geometry factor G is introduced. G is determined only by the field distribution inside the cavity and, for a given resonant mode, depends only on the cavity shape but not on its size or mode frequency:

$$G = \frac{\omega \mu_0 \iiint \left|\boldsymbol{H}\right|^2 \mathrm{d}V}{\iint \left|\boldsymbol{H}\right|^2 \mathrm{d}S} \approx \frac{\omega U R_{\mathrm{S}}}{P_{\mathrm{diss}}} = Q_0 R_{\mathrm{S}} \tag{2.10}$$

The latter terms are valid only approximately since in practice R_{S} depends on RF field and may not be pulled out of the surface integral in Eq. 2.8. Minimizing dynamic losses in SRF cavities is directly addressed by minimizing the surface resistance e.g. by the choice of material, surface treatments or the operating temperature.

Throughout this thesis, RF field strength is typically given in units of mT since it can be directly compared to the intrinsic critical fields of a superconductor. However, for accelerating cavities most commonly the accelerating electric gradient is used in MV/m. To compare those different quantities, the ratio $B_{\mathrm{pk}}/E_{\mathrm{acc}}$ of peak magnetic field occurring somewhere on the cavity wall to the accelerating electric gradient is needed which depends on the specific cavity geometry. For elliptical shapes such as TESLA [40] typical values are about $4\,\mathrm{mT/(MV/m)}$ ranging up to $10\,\mathrm{mT/(MV/m)}$ in quarterwave structures [41].

2.1.1 BCS Surface Resistance

Within the BCS theory, analytical expressions for the surface resistance are available only under certain assumptions. If the mean free path of unpaired electrons ℓ is short, impurity scattering is a significant contribution to the surface resistance. For the dirty limit $\ell \ll \lambda$ the expression

$$R_{\mathrm{BCS,dirty}} = \mu_0^2 \omega^2 \lambda^3 \sigma \ln\left(\frac{2.25 k_\mathrm{B} T}{\hbar\omega}\right) \frac{\Delta}{k_\mathrm{B} T} \exp\left(-\frac{\Delta}{k_\mathrm{B} T}\right) \tag{2.11}$$

is obtained [38]. Increasing ℓ, i.e. the normal state conductivity σ, leads to smaller R_S since $\lambda^3 \propto \ell^{-3/2}$ outweighs $\sigma \propto \ell$ [41]. For intermediate values with $\ell \approx \xi (\approx \lambda)$ a distinct minimum in surface resistance is observed. Further purifying the superconductor leads to increasing R_S since $\lambda \to \lambda_\mathrm{L}$ and $\sigma \propto \ell$ dominates. In the clean limit ($\ell \gg \lambda$) a behavior similar to the anomalous skin effect [42] is observed with saturating BCS resistance

$$R_{\mathrm{BCS,clean}} = \frac{3\mu_0^2 \omega^2 \lambda^4 \sigma}{2\ell} \ln\left(\frac{1.2 k_\mathrm{B} T \Delta \xi^2}{\hbar^2 \omega^2 \lambda^2}\right) \frac{\Delta}{k_\mathrm{B} T} \exp\left(-\frac{\Delta}{k_\mathrm{B} T}\right) \tag{2.12}$$

that is independent of ℓ, since $\lambda = \lambda_\mathrm{L}$ and $\sigma/\ell = \mathrm{const}$. Both formulas above are approximations for low temperatures $T \leq T_\mathrm{c}/2$ and small RF currents. For calculation of the BCS surface resistance at arbitrary temperature or mean free path, numerical tools like SRIMP [43] are available. This program is also used to visualize the BCS surface resistance as a function of mean free path in Fig. 2.1.

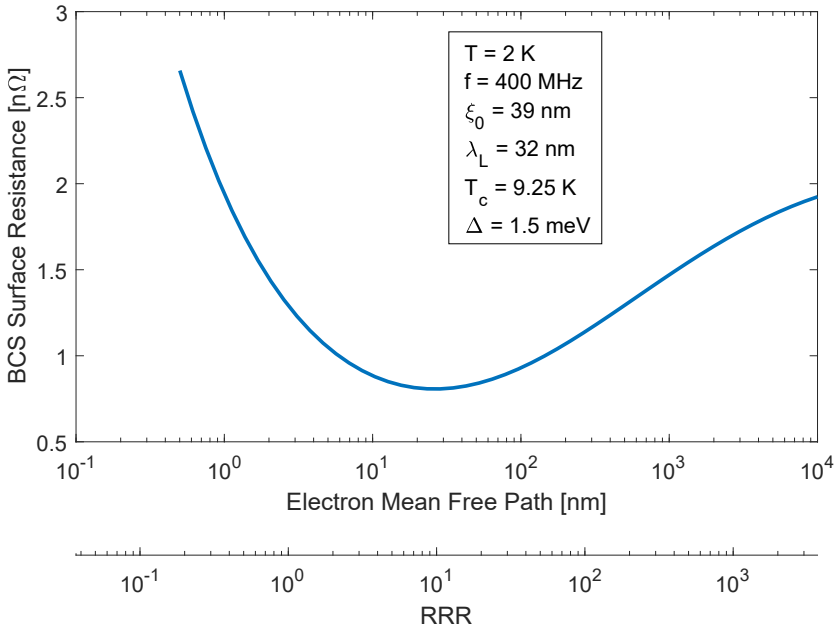

Figure 2.1: *Numerical calculation of the niobium BCS surface resistance vs. electron mean free path using SRIMP [43] at 2 K and 400 MHz.*

Independent of the assumed impurity limit and hence independent of ℓ the expression

$$R_{\mathrm{S}}(T) = \frac{af^2}{T} \exp\left(-\frac{\Delta}{k_{\mathrm{B}}T}\right) \tag{2.13}$$

can be used to fit surface resistance measurement data with the free parameter a for temperatures up to $T_{\mathrm{c}}/2$ [44].

Typically the normal state resistivity ρ is given at room temperature together with the residual resistivity ratio (RRR)

$$\mathrm{RRR} = \frac{\rho(300\,\mathrm{K})}{\rho_{\mathrm{NC}}(4.2\,\mathrm{K})} = \frac{\sigma_{\mathrm{NC}}(4.2\,\mathrm{K})}{\sigma(300\,\mathrm{K})} \tag{2.14}$$

taking into account the increasing normal state conductivity at low temperature. Since the conductivity is directly related to the electron mean free path, one finds for niobium at low temperature [45]

$$\ell\,[\mathrm{nm}] = 2.7 \cdot \mathrm{RRR}. \tag{2.15}$$

2.1.2 Residual Resistance

From the BCS treatment of surface resistance as introduced above, vanishing R_{S} for $T \to 0\,\mathrm{K}$ would be expected. This contradicts measurements on various samples and cavities showing an additional, temperature independent surface resistance, called residual resistance R_{res}. Possible sources of residual resistance such as surface oxides, hydride formation or weakly coupled grain boundaries are material-related and have been studied intensively for bulk niobium [8]. For alternative materials and thin film coatings the distinction between intrinsic losses and technology-related issues will be crucial to judge their potential use in SRF applications.

In general, one dominant contribution to R_{res} is given by trapped, or frozen, DC magnetic flux by pinning centers such as material defects or impurities [8]. If ambient magnetic fields are present while cooling down through the superconducting transition, up to 100 % can be trapped leading to an incomplete Meissner state. Moving flux lines and their normal conducting cores lead to considerable residual resistance that furthermore depends on impurities, pinning behavior and RF frequency. Magnetic shielding, reduction of pinning centers by high-temperature annealing as well as fast cooling with spacial temperature gradients reduces the amount of trapped flux. However, in the latter case bimetallic joints can generate thermocurrents causing a significant amount of trapped flux and foiling the efforts of magnetic shielding [46]. While dedicated cooling schemes avoid harmful spacial asymmetries and mitigate thermocurrents in niobium cavities, this mechanism seems to be an intrinsic issue for multilayer coatings, e.g. when using Nb_3Sn. In this case cooling has to be very slow, reducing temperature gradients as much as possible [47].

2.1.3 Non-linear Surface Resistance

Besides non-vanishing (residual) surface resistance towards low temperatures, a dependence of the surface resistance on the RF field strength is observed. To some extend an increasing R_S of an accelerating cavity with field – often referred to as Q-slope – can be explained by a thermal feedback mechanism: Since all RF heating has to be transported through the cavity wall into the helium bath, the limited thermal conductivity and finite boundary resistance lead to an increased temperature at the RF surface. Given the strong dependence of the BCS surface resistance on temperature, this causes even higher losses and possibly a thermal runaway with breakdown of superconductivity in case of insufficient cooling [8]. Usually a quadratic dependence of $R_S(B)$ is observed [41].

A non-monotonic dependence of R_S on RF field, called anti Q-slope, was observed on niobium cavities where impurities were diffused into the RF-affected top layer ("doping") [48]. In this case, a different explanation is required since the BCS treatment of surface resistance as introduced above is strictly valid only at low RF fields. Taking into account a change of density of states due to the amplitude and frequency of RF currents yields a decrease in surface resistance that can extend up to medium RF fields of about 60 mT. This corresponds to 25 % of the superheating limit of niobium (see Section 2.2.3) or $E_{acc} = 15\,\mathrm{MV/m}$ as observed in doped cavities [11, 49]. Further increasing the RF field will eventually lead again to Q-slope behavior of increasing resistance [50]. A different formalism of modified density of states including states inside the superconducting energy gap is furthermore able to incorporate both residual and temperature dependent surface resistance into one theoretical model [38].

2.1.4 Additional Resistance in Type-II Thin Film Structures

Type-II superconductors with typical Ginzburg-Landau parameters higher than that of niobium ($\kappa \gg \kappa_{Nb} \approx 1$) exhibit coherence lengths of only few nm. On that length scale, the risk of pair-breaking effects and vortex penetration at defects and grain boundaries is naturally increased. In simple words, Cooper pairs of small spacial extent, given by a short coherence length, are more sensitive to defects that are also on that length scale. For example in case of Nb_3Sn deposited via vapor diffusion as used for preparation of the sample characterized in Chapter 4, tin diffuses preferentially along grain boundaries which tends to yield non-stoichiometric composition at these locations. Modeling grain boundaries as weakly coupled Josephson junctions leads to field and frequency dependent residual resistance contributions that may both range from linear to quadratic [51–53]. Early experiments on Nb_3Sn coated cavities showed quadratic scaling of residual resistance with frequency according to [54]

$$R_{res}\,[\mathrm{n\Omega}] = 16 \cdot (f\,[\mathrm{GHz}])^2\,. \tag{2.16}$$

Recent results on 1.3 GHz cavities demonstrated $R_{\mathrm{res}} < 10\,\mathrm{n}\Omega$ [55], however most tests are done at this particular frequency and the scaling law with frequency might still be valid.

A second field dependent surface resistance contribution arises from thermal boundary resistance at interfaces between coated layers or at the substrate. A numerical method presented in [56] was able to model the strong Q-slope observed in niobium coated copper cavities. The equally striking and alarming result of this explanation is the fact, that thermal "voids" covering less than 0.1 % of the interface area cause $Q_0 < 10^{10}$ at medium accelerating gradients in 1.5 GHz elliptical cavities, corresponding to an average surface resistance greater than $25\,\mathrm{n}\Omega$ [40].

2.2 Critical Fields and Field Limitations

In this section the intrinsic limit for achievable accelerating gradients in superconducting cavities is addressed. It is defined by the maximum (RF) magnetic field a superconductor can withstand before superconductivity breaks down. Since nearly all materials that are relevant for SRF applications are superconductors of type II, the Ginzburg-Landau theory provides a convenient description and is introduced first. For practical, non-fundamental limitations of accelerating cavities such as field emission or thermal breakdown, the reader is referred to [8] and [41].

2.2.1 Ginzburg-Landau Theory

The macroscopic theory of superconductivity by Ginzburg and Landau is based on an order parameter ψ, describing a second order phase transition at the critical temperature T_c [30]. Compared to BCS, ψ can be seen as wave function describing the center of mass motion of Cooper pairs with density $|\psi|^2$ [22]. Strictly valid only for temperatures close to T_c, a series expansion of the free energy with two initially unknown coefficients is considered. The first expansion coefficient determines a coherence length ξ that, in contrast to the BCS coherence length ξ_0, depends on temperature as $\xi \propto (1-T/T_\mathrm{c})^{-1}$ and diverges at T_c. The second expansion coefficient is directly connected to the Ginzburg-Landau parameter

$$\kappa = \frac{\lambda(T,\ell)}{\xi(T)}. \tag{2.17}$$

Seven years after the publication of Ginzburg and Landau, Abrikosov showed that the value of κ distinguishes between superconductors of type I ($\kappa < 1/\sqrt{2}$) and type II ($\kappa > 1/\sqrt{2}$) [31].

A relation between the two different coherence lengths becomes visible via their connection to the thermodynamic critical field H_c that exists within Ginzburg-Landau (GL) as well as in the BCS theory [22]. The GL H_c is given by

$$\mu_0 H_\mathrm{c}(T) = \frac{\Phi_0}{2\sqrt{2}\pi\xi(T)\lambda(T,\ell)} \tag{2.18}$$

while for BCS and $T = 0\,\mathrm{K}$

$$\mu_0 H_\mathrm{c}(0\,\mathrm{K}) = \frac{\sqrt{3}}{\pi^2\sqrt{2}}\frac{\Phi_0}{\xi_0\lambda_\mathrm{L}} \tag{2.19}$$

is obtained. $\Phi_0 = h/2e = 2.068\cdot10^{-15}\,\mathrm{Wb}$ denotes the magnetic flux quantum. The dependence of H_c on temperature is approximately given by Eq. 2.6. Deviations from the quadratic behavior are predicted by the BCS theory and have been confirmed experimentally [57].

Extrapolating the Ginzburg-Landau case to 0 K and combining both formulas yields the following relation between ξ_0 and ξ:

$$\xi(0\,\mathrm{K}) = \frac{\pi}{2\sqrt{3}} \frac{\lambda_\mathrm{L}}{\lambda_0} \xi_0 \tag{2.20}$$

λ_0 denotes the effective penetration depth at 0 K including the electron mean free path according to Eq. 2.5. In case of $\ell \ll \xi_0$ this can be further reduced to

$$\xi \approx \sqrt{\frac{\pi}{6} \ell \xi_0} = 0.72 \sqrt{\ell \xi_0}. \tag{2.21}$$

Inserting Eq. 2.20 into the definition of κ in Eq. 2.17 yields the temperature dependence

$$\kappa(T) = \frac{2\sqrt{3}}{\pi} \frac{\lambda^2(T)}{\xi_0 \lambda_\mathrm{L}} \left(1 - \left(\frac{T}{T_\mathrm{c}}\right)^2\right) = \frac{2\sqrt{3}}{\pi} \frac{\lambda_0^2}{\xi_0 \lambda_\mathrm{L}} \frac{1}{1 + \left(\frac{T}{T_\mathrm{c}}\right)^2} \tag{2.22}$$

as well as the connection to BCS parameters. In the following, the dependencies on temperature and mean free path of values such as κ, λ and ξ are usually abbreviated. However, ξ_0 and λ_L are always intrinsic material parameters for the clean, stoichiometric superconductor at $T = 0\,\mathrm{K}$.

2.2.2 Lower Critical Field

For type-II superconductors ($\kappa > 1/\sqrt{2}$) the Meissner state is no longer energetically favorable in case of ambient magnetic fields larger than the lower critical field H_{c1}. Quantized flux lines, or vortices, characterized by Φ_0 penetrate the superconductor in a triangular lattice. If not pinned by local inhomogeneities, e.g. at impurities or grain boundaries, vortices can move under external forces from electromagnetic fields or currents and will cause dissipation. For superconducting magnets and current transport applications this is solved by introducing a sufficient amount of pinning centers. However in case of SRF cavities where vortex oscillations, depinning and losses inside the normal conducting vortex cores are also relevant, a vortex-free Meissner state is required.

In the high-κ limit, H_{c1} is given by [58]

$$\mu_0 H_{c1} = \frac{\Phi_0}{4\pi\lambda^2} \left(\ln \kappa + 0.497\right). \tag{2.23}$$

For arbitrary values of κ, numerical calculations are required. Fig. 2.2 shows data from [59] and the high-κ approximation according to Eq. 2.23. For intermediate values of κ the power fit

$$H_{c1} = \frac{0.83}{\kappa^{0.63}} H_c \tag{2.24}$$

can be used. This fit does not converge to Eq. 2.23 for $\kappa \to \infty$, limiting its validity to $\kappa \lesssim 50$.

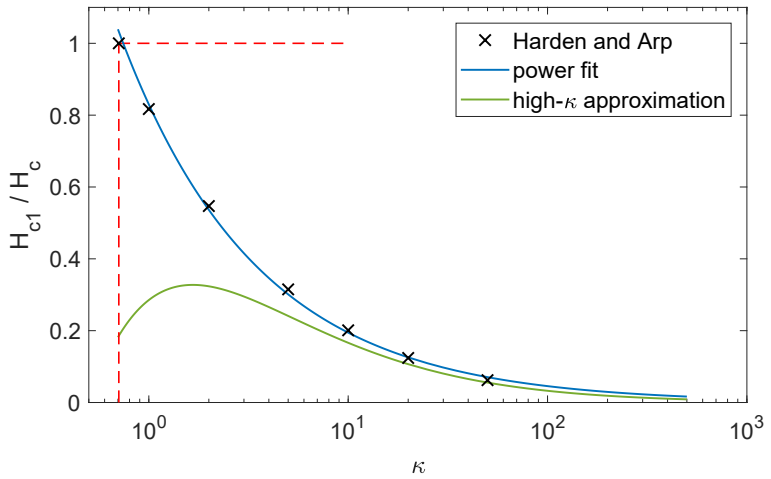

Figure 2.2: *Lower critical field normalized to H_c vs. κ. Numerical values from [59] are interpolated by a power fit, the high-κ approximation is calculated according to Eq. 2.23. Red dashed lines indicate the limiting case of $\kappa = 1/\sqrt{2}$ with $H_{c1} = H_c$.*

In case of superconducting thin films with thickness $d \ll \lambda$, the vortex penetration behavior due to static parallel magnetic fields changes. Evaluating the surface energy barrier yields an increased lower critical field

$$\mu_0 H_{c1} = \frac{2\Phi_0}{\pi d^2}\left(\ln\frac{d}{\xi} + \gamma\right) = \frac{2\Phi_0}{\pi d^2}\ln\left(\frac{d}{1.074\xi}\right) \tag{2.25}$$

with $\gamma = \ln(2/\pi)+0.38 = -0.07$ [60]. Compared to the high-κ limit (see Eq. 2.23) and neglecting numerical factors, the penetration depth λ is replaced by the film thickness d. Qualitatively, this is due to the fact that the surface energy barriers on both sides of the film are at such short distance that d rather than λ determines the longitudinal magnetic field profile.

2.2.3 Superheating Critical Field

The superheating critical field H_{sh} denotes the upper limit of a metastable Meissner phase. Even though being larger than H_{c1}, the penetration of vortices due to an external RF magnetic field is prevented thanks to an energy barrier at the surface of the superconductor. For SRF applications, H_{sh} is considered to put the fundamental limit on RF magnetic field in terms of vortex penetration and hence the achievable accelerating gradient of a given cavity geometry. The superheating field is of special interest in case of extreme type-II superconductors where H_{c1} is limited by κ to uselessly low values. The upper critical field [22]

$$H_{c2} = \sqrt{2}\kappa H_c \tag{2.26}$$

corresponds to the ultimate breakdown of superconductivity for type-II superconductors and is important for DC magnets and current transport properties only. For RF fields in the mixed state with $H_{sh} < H_{RF} < H_{c2}$ dynamic losses are unmanageable and lead to thermal instability of SRF cavities.

As for H_{c1}, the full dependence of H_{sh} on κ can not be expressed with an analytical expression. Depending on the value of κ, analytical expressions are available as results of numerical calculations investigating the stability of the Meissner state against perturbations. Below a critical value $\kappa_c \approx 1.1495$ [61], one-dimensional Ginzburg-Landau theory can be used, yielding [62, 63]

$$H_{sh} \approx H_c\, 2^{-1/4}\kappa^{-1/2}\frac{1 + 4.682\,512\,0\kappa + 3.347\,831\,5\kappa^2}{1 + 4.019\,599\,4\kappa + 1.000\,571\,2\kappa^2}. \tag{2.27}$$

In the narrow range $0.707 < \kappa < 0.92$ the superheating field even exceeds H_{c2}, hence fields larger than H_{sh} will cause a direct transition into the normal conducting state. For $\kappa > \kappa_c$ two-dimensional perturbations have to be taken into account, leading to [61]

$$H_{sh} \approx H_c \left(\frac{\sqrt{20}}{6} + \frac{0.5448}{\sqrt{\kappa}} \right) \tag{2.28}$$

with asymptotic value

$$H_{sh,\infty} = 0.745\, H_c \tag{2.29}$$

for $\kappa \to \infty$. Since the formulas above were developed using Ginzburg-Landau theory, they are strictly valid only in close vicinity to T_c. For the asymptotic high-κ limit (Eq. 2.29), the temperature dependence of H_{sh} was derived in [64], predicting an increased value of

$$H_{sh,\infty}(0\,\mathrm{K}) = 0.84\, H_c \tag{2.30}$$

at $T = 0\,\mathrm{K}$. Furthermore, slightly non-monotonic behavior is observed at low temperature with a global maximum of H_{sh} at $T \approx 0.04 T_c$. Neglecting this effect, the quadratic temperature dependence of the thermodynamic critical field (see Eq. 2.6) provides a good approximation for the superheating critical field.

2.2.4 Vortex Line Nucleation

Measurement data on the RF quench field of superconducting cavities and samples showed deviations from a quadratic temperature dependence and lower values as expected for the superheating critical field [65, 66]. One possible explanation for this behavior is given by vortex penetration at defects with a size on the order of the coherence length. The vortex line nucleation model (VLN) gives an heuristic formula for this limitation [67]:

$$H_{VLN} = \frac{1}{\kappa} H_c \tag{2.31}$$

As κ depends on temperature as (see Eq. 2.22)

$$\kappa(T) = \frac{\kappa(0\,\mathrm{K})}{1 + \left(\frac{T}{T_c}\right)^2} \tag{2.32}$$

the final temperature dependence of H_{VLN} is given by

$$H_{VLN}(T) = H_{VLN}(0) \left(1 - \left(\frac{T}{T_c} \right)^4 \right). \tag{2.33}$$

The derivation of the vortex line nucleation model uses a thermodynamic energy balance approach. This does not contain any superheating effects and makes H_{VLN} similar to H_{c1}. For this reason, the model is criticized being a non-fundamental experimental extrapolation of measurement data due to non-ideal surface characteristics [64]. For large values of κ the unphysical condition of $H_{\mathrm{VLN}} < H_{\mathrm{c1}}$ is obtained. However, VLN has been successfully applied to earlier measurements on the RF critical field of Nb_3Sn and showed better agreement than a quadratic fit [65, 66]. Also, in case of niobium, it yielded values of κ that were in agreement with low field surface impedance measurements [68].

2.2.5 Field Enhancement

Looking at real surfaces of superconducting cavities or samples, performance limiting surface structures such as pits and bumps can occur. In the context of critical fields we will omit the aspect of field emission which is mostly relevant for regions of high electric field in accelerating cavities and focus on magnetic field enhancement. Those structures can originate from mechanical damages or chemical etching (BCP) and have sizes in the order of at least a few µm. This is large compared to the intrinsic length scales of the superconductor (λ, ξ) and we can assume the superconducting properties to be unaffected. Now, the magnetic field enhancement can be calculated using Maxwell's equations and [69, 70]. Depending on the actual surface geometry, a field enhancement factor $\beta \geq 1$ is defined leading to $H_{\mathrm{mfe}} = \beta H$. This factor is especially independent of the local magnetic field and temperature, leading to the locally decreased RF critical field

$$H_{\mathrm{crit.\ RF,\ mfe}}(T) = \frac{H_{\mathrm{sh}}(T)}{\beta}. \tag{2.34}$$

Field enhancement leading to local quenches and small normal conducting regions is one model for the observed high-field Q-slope in niobium cavities [71]. In case of Nb_3Sn thin films produced by tin diffusion coating on bulk niobium substrates, significant surface roughness is observed causing field enhancement all over the coated surfaces. This might partially explain the low quench limit of Nb_3Sn cavities compared to the superheating limit [72].

2.3 S-I-S′ Layered Structures

Based on the increase of H_{c1} for single superconducting thin films (see Eq. 2.25), Gurevich proposed multilayer coatings on bulk superconducting cavities to push the vortex penetration field beyond $B_{sh,bulk}$ [19]. The film thickness d has to be lower than the penetration depth λ of the film material, but still large compared to the coherence length ξ. Those conditions are intrinsically fulfilled by thin type-II superconductors. The practical challenge that type-II superconductors are typically not available as bulk materials, but have to be produced by techniques such as chemical or physical vapor deposition, perfectly fits this proposal.

In practice, vortices might penetrate a thin-film superconductor at lower fields than theoretically possible due to material or topographic defects. In order to prevent global instabilities by thermomagnetic avalanches that would limit the entire SRF structure, thin insulating layers can be put in between the superconductors [20]. In this case, penetrating vortex loops turn into vortex-antivortex pairs that are stopped in the insulator layer. However, the question whether RF dissipation due to vortex penetration into a thin superconducting layer is acceptable for SRF cavities or also leads to unmanageable high losses is answered differently [20, 73, 74].

The full theoretical description of multi-layered structures requires careful treatment of counter-flow currents induced due to the vicinity of several superconductors [21]. The following formulas are taken from [21], describing the general solution of a bulk superconducting substrate (S′) coated with one insulating layer (I) and one superconducting layer (S) on top. Required parameters are penetration depth and thickness of the S-layer (λ_1, d_S), thickness of the I-layer (d_I) and penetration depth of the substrate (λ_2). In this case, the depth profile of an externally applied magnetic field B_0 is given by

$$B(x) = \begin{cases} \gamma_2 B_0 \left(\cosh \frac{d_S - x}{\lambda_1} + \frac{\lambda_1 + d_I}{\lambda_1} \sinh \frac{d_S - x}{\lambda_1} \right) & 0 \leq x \leq d_S \\ \gamma_2 B_0 & d_S < x < d_S + d_I \\ \gamma_2 B_0 \exp\left(-\frac{x - d_S - d_I}{\lambda_2} \right) & x \geq d_S + d_I \end{cases} \tag{2.35}$$

with

$$\gamma_2 = \frac{1}{\cosh \frac{d_S}{\lambda_1} + \frac{\lambda_2 + d_I}{\lambda_1} \sinh \frac{d_S}{\lambda_1}}. \tag{2.36}$$

For the substrate an unperturbed exponential decay is obtained, starting from the reduced surface field $\gamma_2 B_0$ and described by λ_2. Inside the top layer, $B(x)$ deviates from this simple behavior due to the presence of a counterflow current. The current density

$$J(x) = -\frac{1}{\mu_0} \frac{\mathrm{d}B(x)}{\mathrm{d}x} \tag{2.37}$$

in the top layer now has a maximum value

$$J(0) = \gamma_2 \frac{B_0}{\mu_0 \lambda_1} \left(\sinh \frac{d_\mathrm{S}}{\lambda_1} + \frac{\lambda_2 + d_\mathrm{I}}{\lambda_1} \cosh \frac{d_\mathrm{S}}{\lambda_1} \right) = \gamma_1 \frac{B_0}{\mu_0 \lambda_1} \tag{2.38}$$

with

$$\gamma_1 = \frac{\sinh \frac{d_\mathrm{S}}{\lambda_1} + \frac{\lambda_2 + d_\mathrm{I}}{\lambda_1} \cosh \frac{d_\mathrm{S}}{\lambda_1}}{\cosh \frac{d_\mathrm{S}}{\lambda_1} + \frac{\lambda_2 + d_\mathrm{I}}{\lambda_1} \sinh \frac{d_\mathrm{S}}{\lambda_1}}. \tag{2.39}$$

This can be higher or lower compared to the "bulk"-value for a semi-infinitely thick superconductor

$$J_\mathrm{bulk}(x) = \frac{B(x)}{\mu_0 \lambda} \tag{2.40}$$

as applicable to the substrate layer. Hence, the entire S-I-S′ structure maintains a vortex-free (metastable) Meissner state until

- $J(0)$ exceeds the depairing limit of the top layer $\frac{B_\mathrm{sh}^{(\mathrm{S})}}{\mu_0 \lambda_1}$ and hence $\gamma_1 B(0) > B_\mathrm{sh}^{(\mathrm{S})}$, or
- the superheating limit of the bulk substrate is exceeded by $B(d_\mathrm{I} + d_\mathrm{S}) = \gamma_2 B_0 > B_\mathrm{sh}^{(\mathrm{sub})}$.

In other words:

$$B_\mathrm{vp,S\text{-}I\text{-}S'} = \min \left\{ \frac{B_\mathrm{sh}^{(\mathrm{S})}}{\gamma_1}, \frac{B_\mathrm{sh}^{(\mathrm{sub})}}{\gamma_2} \right\} \tag{2.41}$$

Obviously, values of γ_1 and γ_2 smaller than 1 are intended. For γ_2 this is always fulfilled, since any conducting top layer will reduce the magnetic field seen by the substrate. $\gamma_1 < 1$ is obtained if $\lambda_1 > \lambda_2 + d_\mathrm{I}$, which calls for type-II superconductors in the S-layer when using niobium as substrate material. A special and practically interesting case is achieved by a top layer of "dirty" niobium, which already enhances the bulk superheating field by about 20 % [20]. Note that from a theoretical point of view the insulating layer is not required and the formulas remain valid for $d_\mathrm{I} = 0$. Fig. 2.3 shows exemplary curves for $B(x)$ and $J(x)$ for a parameter set similar to the sample characterized in Chapter 5. For the calculation of the vortex penetration field $B_\mathrm{vp}(T)$ as given in Fig. 2.4, the temperature dependencies of λ_i and $B_{\mathrm{sh},i}$ have to be taken into account. For simplicity, the empirical expressions of Eqs. 2.3 and 2.6 are applied to λ_i and $B_{\mathrm{sh},i}$ respectively. The resulting B_vp exceeds $B_\mathrm{sh,Nb}$ for all temperatures, even though the superheating limit of the top S-layer is lower than that of niobium. For NbTiN only few data on H_c or H_sh is available, hence the estimate of $B_\mathrm{sh,NbTiN} = 200\,\mathrm{mT}$ is used. This corresponds to 50 % of the high-κ limit (see Eq. 2.30) with $\mu_0 H_\mathrm{c} = 500\,\mathrm{mT}$ as obtained from low-energy muon spin rotation measurements [75]. The reduction to 50 % is somewhat arbitrary but based on the experimental observation, that thin-film superconducting cavities and samples are currently limited by vortex penetration at fields levels that are both significantly higher than H_c1 but lower than H_sh [66, 76].

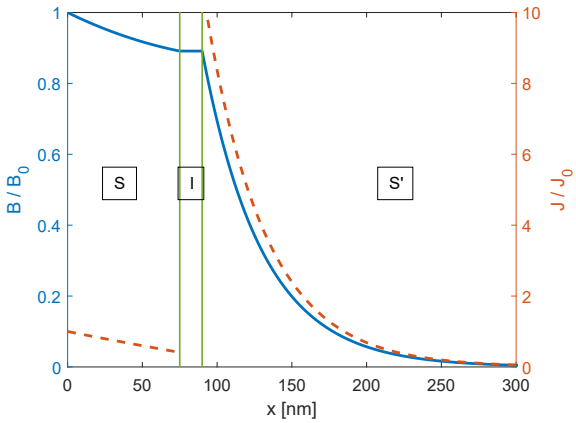

Figure 2.3: *Depth profiles of magnetic field (solid line) and current density (dashed line) in an S-I-S′ structure. Curves are calculated using Eqs. 2.35 and 2.37 with $d_S = 75\,nm$, $d_I = 15\,nm$, $\lambda_1 = 240\,nm$ and $\lambda_2 = 40\,nm$.*

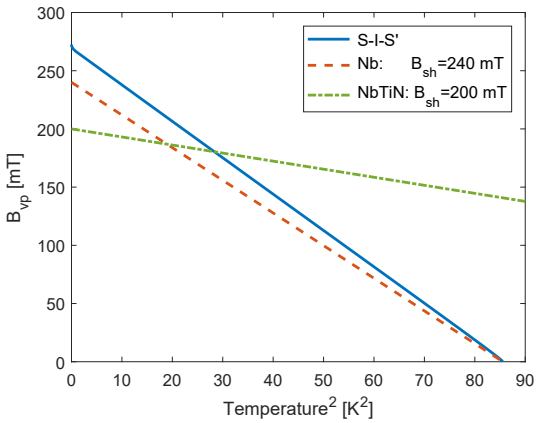

Figure 2.4: *Exemplary RF vortex penetration field. Curves are calculated using Eq. 2.41 and parameters as in Fig. 2.3 and $T_{c,NbTiN} = 17.3\,K$, $B_{sh,NbTiN} = 200\,mT$, $T_{c,Nb} = 9.25\,K$ and $B_{sh,Nb} = 240\,mT$.*

The total surface resistance of an S-I-S′ structure is given by adding up the RF dissipation of superconducting top layer and substrate that exhibit intrinsic surface resistances of $R_\mathrm{S}^{(\mathrm{S})}$ and $R_\mathrm{S}^{(\mathrm{sub})}$, respectively:

$$R_\mathrm{S} = 2\lambda_1 \frac{\mu_0^2}{B_0^2} R_\mathrm{S}^{(\mathrm{S})} \int_0^{d_\mathrm{S}} J^2(x)\,\mathrm{d}x + 2\lambda_2 \frac{\mu_0^2}{B_0^2} R_\mathrm{S}^{(\mathrm{sub})} \int_{d_\mathrm{S}+d_\mathrm{I}}^{\infty} J^2(x)\,\mathrm{d}x. \tag{2.42}$$

Dielectric losses in the I-layer are negligible, for GHz frequencies a surface resistance contribution of only $R_{\mathrm{S,I}} \approx d_\mathrm{I} \cdot 10^{-7}\,\frac{\mathrm{n\Omega}}{\mathrm{nm}}$ is expected [21]. Evaluation of the integrals yields

$$R_\mathrm{S} = \underbrace{\gamma_2^2 \left[\frac{1+r_\lambda^2}{2} \sinh\frac{2d_\mathrm{S}}{\lambda_1} + r_\lambda \left(\cosh\frac{2d_\mathrm{S}}{\lambda_1} - 1 \right) - \left(1 - r_\lambda^2\right) \frac{d_\mathrm{S}}{\lambda_1} \right]}_{r_1} R_\mathrm{S}^{(\mathrm{S})} + \underbrace{\gamma_2^2}_{r_2} R_\mathrm{S}^{(\mathrm{sub})} \tag{2.43}$$

with

$$r_\lambda = \frac{\lambda_2 + d_\mathrm{I}}{\lambda_1}. \tag{2.44}$$

r_1 and r_2 can be interpreted as weighting factors for the surface resistance contribution of each layer. Note that in general $r_1 + r_2 \neq 1$ and both values depend on temperature due to the temperature dependence of λ_i. Figs. 2.5 and 2.6 show an exemplary simulation for the S-I-S′ structure introduced before. The surface resistance of each layer is calculated using SRIMP [43] with $\frac{\Delta_i}{k_\mathrm{B} T_{\mathrm{c},i}} = 1.88$, $\xi_\mathrm{NbTiN} = 5\,\mathrm{nm}$, $\ell_\mathrm{NbTiN} = 3\,\mathrm{nm}$, $\xi_\mathrm{Nb} = 39\,\mathrm{nm}$, $RRR_\mathrm{Nb} = 300$ and $f = 1\,\mathrm{GHz}$. Additionally, all curves are limited at low temperature to $R_\mathrm{res} = 1\,\mathrm{n\Omega}$. The surface resistance of such an S-I-S′ structure is reduced by about 20 %, compared to uncoated niobium. In the case of

very low residual resistance as shown in Fig. 2.6, this reduction is achieved already at the typical operating temperature of 1.8 K. For higher R_{res}, this point is shifted towards higher temperature along with considerably higher total surface resistance. Hence, from the perspective of RF dissipation and required cryogenic infrastructure, thick film coatings that make maximum use of the low BCS resistance of high-T_{c} superconductors are preferred. However, given the quench limitation of current Nb_3Sn cavities [66], multi-layer coatings have the potential to boost vortex penetration and hence the achievable accelerating gradient of SRF cavities.

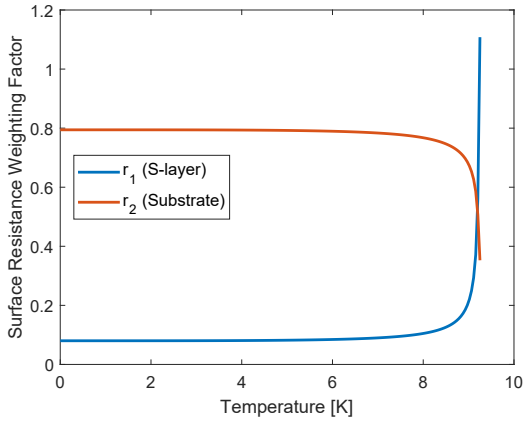

Figure 2.5: *Surface resistance weighting factors r_1 and r_2 vs. temperature. Curves are calculated using Eq. 2.43 and parameters as in Fig. 2.3.*

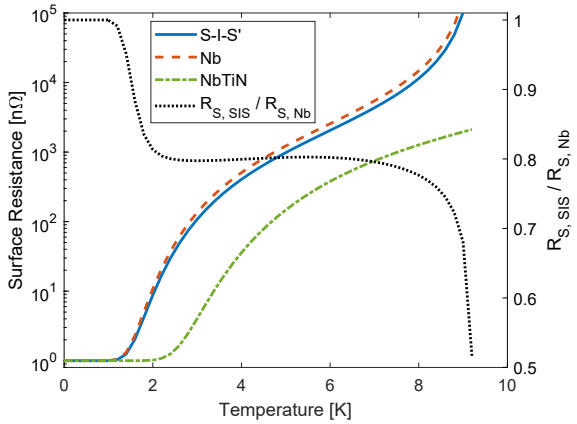

Figure 2.6: *Exemplary surface resistance of an S-I-S′ structure. Weighting factors are taken from Fig. 2.5 and $R_S(T)$ is calculated using SRIMP, plus 1 nΩ of residual resistance.*

3 Instrumentation: The Quadrupole Resonator

For R&D on SRF materials and for investigating fundamental questions such as SRF loss mechanisms or material limitations, sample test cavities are of high interest and of high value. Throughout the SRF community several systems exist, differing in operating frequency, sample size and shape as well in the accessible parameter space of frequency, temperature and RF field strength. For a review of other sample test cavities the reader is referred to [12]. At Helmholtz-Zentrum Berlin it was decided to build and operate a Quadrupole Resonator. The concept of this sample test cavity was developed at CERN where the first resonator was put into operation in 1997 [15, 77–79]. The QPR at HZB is based on that design with slightly shifted resonant frequencies and optimized measurement resolution and achievable field strength. Besides a short introduction given here the reader is referred to [13, 14, 80] for more information on the optimization process leading to the present design.

3.1 Overview and Mechanical Design

A sectional drawing of the QPR in given in Fig. 3.1. The three main parts of the QPR are the screening cavity (red), four quadrupole rods (green) and the sample chamber assembly (yellow). The entire system is immersed in liquid helium when sample tests are performed.

The nearly cylindrical screening cavity provides the RF volume and is made from high purity RRR 300 niobium. On top, four ports are available from which two are used for the installation of RF antennas and one for a vacuum pumping line. The most important parts for the generation of the RF field are four hollow Nb rods that serve as transmission lines. They are connected pairwise by crescent-shaped pole shoes at the bottom and shorted to the cavity at the top. The frequency of the quadrupole modes is determined by the length of the rods, for the first mode the length of one pair of rods corresponds to approximately one wavelength λ. The maximum RF magnetic field is located on the pole shoes and hence very close to the sample surface. Furthermore, the shape of these pole shoes define the high-field region on the sample surface. At higher harmonic frequencies this still holds while additional antinode(s) of RF magnetic field occur on the rods.

The sample chamber is a top hat like assembly which is inserted into the resonator from below. This chamber acts as inner conductor of a coaxial line with a cutoff frequency for quadrupole

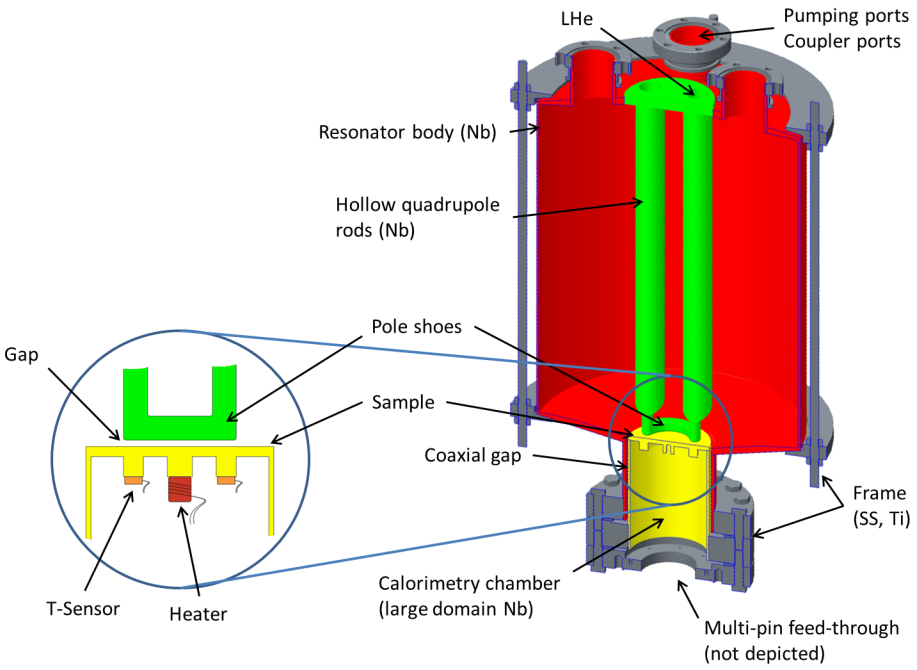

Figure 3.1: *Schematic view of the Quadrupole Resonator.*

modes of 2.5 GHz [81]. Hence, at frequencies below that value, RF waves propagating into the coaxial structure decay exponentially and RF losses on the side walls of the chamber are very small. Therefore, the actual RF sample surface is reduced to the planar surface on top of the chamber. Due to the small gap between sample surface and quadrupole pole shoes of 0.5 mm, the peak magnetic field on the sample is about 89 % of the maximum RF field occurring on the pole shoes [80]. The sample chamber is closed by a multi-pin feed-through and is evacuated separately. This ensures sufficiently good vacuum $\left(p < 5 \cdot 10^{-9}\,\text{mbar at } 1.8\,\text{K}\right)$ and clean conditions inside the resonator. The bottom surface of the sample is equipped with diagnostics, such as temperature sensors and up to two resistive heaters which is described later in more detail (see Sections 3.3.1 and 3.3.3. Inside the sample chamber, the requirements on vacuum pressure and cleanliness are relaxed, enabling also experimental diagnostics. Operational experience showed vacuum levels of about 10^{-7} mbar up to 10^{-4} mbar in the worst case.

The QPR is operated in a vertical helium bath cryostat ensuring the superconducting state of all niobium parts. The rods and pole shoes are made hollow to provide sufficient cooling of all high-field regions in the resonator. Due to the coaxial design at the bottom, the sample is thermally decoupled from the resonator, since direct thermal contact only exists at the mounting flange which is also in direct contact with the liquid helium bath. Furthermore, this setup offers the unique opportunity for measurements at different temperatures: By using a heater attached to the sample, its temperature can be adjusted freely above LHe temperature without influencing the resonator. Especially by using a pressure stabilized bath of superfluid helium, CW RF measurements at high fields are possible.

3.2 Upgrade I: Operation at Higher Harmonic Quadrupole Modes

Typical operating frequencies of SRF cavities range from about 100 MHz as used for quarterwave resonators in hadron accelerators up to few GHz for elliptical cavities in electron machines. The first three quadrupole modes of the QPR at frequencies of about 415 MHz, 850 MHz and 1285 MHz cover most of that relevant frequency space. Furthermore this allows to study both, the low-frequency regime of dominant residual resistance as well as BCS-dominated surface resistance and frequency dependencies. Given by the length l of one pair of quadrupole rods, harmonic frequencies with $f \approx n \cdot \frac{c}{l}$ can be excited. This relation is valid only approximately, since at higher frequency the ratio of electric to magnetic RF field on the sample surface increases, leading to a shift towards higher frequency.

Initially the QPR was commissioned at its first quadrupole mode. For measurements at higher quadrupole modes the pickup antenna and parts of the RF control system had to be changed, which is discussed in the following.

3.2.1 Multi-mode Pickup Antenna

The quadrupole resonator is equipped with four vacuum ports at its top. Given by the symmetry of the rods and the connecting pole shoes, each two ports being opposite are mirror symmetric to the RF (magnetic) field. Hence, two mounting locations for input and pickup antenna are defined (see labels "A" and "B" in Fig. 3.2a).

Initially, the QPR was equipped with two identical loop couplers for input and pickup coupling, both mounted on rotatable feedthroughs. Since the coupling is in first order the scalar product between RF magnetic field vector and enclosed loop surface, it can be varied by adjusting the orientation of the antenna. In order to cope with expected strong microphonics due to rod oscillations, the input coupler (external quality factor Q_{in}) was oriented for strong overcoupling providing a broadened resonance curve. The pickup coupler (external quality factor Q_{t}) was oriented close to minimum coupling satisfying the condition $Q_{\mathrm{in}} \approx Q_{\mathrm{L}} \ll Q_0 \ll Q_{\mathrm{t}}$. Fig. 3.3a shows the coupling of input and pickup antenna as a function of rotation, calculated with CST Microwave Studio® (MWS) [82]. For technical details on the simulation see Appendix Section A.8. Both couplers were mounted on opposite ports (type "B") on the QPR so the same curve(s) apply to both couplers. Since both couplers are approximately rotational symmetric, only rotational angles between 0 ° and 90 ° are shown. Analyzing the coupling to all modes as a function of rotational angle α and port position, yields four groups of modes with a) increasing or decreasing $Q_{\mathrm{ext}}(\alpha)$ and b) equal or opposite behavior at ports "A" and "B". At both port positions, $\alpha = 0\,^\circ$ denotes maximum coupling to the quadrupole modes, i.e. coupling

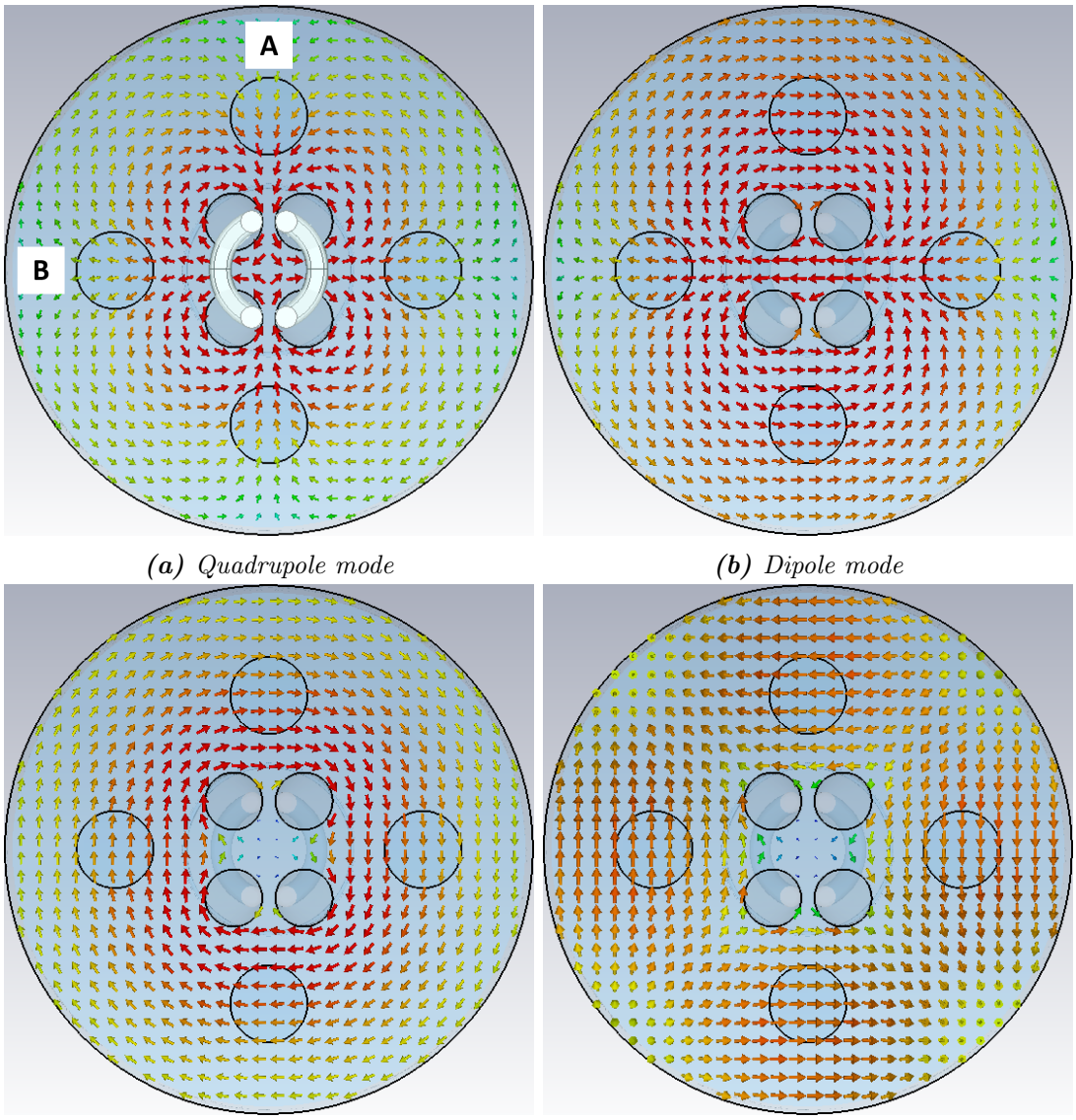

(a) *Quadrupole mode* **(b)** *Dipole mode*

(c) *Monopole mode* **(d)** *1287 MHz mode*

Figure 3.2: *RF magnetic field for different resonant mode types in a horizontal plane close to the location of vacuum ports at the top of the resonator.*

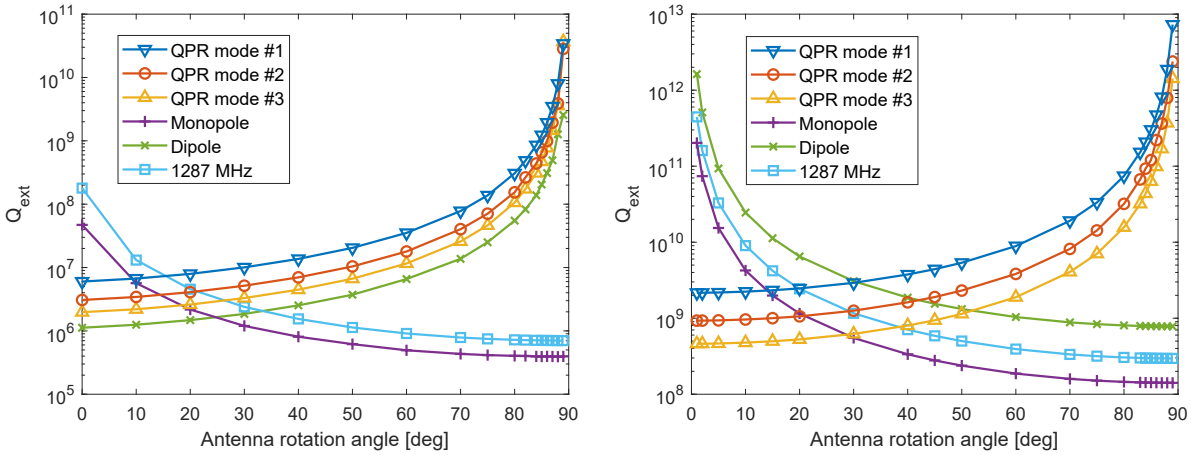

(a) *Initial loop coupler, mounted on port "B".*

(b) *New dedicated pickup coupler, port "A".*

Figure 3.3: *Q_{ext} of initial loop coupler (left) and new dedicated pickup coupler (right) as a function of rotational angle for all three quadrupole modes and the modes shown in Fig. 3.2. Only angles between 0 ° and 90 ° are plotted due to rotational symmetry. Both couplers show qualitatively comparable behavior if installed on the same port location. Note that the ordinates of plots (a) and (b) differ by several orders of magnitude.*

loop perpendicular to the RF magnetic field. Fig. 3.3 shows $Q_{\mathrm{ext}}(\alpha)$ for all mode types presented in Fig. 3.2. As discussed later, the cavity mode at 1287 MHz is the most critical non-quadrupole mode since it can be excited simultaneously with Q3 (see Section 3.2.3). By orienting the input coupler at $\alpha = 0\,^\circ$ (maximum Q_{ext}), the external excitation of that mode is suppressed strongly. However, this only helps for issues with the RF system, the problem of self-excitation due to microphonics remains (see Section 3.5.3).

The advantage of having a common design for both antennas comes with the drawback, that the pickup antenna has to be oriented close to 90 ° in order to achieve $Q_{\mathrm{ext}} > 10^9$. Since Q_{ext} is lower for higher harmonic frequencies, this becomes especially critical at the third quadrupole mode. At this orientation the coupling is highly sensitive to mechanical tolerances. Furthermore, handling during mounting is complicated. During first measurements the pickup coupling was changed two times, both without finding satisfying settings. Unstable pickup coupling was observed during operation, leading to systematic "jumps" in measured surface resistance [83]. In order to resolve these weak points, a dedicated pickup coupler for a target $Q_{\mathrm{ext}} = 10^9 \ldots 10^{10}$ at all three quadrupole modes was developed, that remains compatible to the existing rotatable feedthrough. Given by the field configuration in the upper region of the QPR and the positioning of available vacuum ports, a loop-type coupler is preferred. Besides omitting the protruding loop, the open diameter of the coaxial line had to be reduced in order to achieve high Q_{ext} at lower rotational angle. Sectional drawings of both couplers are given in Fig. 3.4, the corresponding coupling of the pickup antenna is shown in Fig. 3.3b.

In general, the coupling strength of a magnetic loop coupler is given by the size of the loop and its orientation relative to the magnetic field inside the cavity [84]. Assuming a thin and sufficiently small loop that allows for a perturbative approach yields

$$Q_{\mathrm{ext}}(\alpha) = \frac{Q_{\mathrm{e},0}}{\cos^2(\alpha)} \tag{3.1}$$

with rotational angle α and $Q_{\mathrm{e},0}$ denoting the case of strongest coupling when orienting the loop area perpendicular to the cavity's magnetic field. The quadratic dependence comes from the fact that the external quality factor is proportional to the emitted power and hence the RF field squared. Since Eq. 3.1 applies to the couplers discussed here, $Q_{\mathrm{e},0}$ is sufficient for quantitative comparison. The reduced distance between the quadrupole rods near port "A" causes a focusing effect and hence higher RF fields than at port "B". The resulting Q_{ext} at port "B" is higher by a factor 1.7 than at port "A" for all quadrupole modes and both loop couplers. The spread of Q_{ext} with frequency increases for the new coupler as visible in Fig. 3.3. While decreasing inversely proportional to frequency in case of the initial coupler, the new coupler without protruding loop section suppresses low frequencies by introducing an internal cutoff. Tab. 3.1 summarizes $Q_{\mathrm{e},0}$ for both couplers and both types of ports. A full set of plots showing Q_{ext} for both coupler types and both port locations can be found in Appendix Section A.2.

Table 3.1: *Minimum external quality factor $Q_{e,0}$ for QPR loop couplers.*

Type	Initial coupler		New coupler	
Port	"A"	"B"	"A"	"B"
Q1	$3.6 \cdot 10^6$	$6.0 \cdot 10^6$	$2.2 \cdot 10^9$	$3.6 \cdot 10^9$
Q2	$1.8 \cdot 10^6$	$3.1 \cdot 10^6$	$0.93 \cdot 10^9$	$1.6 \cdot 10^9$
Q3	$1.2 \cdot 10^6$	$2.0 \cdot 10^6$	$0.46 \cdot 10^9$	$0.78 \cdot 10^9$

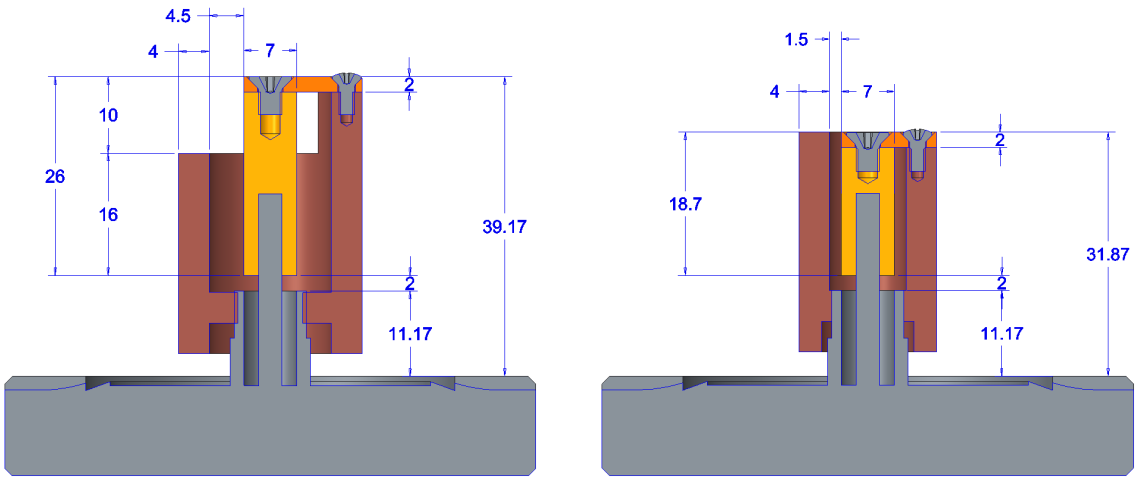

Figure 3.4: *Sectional drawings of initial loop coupler (left) and new dedicated pickup coupler (right). The initial design is still used as input antenna.*

3.2.2 Broad-band Phase-locked Loop RF Control System

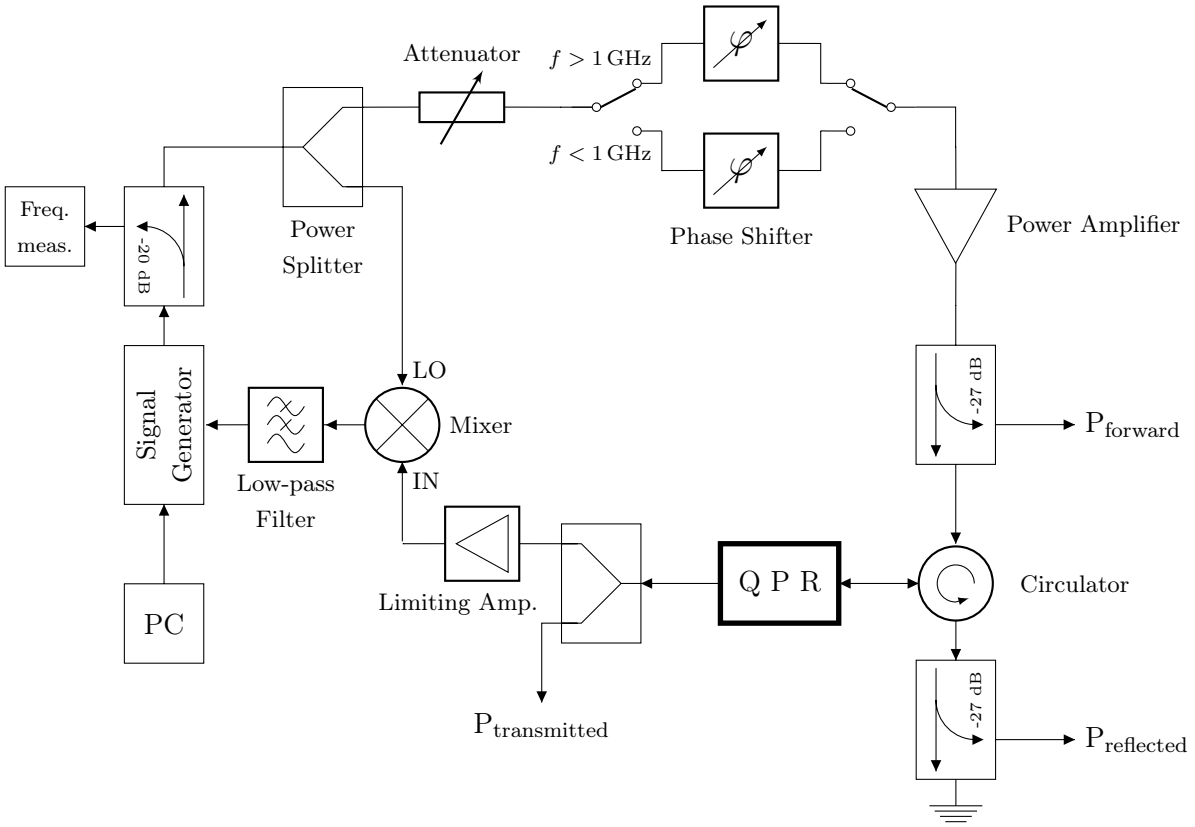

Figure 3.5: *Sketch of the RF control system.*

A phase-locked loop (PLL) is used to lock the signal generator (Rohde & Schwarz SMB100A) to the resonant frequency of the QPR: The pickup signal coming from the cavity is amplified to a constant power level by a phase constant limiting amplifier. This signal is multiplied with the generator output. The double-frequency component is rejected using a low-pass filter and the resulting signal is inversely proportional to the frequency deviation from the resonance center. After further filtering and level adjustment this signal is fed back to the Frequency Modulation (FM) input of the signal generator. To compensate for a constant phase offset between both signal branches (the transit time difference), the QPR input signal can be phase shifted by up to 360 °. A schematic drawing of the entire RF control system is given in Fig. 3.5.

In the forward power branch a variable attenuator is used to adjust the RF field level, since the power amplifier has fixed gain. Operating with strong overcoupling on the QPR input antenna leads to almost full reflection, hence a circulator protects the amplifier from back traveling power. Broad-band directional couplers enable measurements of forward and reflected power. The power transmitted to the pickup antenna is low enough that the power meter does not require a directional coupler for safe operation.

Since the used power amplifiers and circulators do not cover the full required bandwidth for all three quadrupole modes, specific devices for each mode are available. For low-power broad-band measurements, both amplifier and circulator can be bypassed. In the low power RF system all components provide enough bandwidth or could be sufficiently upgraded except for the variable phase shifter. In order to minimize the number of connections to be changed, two different phase shifters are selectable by a mechanical switch (threshold $\approx 1\,\mathrm{GHz}$).

A measurement PC is used for full configuration and control of the RF system running a custom LabVIEW™ program. Equipped with an internal Digital-to-Analog Converter (DAC) module, both phase shifters and the attenuator are voltage controlled. The frequency dependence of those components is recorded and compensated with calibration curves accordingly. The signal generator provides an internal pulse generator with RF pulse modulation. This is used for pulsed RF and also single, software-triggered pulses. The power meters for forward, reflected and transmitted power can measure average CW power level, as well as pulse traces with high time resolution down to 50 ns (see also Section 3.5). In case of pulsed RF the signal generator is also used to synchronize and trigger all connected measurement devices. For communication between computer and measurement devices interfaces for USB, Ethernet and GPIB (IEEE 488) are available.

3.2.3 Operational Experience I: Frequency Shift and Mode Order Swapping

The QPR is highly susceptible to mechanical perturbations due to its mechanical design featuring a cylindrical cavity and long rods which are fixed only on one side. Besides microphonics and Lorentz Force detuning – which will be discussed later in Section 3.5.3 – also static detuning is very prominent. From Slater's theorem (see Section 3.6) we know that a change of cavity volume may change the cavity's resonant frequency. Due to the mode-dependent focusing effect of rods and pole shoes this shift is different for all three QPR modes.

During commissioning of the QPR, a calibration method was extracted from simulations and measurements in order to calculate the gap between sample and pole shoes from the resonant frequency of the first quadrupole mode. The deviation Δg from the nominal value of $g_0 = 500\,\mu\mathrm{m}$ is given by

$$\Delta g = (418.3\,\mathrm{MHz} - f_{\mathrm{meas}}) \cdot 105.3\,\frac{\mu\mathrm{m}}{\mathrm{MHz}} - 75\,\mu\mathrm{m} \tag{3.2}$$

with f_{meas} denoting the measured frequency of Q1[1] at room temperature and equal pressure inside and outside the resonator.

[1] The resonant frequency of quadrupole modes can vary by several MHz. To avoid ambiguities, the abbreviation Qn is used denoting the n-th quadrupole mode.

This condition is typically given immediately after mounting the sample or inside the evacuated cryostat before cool-down. $\Delta g > 0$ corresponds to an increased gap. The value of g is then used to obtain the RF field calibration constants c_1, c_2 and G for all three quadrupole modes that are needed for further RF measurements (see e.g. Sections 3.3.1 and 3.6). Analytic expressions to calculate c_1, c_2 and G as a function of g can be found in the Appendix (see Section A.3).

Close to the third quadrupole mode two other eigenmodes exist which vary only slightly with gap height g. Experience showed deviations in the frequency of Q3 of up to 9.1 MHz, while the frequency of neighboring modes at 1275.8 MHz and 1287.0 MHz varied by less than 400 kHz. As a result, the mode order of Q3 and the one at 1287 MHz can swap, possibly causing ambiguity errors. Fig. 3.6 shows RF mode scan data near Q3 for three different measurement runs, measured using a vector network analyzer (VNA). Data on the full frequency span from 400 MHz to 1.46 GHz can be found in the Appendix (see Section A.1).,

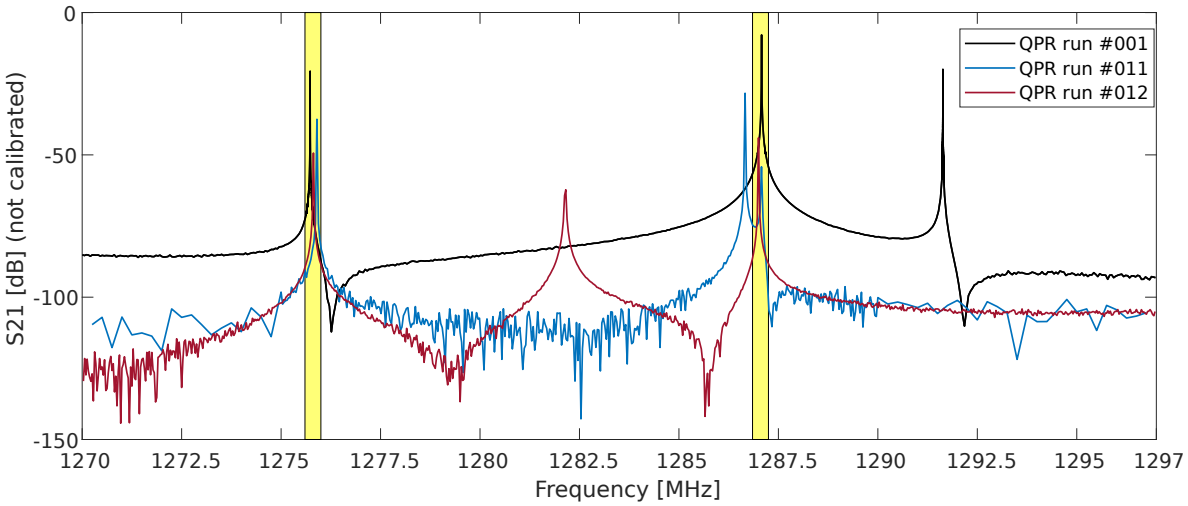

Figure 3.6: *VNA mode scans near Q3 for three different measurement runs. The two neighboring cavity modes stay nearly the same – highlighted yellow – while the quadrupole mode shifts significantly. All data was taken under comparable conditions at $T = 1.8\,K$.*

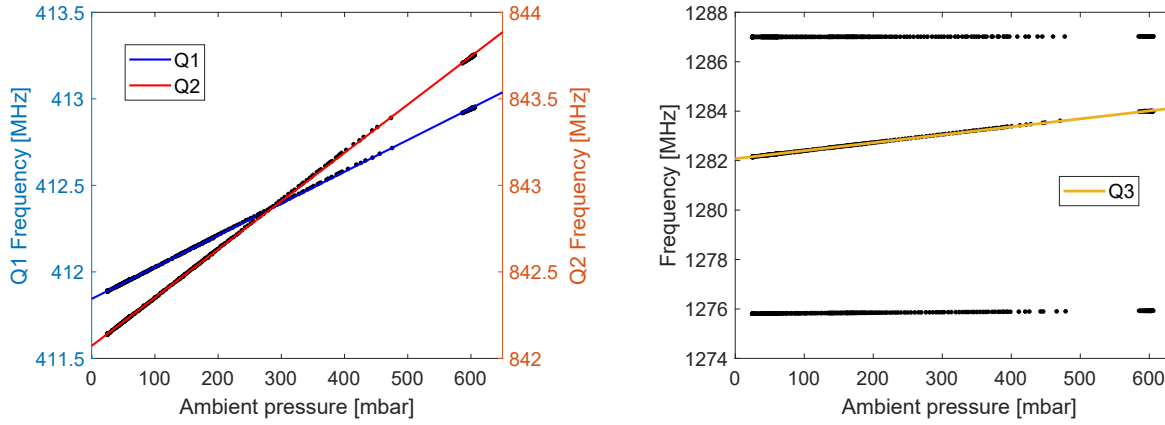

(a) df/dp of Q1 and Q2 *(b) df/dp of Q3 and neighboring modes*

Figure 3.7: *Shift of resonant frequencies with ambient pressure. Data is obtained from VNA measurements during pump-down after helium refill (QPR run #012). The abscissae contain both, gas pressure and hydrostatic pressure acting on the cavity. Linear fits are shown for the quadrupole modes only, the hydrostatic pressure is calculated relative to the cavity center using Eq. 3.3.*

The strong dependence of quadrupole mode frequencies on the distance between sample and rods together with the cylindrical shape of the QPR cavity defines the sensitivity to ambient pressure. Fig. 3.7 shows measurement data of resonant frequencies vs. ambient pressure. Using linear fits, the sensitivity to ambient pressure $\mathrm{d}f/\mathrm{d}p$ is derived. The uncertainties given in Tab. 3.2 state the $1\,\sigma$ uncertainty of the fits. Compared to elliptical TESLA-shaped cavities ($\mathrm{d}f/\mathrm{d}p = 10\,\mathrm{Hz/mbar}$ [40]) the values obtained for quadrupole modes are higher by a factor 180 to 320. Earlier measurements on Q1 gave a value of 2.6 kHz/mbar [80]. As indicated by the fit uncertainties given in Tab. 3.2, $\mathrm{d}f/\mathrm{d}p$ can be determined with high precision. However, this only holds for unchanged ambient conditions for the time of one measurement run. During sample change and the final assembly for cool-down the pre-stress on the cavity coming from its holding frame can vary significantly. This explains the discrepancy of $\mathrm{d}f/\mathrm{d}p$ values obtained during different measurement runs. For that reason, data correction procedures requiring this quantity cannot rely on values obtained from another run without introducing significant uncertainty. This is especially relevant for measurements of the penetration depth (see Section 3.6).

Table 3.2: *Sensitivity of resonant frequency to ambient pressure and liquid helium level for different RF modes, measured during QPR run #012. Error bars give statistical fit uncertainty only.*

Frequency [MHz]		412 (Q1)	842 (Q2)	1275	1282 (Q3)	1278
$\mathrm{d}f/\mathrm{d}p$	[Hz/mbar]	1836 ± 1	2789 ± 2	204 ± 1	3226 ± 3	40.1 ± 0.2
$\mathrm{d}f/\mathrm{d}l$	[Hz/%]	399.2 ± 0.2	606.3 ± 0.4	44.4 ± 0.2	701.3 ± 0.7	8.72 ± 0.04

During operation in a vertical bath cryostat, the liquid helium level and hence the hydrostatic pressure on the cavity decreases. This effect changes the ambient pressure by

$$\Delta p = \Delta h \cdot \rho \cdot g = \Delta h[\%] \cdot 15.24 \,\frac{\mathrm{mm}}{\%} \cdot \rho(1.8\,\mathrm{K}) \cdot g \approx 0.22 \,\frac{\mathrm{mbar}}{\%} \cdot \Delta h\,[\%] \tag{3.3}$$

which yields a significant dependence of the operating frequency on the liquid helium level $\mathrm{d}f/\mathrm{d}l$ (see Tab. 3.2).

During operation the identification of the quadrupole modes from VNA measurements is essential. Given by the mode separation at Q1 and Q2, ambiguity errors are excluded (see Appendix Figs. A.1 and A.2). A good method to unanimously identify Q3, is to perform VNA scans during pump-down. Looking at the range $(1285 \pm 10)\,\mathrm{MHz}$, the mode with the largest $\mathrm{d}f/\mathrm{d}p$ is the quadrupole mode.

The pressure sensitivity of the QPR could be directly compensated by an external tuning mechanisms acting on the cylindrical sidewalls of the cavity. Experiments with a titanium clamp squeezing the cavity increased the frequency of Q1 by about 50 kHz. This would probably be sufficient to compensate $\mathrm{d}f/\mathrm{d}l$ during measurements. Another commonly used tuning mechanism for SRF cavities is given by piezo actuators. Their successful application to the QPR for microphonics detection was shown in [85]. Active excitation of the quadrupole rods represents another promising way to compensate even dynamic detuning.

3.3 Measuring RF Surface Resistance

The main purpose of the QPR is to perform precision measurements of the RF surface resistance at different frequencies and as a function of temperatures and RF field strengths. The comparatively low frequency of the first quadrupole mode provides high sensitivity to residual resistance at low sample temperature. This aspect is difficult to access with other sample test systems, which generally must operate at higher frequency where the BCS resistance tends to dominate. Furthermore, the surface resistance is measured with a calorimetric compensation technique enabling absolute measurements without the need for cross-calibration to a reference sample.

3.3.1 Calorimetric Measurement Technique

The calorimetric measurement principle uses an RF-DC compensation technique consisting of three steps:

1. Without RF field, the sample is heated to a temperature of interest until thermal equilibrium is reached. The required heater power is recorded by measuring heater current and voltage drop across the heater using a 4-wire setup. This power level P_{DC1} is also denoted DC reference power $P_{\mathrm{reference}}$.

2. The RF is switched on to the power level of interest and a PID control loop reduces the heater power to stabilize the temperature of interest again (P_{DC2}).

3. Once thermal equilibrium is reached, the RF dissipated power is given by the difference in heater power $P_{\mathrm{diss}} = \Delta P_{\mathrm{DC}} = P_{\mathrm{DC1}} - P_{\mathrm{DC2}}$.

The average surface resistance is then given by

$$R_{\mathrm{S}} = \frac{2P_{\mathrm{diss}}}{\iint_{\mathrm{sample}} |H|^2 \,\mathrm{d}S} = 2\, c_1\, \mu_0^2 \frac{\Delta P_{\mathrm{DC}}}{B^2_{\mathrm{sample,\ pk}}} \tag{3.4}$$

with the RF calibration constant

$$c_1 = \frac{B^2_{\mathrm{sample,\ pk}}}{\iint_{\mathrm{sample}} |B|^2 \,\mathrm{d}S}. \tag{3.5}$$

As usual for cavity measurements, the peak RF magnetic field on the sample $B_{\mathrm{sample,\ pk}}$ is derived from the measured RF power level at the pickup antenna P_{t} according to

$$B_{\mathrm{sample,\ pk}} = \sqrt{\frac{c_2\, Q_{\mathrm{ext}}\, P_{\mathrm{t}}}{\omega}} \tag{3.6}$$

with the second constant

$$c_2 = \frac{B^2_{\text{sample, pk}}}{U} \tag{3.7}$$

and the stored energy

$$U = \frac{Q_{\text{ext}} P_{\text{t}}}{\omega}. \tag{3.8}$$

The calibration constants for each quadrupole mode are obtained from simulations [80] and corrected for the actual gap distance between sample and pole shoes according to Eqs. 3.2 and A.2–A.4.

Obviously, the surface resistance measurement is restricted to a regime where $P_{\text{diss}} < P_{\text{reference}}$. To increase the measurable RF field range, pulsed RF power is used. Pulse period and duty factor have to fulfill certain criteria:

- The pulse period must be short enough to ensure a constant sample temperature (sufficient thermal "inertia" of the sample system)
- Individual pulses need to be long enough that the contribution from rising and falling edges to RF losses is much less than the constant part of the pulse. Note that precise recording and integration of the pulse shape would be possible with the available power meters. However, field-dependent surface resistance that is intrinsically unknown might cause significant systematic errors. In case of "usual" Q-slope the resulting surface resistance would be underestimated.
- Due to the susceptibility of the QPR to mechanical oscillations, Lorentz force detuning can trigger microphonic detuning. Hence, the pulse repetition rate should not trigger any mechanical resonance or an integer harmonic of it. In the present case the resonance at 100 Hz is most severe.

For standard operation, a pulse period of 133 ms and duty factors down to 30 % are used, providing reliable results.

3.3.2 Resolution, Accuracy and Precision

The measurement precision of the QPR was discussed in earlier work (see [80]). However, significant parts of the setup were changed in the meantime and certain assumptions were revised. Hence, a new assessment is presented here. In general, the surface resistance measurement uncertainty depends on properties of the sample such as its thermal conductivity and the surface resistance itself. For that reason, no ultimate quantitative analysis can be provided. Nevertheless, certain summarizing statements are given in Tab. 3.3, based on realistic assumptions as discussed in the further course of this section.

Table 3.3: *Summary of surface resistance measurement uncertainties and limitations. Details and underlying assumptions are discussed in the further course of this section, see text and figures as given in the column "References".*

Quantity	Value	References
Typical accuracy of R_S w/o bias	9.2 %	pp. 47f.
Minimum resolvable R_S	0.5 nΩ at $B_{RF} = 10$ mT in general: 50 nΩ(mT)^2	p. 41
Systematic bias of R_S at Q3	> 25 nΩ	Figs. 3.18 and 3.19
Systematic uncertainty of R_S due to temperature gradients	< 1 %	Section 3.3.3, Fig. 3.24
Calorimetric accuracy of heater power measurement	< 0.3 %	pp. 36ff., Fig. 3.9
Minimum RF field level (B_{RF})	5 mT	Fig. 3.20
Accuracy of B_{RF}	6.5 %	pp. 47f.
Vertical ΔT between RF surface and temperature sensor	< 5 mK	Section 3.3.3, Fig. 3.23

Uncertainty of the Heater Power Measurement A LakeShore LS336 device is the central unit of the calorimetric measurement. It can power two DC heaters and read out four temperature sensors. The output of the internal PID controller is a variable current source with 16-bit digital resolution. In the worst case (highest value of maximum current), one bit of the DAC corresponds to a current step of 30.5 µA or a 47 nW step in heater power at a load resistance of 50 Ω. The RMS noise of the current source of 0.12 µA is negligible.

During commissioning of the QPR, the heater power was derived only from the measured voltage drop across the heater, assuming a constant resistance. However, measurements show that the stability of the resistance is only on the level of a few percent which can easily be improved by simultaneously measuring the current flowing through the heater and the corresponding voltage drop. Furthermore, this provides a safety procedure since the heater resistance is monitored to prevent overheating and to detect insulation failures. Both ends of the heater's resistive part are equipped with a pair of wires, enabling a precise measurement of only the relevant voltage

drop across the heater. The heater current is measured with a Keithley 2100 multimeter. It has a resolution of at least 1 µA which is sufficiently better than the D/A resolution of the current source. The accuracy of the device limits the overall current accuracy to about 0.3 % in the worst case. The heater voltage is measured with an HP 34401A multimeter having a worst case accuracy of better than 660 µV. This is below the step size defined by the current source $V_{\text{step}} = 50\,\Omega \cdot 30.5\,\mu\text{A} = 1.5\,\text{mV}$ and hence no limitation of the measurement system. However, voltage noise coming from electromagnetic interference may disturb the voltage measurement.

Fig. 3.8 shows the relative accuracy of current and voltage measurements. The resulting heater power accuracy for two exemplary values of heater resistance (50 Ω and 200 Ω) is given in Fig. 3.9. Typically, a heater with $R \approx 50\,\Omega$ is used for measurements. After the discussion of helium bath stability and the introduction of a thermal simulation model, the electronic accuracy as a function of sample temperature is given in Fig. 3.13.

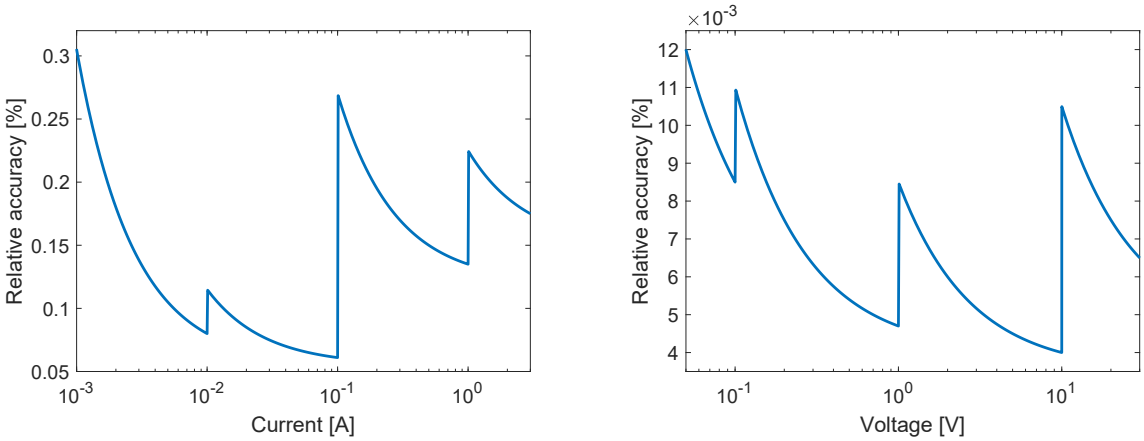

Figure 3.8: *Relative accuracy of current and voltage measurement. Steps occur when the measurement device switches its range setting.*

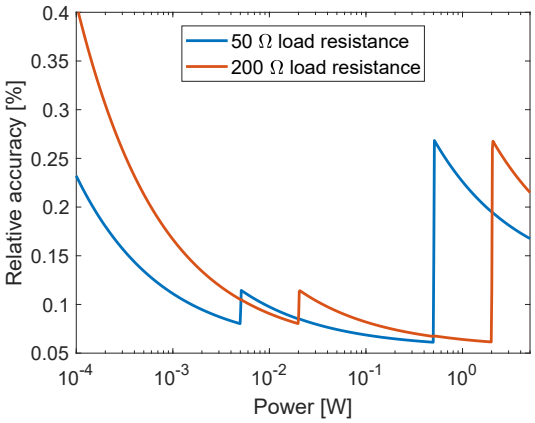

Figure 3.9: *Relative accuracy of the heater power measurement.*

Helium Bath Stability The pressure stability of the liquid helium bath has direct influence on the heater power and hence the thermometry precision. Measurements show that the pressure fluctuations of the vertical bath cryostat depend on the helium level, increasing from ±40 µbar at 60 % helium level up to ±80 µbar at 10 % level (see Fig. 3.10). At the operating temperature of 1.8 K this maximum value corresponds to a variation in bath temperature of ±1.4 mK [86]. For a detailed measurement of the helium pressure, both measurement and time resolution of the sensor are limited. This becomes visible in Fig. 3.10 by stepwise changing data determined by the bit resolution of the available analog-to-digital converter. By operating the QPR at constant field, the resonant frequency measured by the frequency counter of the PLL system (see Section 3.2.2) can be used to monitor changes of helium pressure with higher time resolution as shown in Fig. 3.11. A value of $\Delta f = \pm 100$ Hz corresponds to ±54 µbar (see Tab. 3.2). The sample temperature responds with a delay of 10 seconds given by the thermal inertia of sample chamber and liquid helium bath. This delay is about one quarter of the oscillation time constant, reducing the measured ΔT on the sample to only ±0.6 mK.

During measurements, the sample temperature is actively controlled which transforms temperature changes of the LHe bath into heater power changes ΔP_{heater}. Using COMSOL Multiphysics® [87] a thermal simulation of the sample chamber system was set up (see later this section) and the temperature boundary condition given by the LHe bath is varied by 1.4 mK. Comparing the required heater power to achieve a certain sample temperature for both scenarios leads to ΔP_{heater} on the order of 20 µW as shown in Fig. 3.12. Obviously, this error source limits the entire setup at sample temperatures that are very close to the helium bath temperature. For a $T \gtrsim 1.825$ K the resulting error is less than 6 %, quickly dropping with increasing temperature (see Fig. 3.13). By using a sufficiently long averaging data set of several minutes, the impact of the helium bath on the heater power measurement can be suppressed further.

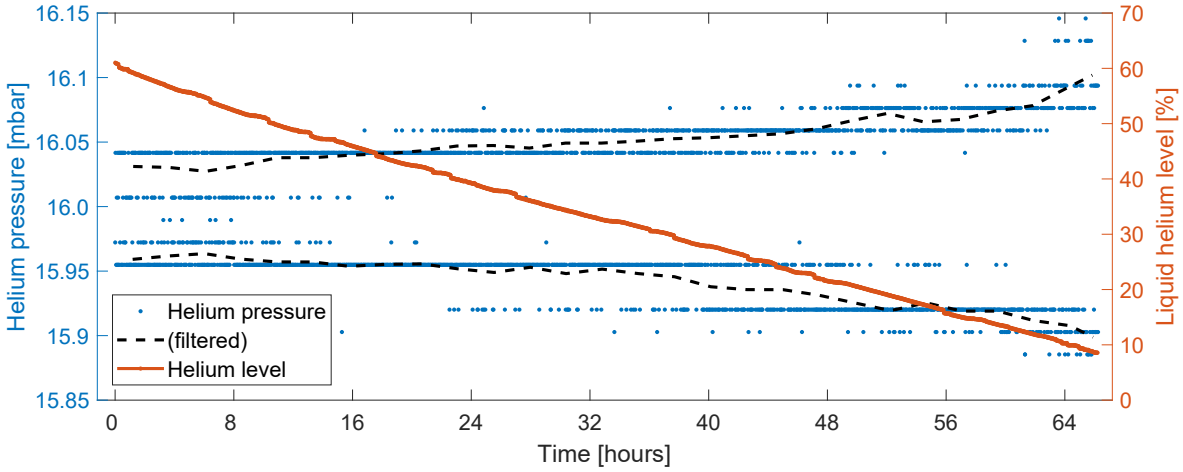

Figure 3.10: *Helium pressure and liquid level vs. time. Time and bit resolution of the pressure sensor are not sufficient to fully capture the occurring fluctuations. A moving average filter is shown for upper and lower halves of the pressure data sets (black dashed lines), highlighting the decreasing pressure stability with helium level.*

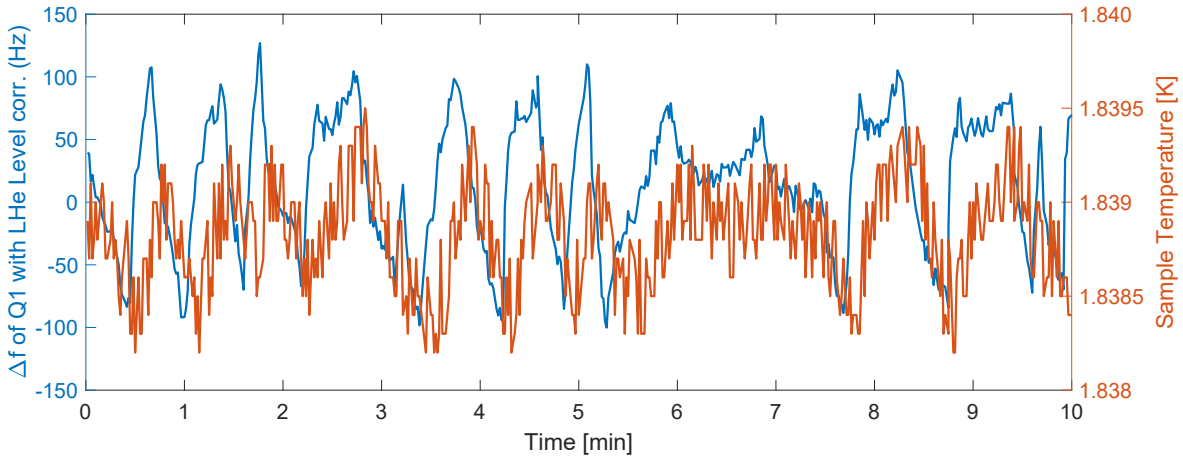

Figure 3.11: *Deviations of resonant frequency and sample temperature vs. time. During this measurement the sample heater was switched off and the long-term drift of frequency with helium level is corrected.*

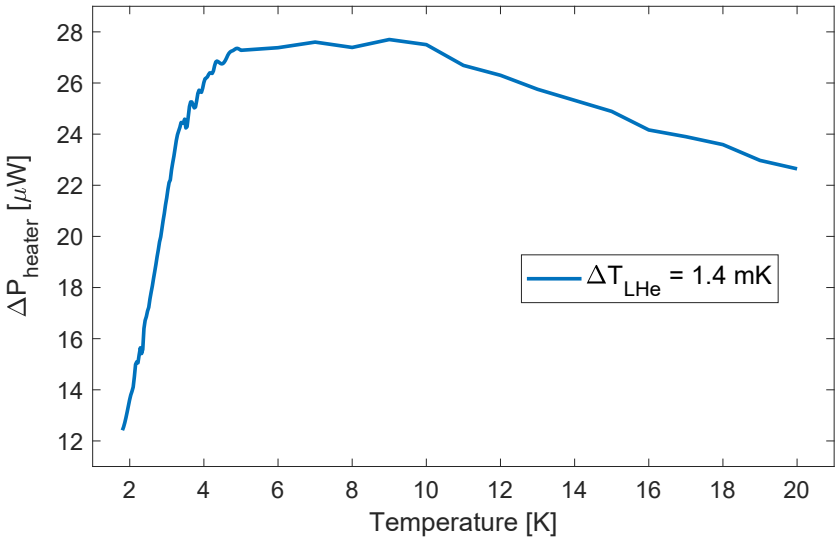

Figure 3.12: *Impact of fluctuating helium bath temperature on the required heater power to achieve a given sample temperature.*

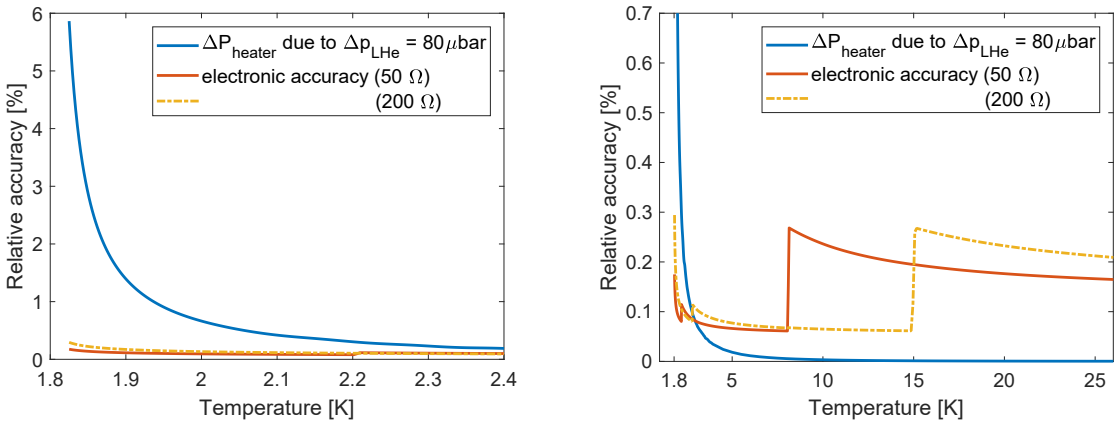

Figure 3.13: *Relative accuracy of the calorimetric system due to read-out electronics and helium bath stability. For the electronic accuracy, the power axis of Fig. 3.9 is transformed to temperature using the thermal simulation model mentioned above.*

Minimum Resolvable Surface Resistance The minimum resolvable surface resistance is of interest at very low sample temperatures. Due to the at some point negligible BCS contribution, this directly translates to the minimum resolvable residual resistance that can be measured directly. Fitting data for surface resistance vs. temperature might yield a lower residual resistance, however, deviations from the implied theoretical model cannot be resolved in that case. At sample temperatures close to the helium bath temperature, measurements are not limited by the smallest resolvable change in heater power – as that would only be 47 nW and hence correspond to an incredibly low surface resistance – but by the equivalent heater power change due to helium pressure fluctuations. Using Eq. 3.4, a value of 12 µW (see Fig. 3.12 at lowest temperature) yields $R_S = 0.5\,\mathrm{n\Omega}$ at $B_{\mathrm{sample}} = 10\,\mathrm{mT}$, decreasing quadratically with RF field to ultimately $R_S = 0.003\,\mathrm{n\Omega}$ at the QPR quench limit of $B_{\mathrm{sample}} = 120\,\mathrm{mT}$. In general, the resolution parameter

$$R_{S,\mathrm{min}} B_{\mathrm{RF}}^2 = 2\, c_1\, \mu_0^2\, \Delta P_{\mathrm{DC,min}} = 50\,\mathrm{n\Omega(mT)}^2 \tag{3.9}$$

can be defined. The values above apply to Q1, for higher harmonic modes the minimum resolvable surface resistance increases by about 20 % due to the increasing c_1 parameter (see Eq. 3.5 and Appendix Section A.3). Note that only the RF contribution via c_1 is an intrinsic property of the resonator. Decreasing the thermal conductivity of the sample chamber reduces the DC heater power that is required to compensate temperature fluctuations caused by the liquid helium bath. In that case, the resolution is improved, ultimately limited by the temperature sensor readout resolution of 0.1 mK and the corresponding heater power response in closed-loop PID operation. Currently, measurements of low surface resistance are limited by parasitic RF heating to significantly higher values. This effect is discussed in the following section.

Measurement Bias due to Parasitic Losses – or "Missing Power" Up to now, the lowest surface resistance measured with the QPR at HZB was 8 nΩ at 2.25 K and Q1 on a RRR 300 bulk niobium sample [80]. Especially at the third quadrupole mode consistent results have not been obtained so far. One reason for this is insufficient damping of RF field in the coaxial structure of the sample chamber. In the calorimetric RF-DC compensation technique all RF losses occurring on the sample chamber are interpreted as surface resistance of the sample, and hence lead to a systematically overestimated R_S. Earlier work on simulations of the RF losses at the stainless steel bottom flange of the sample chamber predicts a systematic bias of 4.6 nΩ at the first quadrupole mode [80]. In the following, the effect of unwanted heating and surface resistance bias is studied for the sample design introduced in Section 3.4 and at all three relevant quadrupole modes.

In terms of RF dissipation the sample chamber is divided into three domains: Sample surface, coaxial wall and bottom flange. Using the eigenmode solver in CST MWS, the RF fields inside the QPR are simulated and the damping coefficient

$$\delta_i = \frac{\iint_{\text{sample}} |H|^2 \, \mathrm{d}S}{\iint_i |H|^2 \, \mathrm{d}S} \tag{3.10}$$

is evaluated for each domain and each quadrupole mode, where the surface integral in the denominator is taken of the domain i. The dissipated power in each domain is then given by

$$P_i = \frac{1}{\delta_i} \frac{R_i}{R_{\text{sample}}} P_{\text{sample}} = \frac{\gamma_i}{R_{\text{sample}}} P_{\text{sample}} \tag{3.11}$$

introducing the loss coefficient $\gamma_i = \frac{R_i}{\delta_i}$. R_i denotes the surface resistance of a domain.

Table 3.4: *RF parameters describing the additional losses on coaxial wall and bottom flange. The surface resistance of stainless steel is calculated using the normal skin effect with $\sigma = 2 \cdot 10^6\,(\Omega\mathrm{m})^{-1}$ at cryogenic temperatures [88].*

	Q1 (433 MHz)	Q2 (866 MHz)	Q3 (1315 MHz)
δ_{coax}	207.7	212.1	217.0
δ_{flange}	$1.4 \cdot 10^6$	$1.0 \cdot 10^6$	$5.7 \cdot 10^5$
$R_{\text{S, SS304}}$	29 mΩ	41 mΩ	51 mΩ
γ_{flange}	21.2 nΩ	40.7 nΩ	89.0 nΩ

Compared to earlier work on this structure, the damping coefficient δ_{flange} at 433 MHz is lower by a factor 4.5 [80], leading to a significantly higher contribution of the flange. Due to the narrow width but large surface of the coaxial structure the required number of mesh cells and hence the computational effort is very high. Considering this discrepancy and possible numerical uncertainty, the obtained values of δ are scaled by a factor $x = \{1; 2; 4.5\}$. Fig. 3.14 shows the resulting ratio of dissipated power at the flange to the power dissipated in the sample. At a given temperature, the heater power ratio increases linearly with x. The necessary $R_{\text{S}}(T)$ is calculated using the numerical BCS code SRIMP [43] for niobium with RRR 300 and $R_{\text{res}} = 10\,\text{n}\Omega$. The surface resistance of stainless steel is assumed to be independent of temperature (see Tab. 3.4). Compared to P_{flange}, the contribution of the coaxial wall can be neglected: Assuming non-ideal niobium with 10 times higher residual resistance yields $\frac{P_{\text{coax}}}{P_{\text{sample}}} = 5\,\%$ at low temperature, further decreasing to 0.5 % in the regime of dominating BCS losses. Note that in this case higher frequencies are less affected by the coax.

The loss coefficient γ_i as defined above is given in units of resistance (or nΩ) and seems to give a resistance contribution. However, this not fully true since the RF-DC compensation technique cannot measure RF dissipation directly but compares power levels at constant temperature. Hence, the temperature rise or the distortion of the temperature distribution on the sample

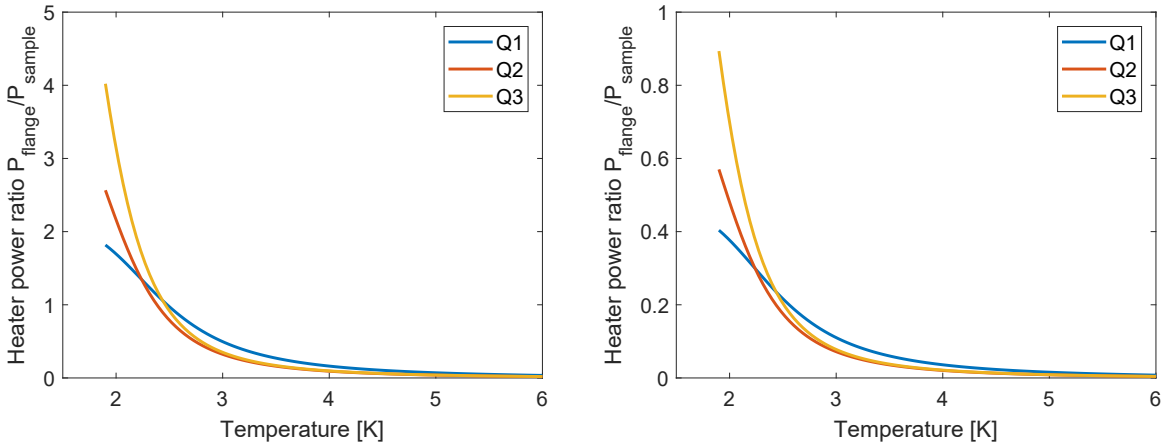

(a) $x = 1$ *(b)* $x = 4.5$

Figure 3.14: *Ratio of RF dissipated power on the normal conducting bottom flange and a niobium sample with 10 nΩ residual resistance. The damping coefficient δ_{flange} is scaled by a factor x to study numerical uncertainties. $x = 4.5$ approximately reproduces the RF loss ratio of 50 % at low temperature and Q1 as calculated in [80].*

chamber has to be evaluated which then yields the surface resistance contribution. In order to do so, a thermal simulation of the sample chamber introduced in Section 3.4 using COMSOL Multiphysics® is set up. The temperature dependent thermal conductivities of all materials are considered, data is taken from [88–91]. For technical details on the simulation see Appendix Section A.8. A sketch of the simulation geometry and one exemplary temperature map is shown in Fig. 3.15. The resonator itself does not have to be taken into account since sample chamber and resonator are thermally decoupled (see Section 3.1). For now, the problem is simplified to axial symmetry. Concerning RF heating this simplification will be given up later for a detailed analysis of thermal gradients on the sample surface (see Section 3.3.3). Three external heat sources are implemented: The central DC heater below the RF sample surface, RF heating of the sample on an annulus covering the region of highest magnetic field and RF heating of the bottom flange. The cooling by superfluid liquid helium is implemented using a fixed temperature boundary condition ($T = 1.8\,\mathrm{K}$) at the outer surfaces touching the liquid. Thermal boundary resistance and the large but finite thermal conductivity of superfluid helium is neglected. Fig. 3.16 shows simulated and measured data of sample surface temperature as a function of DC heater power. The different measurement runs correspond to three different sample chambers, including also a demountable setup (run 09, see also Section 3.4). For that reason, the thermal simulation describes a typical scenario that is not limited to a specific sample.

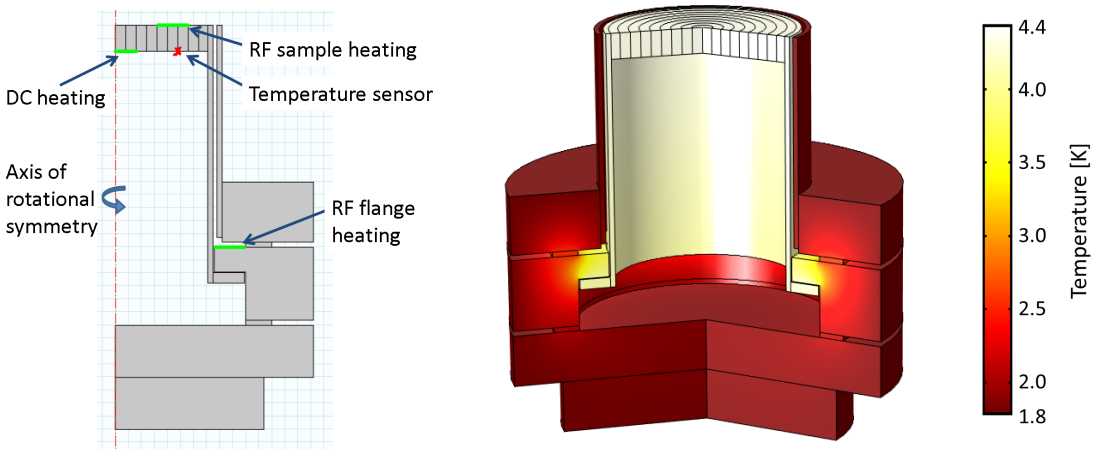

Figure 3.15: *Left: Sketch of the simulation geometry. Locations of boundary heat sources are highlighted in green, the position of the reference temperature sensor is indicated by a red X. Right: Exemplary 3D temperature map for a DC heater power of 100 mW.*

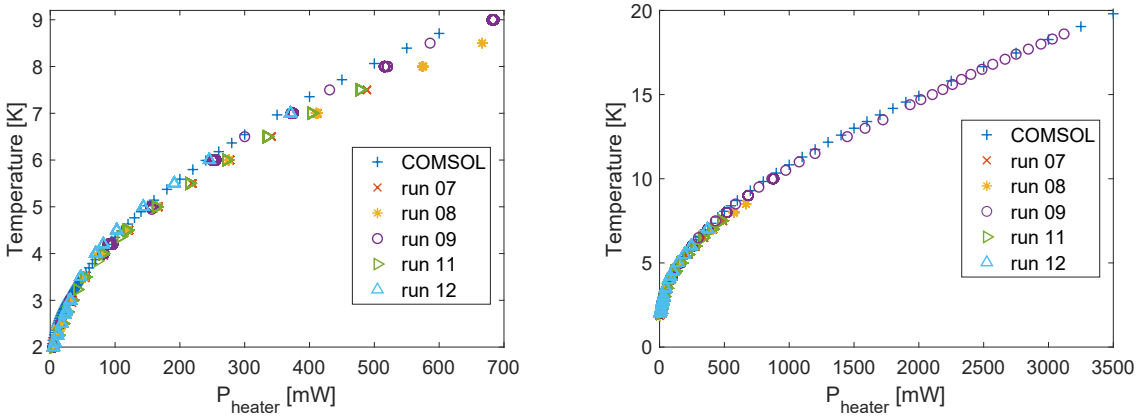

Figure 3.16: *Simulated and measured sample temperature vs. DC heater power.*

In order to estimate the impact of parasitic heating on the measured values of surface resistance, all data acquisition steps are translated to COMSOL. First, a parameter scan in heater power is computed using only the central heater at the sample bottom. Compared to measurement data this verifies the model and the thermal conductivities (see again Fig. 3.16). The resulting data points are interpolated to obtain the required reference power $P_{\mathrm{reference}}(T)$ for any sample temperature of interest. In a second step RF heating is computed at multiple combinations of total power and relative ratio of RF power heating the sample to RF dissipation on the bottom flange. The resulting dataset is again interpolated and provides now possible distributions of heater power and RF dissipation for a given value of sample temperature. For the surface resistance accuracy the worst case occurs if all heating comes from RF dissipation, hence the DC heater is off and $\Delta P_{\mathrm{DC}} = P_{\mathrm{reference}}$. The corresponding RF field is calculated according to Eq. 3.4 with the true $R_{\mathrm{S}}(T)$ from SRIMP and the true RF dissipation on the sample surface. Fig. 3.17

shows one exemplary set of RF field values for $R_{\mathrm{res}} = 10\,\mathrm{n\Omega}$ and baseline damping coefficients from Tab. 3.4 ($x = 1$). Obviously, parasitic heating at the bottom flange causes a severe limitation in accessible RF field in the very important temperature range $T \leq 4.2\,\mathrm{K}$. Taking now the values of B_{sample} and the corresponding worst-case condition of $\Delta P_{\mathrm{DC}} = P_{\mathrm{diss}} = P_{\mathrm{reference}}$ results in a surface resistance that is overestimated systematically due to the losses at the bottom flange. Fig. 3.18 shows this systematic overestimation for the RF damping coefficients δ_i ($x = 1$) as calculated in this work. Again, for the sample a surface resistance of RRR 300 niobium with $R_{\mathrm{res}} = 10\,\mathrm{n\Omega}$ is assumed. In Fig. 3.19 the same calculation is repeated for higher RF damping given by simulation scaling factors $x = 2$ or 4.5.

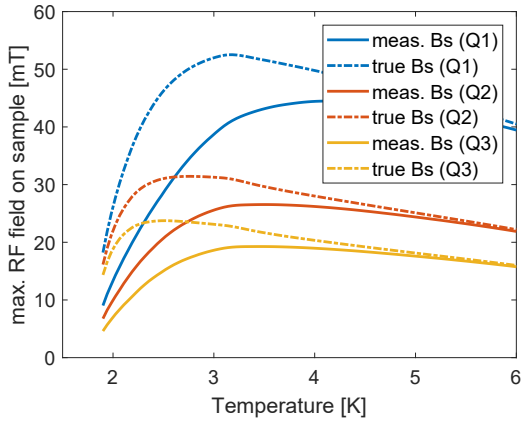

Figure 3.17: *Maximum possible RF field for the case that all heating comes from RF dissipation. Dashed lines show the ideal case of no additional heating at the bottom flange.*

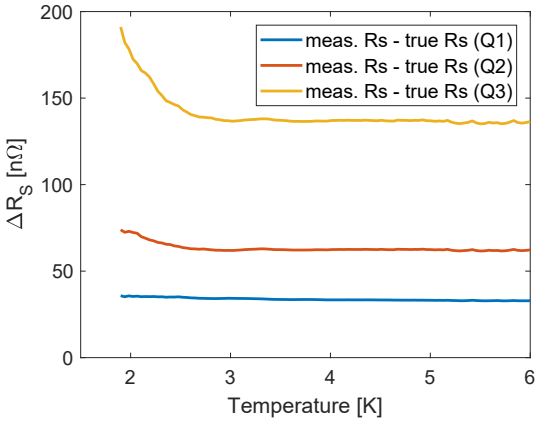

Figure 3.18: *Systematic errors in R_S measurements due to RF dissipation inside the coaxial structure. A niobium sample with RRR 300 and $R_{res} = 10\,n\Omega$ was assumed.*

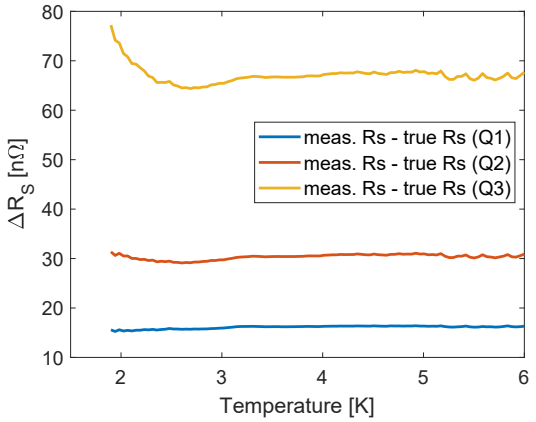

(a) $x = 2$

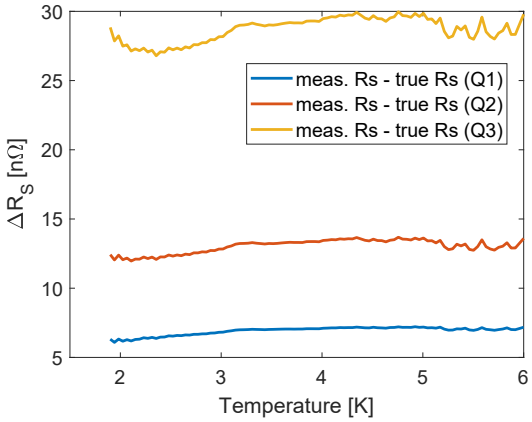

(b) $x = 4.5$

Figure 3.19: *Systematic errors in surface resistance measurements for a RRR 300 niobium sample with $R_{res} = 10\,n\Omega$ and different simulation scaling factors x. Higher values of x correspond to stronger damping of RF fields inside the coaxial structure and hence less systematic errors.*

For temperatures above 4.5 K increasing numerical noise is observed, especially at high frequency and strong coaxial damping (high x). This is due to the steep increase of BCS surface resistance on the sample surface and hence vanishing power ratio of flange heating to sample heating. The impact of ΔR_S gets negligible since its relative contribution decreases below the overall measurement accuracy.

A systematic error larger than 10 nΩ at low temperature and Q1 is not compatible with measurement results obtained so far. However, the simulation assumes maximum RF field representing the worst case. For lower RF field non-zero $P_{\mathrm{DC}2}$ reduces effectively the ratio of flange heating to sample heating and hence the systematic offset error. On the other hand this leads to an artificial Q-slope with increasing R_S for higher RF fields. Looking at the error as a function of temperature yields ΔR_S with slopes of different sign depending on the scaling x and hence the coaxial damping. Counter-intuitively, the normal conducting flange with a surface resistance independent of temperature and RF field does not only contribute as additional residual resistance but may also impact the BCS behavior of the measured surface resistance.

In order to suppress this significant systematic error, the surface resistance of the bottom flange has to be reduced. Options might be copper or superconductor coating of the areas exposed to RF or even the use of a bulk superconducting flange. For high-quality copper at low temperature the anomalous skin effect applies [8] resulting in a surface resistance of

$$R_{\mathrm{S,\,anom.}} = \left[\sqrt{3}\pi \left(\frac{\mu_0}{4\pi}\right)^2\right]^{1/3} \omega^{2/3} \left(\rho\ell\right)^{1/3} = 1.3\,\mathrm{m\Omega} \tag{3.12}$$

at 1.3 GHz with $(\rho\ell) = 6.7 \cdot 10^{-16}\,\Omega\mathrm{m}^2$ [92]. Studies of copper plating on RF couplers showed that for a thickness of 10 µm the achievable RRR is only about 15 to 50, depending on the coating procedure [93]. However these values already provide $R_\mathrm{S} < 2.5\,\mathrm{m\Omega}$ [8], post-coating annealing may increase the RRR to better than 100 [94]. In the anomalous limit, RF losses on the flange will be suppressed by about a factor 40 compared to stainless steel. This can be exceeded by far when using superconducting surfaces such as coatings of lead or niobium or a bulk superconducting flange of NbTi. Then, the lowest detectable true surface resistance will be determined by losses on the cylindrical wall surface of the sample chamber. In case of niobium samples this seems manageable. However, additional complications arise for multilayer coatings and measurements at high temperatures: The Nb_3Sn sample discussed later (see Chapter 4) is coated on all exterior surfaces, hence a scenario of sidewall losses similar to bulk niobium is expected. With sputtered coatings as for the S-I-S′ sample (see Chapter 5), high quality coatings of the sidewalls are complicated if not impossible. In this case, the bare niobium substrate will cause a temperature dependent increase of R_S and impede measurements above 9.25 K.

From a numerical point of view the basic assumption of the RF-DC compensation method – namely that both kinds of heating cause the same temperature response at the reference sensor location – is violated by power "missing" on the sample. Looking at the geometry as a rotationally symmetric two-dimensional problem requires that no heating may occur between the reference temperature sensor and the liquid helium bath. When fulfilling this condition, the heat flux – coming from arbitrary sources – passing the sensor location equals the total heat flux and always produces the same temperature rise towards the liquid helium bath. RF heating at the bottom flange obviously violates this requirement. As we will see later (see Section 3.3.3 and esp. Fig. 3.22), the RF-DC compensation method works for BCS-distributed RF losses even for a temperature sensor located at the bottom of the RF surface. In case of defects, multipacting or excessive heating near the sample edges, the true dissipated power – and hence the surface resistance – will again be overestimated. To minimize this risk, the reference temperature sensor at the sample should be placed on the biggest radius possible, i.e. as close as possible to the outer edge of the RF surface.

RF Measurement Accuracy and Overall Surface Resistance Accuracy For the calculated surface resistance the accuracy of the RF power measurement contributes significantly. In the experimental setup Keysight U2042XA power meters are used that have an accuracy of $\pm 0.18\,\mathrm{dB}$ or $\pm 4.1\,\%$ for all relevant frequencies and power levels. In addition, approximately $0.2\,\mathrm{dB}$ have to be added due to the uncertainty of RF cable losses, yielding an overall uncertainty of $0.4\,\mathrm{dB}$ or $9.2\,\%$. This is a typical value for RF measurements [95], for the conversion of errors on the dB scale to % see e.g. [96].

Using Eq. 3.4, the propagation of uncertainties is given by

$$\sigma_{R_\mathrm{S}}^2 = \left(\frac{\partial R_\mathrm{S}}{\partial P_\mathrm{DC}}\right)^2 \sigma_{P_\mathrm{DC}}^2 + \left(\frac{\partial R_\mathrm{S}}{\partial Q_\mathrm{t}}\right)^2 \sigma_{Q_\mathrm{t}}^2 + \left(\frac{\partial R_\mathrm{S}}{\partial P_\mathrm{t}}\right)^2 \sigma_{P_\mathrm{t}}^2 \tag{3.13}$$

which yields the relative error

$$\left(\frac{\sigma_{R_\mathrm{S}}}{R_\mathrm{S}}\right)^2 = \left(\frac{\sigma_{P_\mathrm{DC}}}{\Delta P_\mathrm{DC}}\right)^2 + \left(\frac{\sigma_{P_\mathrm{DC}}}{\Delta P_\mathrm{DC}}\right)^2 + \left(\frac{\sigma_{Q_\mathrm{t}}}{2Q_\mathrm{t}}\right)^2 + \left(\frac{\sigma_{P_\mathrm{t}}}{2P_\mathrm{t}}\right)^2 = 2\left(\frac{\sigma_{P_\mathrm{DC}}}{\Delta P_\mathrm{DC}}\right)^2 + \frac{1}{2}\left(\frac{\sigma_\mathrm{RF}}{\mathrm{RF}}\right)^2 \tag{3.14}$$

assuming

$$\frac{\sigma_{Q_\mathrm{t}}}{Q_\mathrm{t}} = \frac{\sigma_{P_\mathrm{t}}}{P_\mathrm{t}} = \frac{\sigma_\mathrm{RF}}{\mathrm{RF}} = 9.2\,\%. \tag{3.15}$$

Note that in the discussion of heater power accuracy above we obtained $\frac{\sigma_{P_{\mathrm{DC}}}}{P_{\mathrm{DC}}}$ while for the surface resistance $\frac{\sigma_{P_{\mathrm{DC}}}}{\Delta P_{\mathrm{DC}}}$ is relevant. This is important for measuring R_{S} at low field or at high temperature where $\frac{\sigma_{P_{\mathrm{DC}}}}{\Delta P_{\mathrm{DC}}} = \frac{\sigma_{P_{\mathrm{DC}}}}{P_{\mathrm{diss}}}$ can become very large. Restricting the useful measurement range to $\sqrt{2}\frac{\sigma_{P_{\mathrm{DC}}}}{\Delta P_{\mathrm{DC}}} \leq \frac{1}{\sqrt{2}}\frac{\sigma_{\mathrm{RF}}}{\mathrm{RF}}$ sets a lower boundary on ΔP_{DC} and hence P_{diss}. For a given surface resistance this translates into a minimum RF field required for this measurement. Fig. 3.20 shows a simulation for RRR 300 niobium with 5 nΩ residual resistance. The values of 5 to 10 mT fit well to the experience from measurements of increasing spread in measured R_{S} data at this field level.

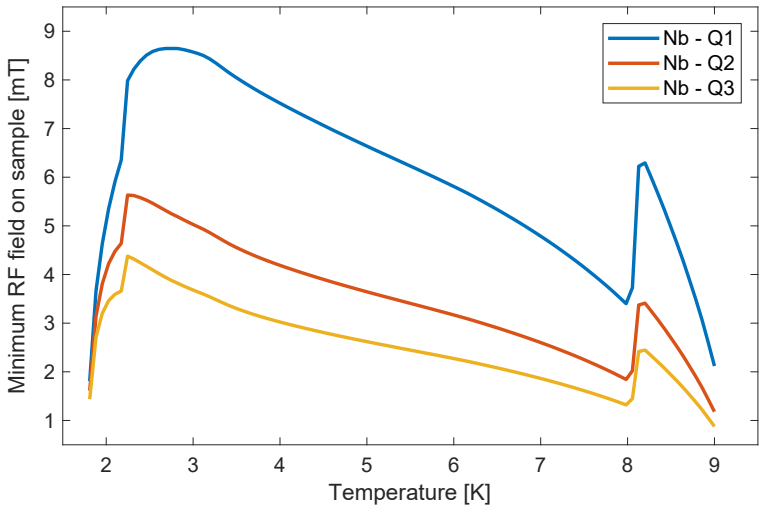

Figure 3.20: *Calculated minimum RF field level for $\frac{\sigma_{R_S}}{R_S} \leq 9.2\,\%$. $R_S(T)$ is calculated for RRR 300 niobium with $R_{res} = 5\,n\Omega$. Vertical jumps occur due to range switching of the ampere-meter (see Figs. 3.8 and 3.12).*

3.3.3 Gradients of Temperature and RF Field

The RF-DC compensation technique for surface resistance measurements relies on the assumption that any RF dissipation on the sample surface leads to the same thermal response as the exact same amount of DC heater power. As seen above, this assumption is violated e.g. by RF heating of additional parts of the sample chamber like the bottom flange. However, this effect can be suppressed by using superconducting material on all parts of the sample chamber and copper coating on the flange.

A second source of systematic error comes from asymmetries in sample heating and temperature gradients on the sample "disk". By construction, the PID controller relies on one temperature sensor at the bottom surface and the lateral distributions of heating (RF vs. DC) differ. This intrinsic property of the QPR is studied with another thermal simulation based on the one introduced before but without rotational symmetry (full 3D model). Two different DC heating scenarios are implemented:

1. Baseline design: Central DC heater with diameter 10 mm
2. Ring-shaped heater at $r_\mathrm{H} = 20 \ldots 32\,\mathrm{mm}$

Both heaters are still rotational symmetric. For RF dissipation the squared magnetic field on the sample surface is imported from CST MWS and used as boundary heat source. The reference temperature sensor is located on the sample bottom at $r = 24.1\,\mathrm{mm}$.

Fig. 3.22 shows exemplary results for 50 mW of heater power applied individually to the different boundary heat sources. The 2D temperature map on the sample surface due to the same amount of RF heating is given in Fig. 3.21.

Comparing the different scenarios of DC heating and RF heating in the high-field region yields a temperature response at the reference location ($r = 24.1\,\mathrm{mm}$) that is very similar. The deviation of 0.5 mK is close to the resolution limit of the temperature sensor ($\Delta T = 0.1\,\mathrm{mK}$). For the low field region a deviation of -2.5 mK is observed. This justifies the assumption of RF-DC compensation in case the sensor is mounted below a high-field region. Again, the curves for RF heating shown in Fig. 3.22 correspond to maximum RF field, and hence a worst-case scenario. Lower RF fields yield intermediate results with less temperature difference at the reference location.

The vertical temperature gradient across the thickness of the sample changes sign for DC and RF heating. Fig. 3.23 shows this effect vs. sample temperature. The ring-shaped DC heater produces a temperature profile which is similar to the RF heating but with inverse sign in gradient. For medium RF fields the gradients cancel each other yielding a temperature distribution that is nearly homogeneous in both dimensions, horizontally and vertically.

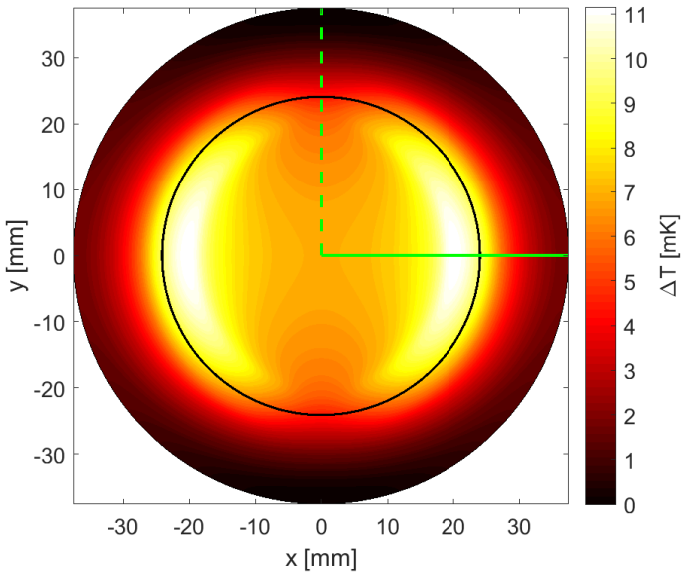

Figure 3.21: *Temperature distribution on the sample surface due to 50 mW of RF heating. A peak temperature of 3.66 K is observed in the high-field region. A black circle highlights the radial position of the temperature sensor on the sample bottom, green lines indicate cut lines for high-field and low-field region. See Fig. 3.22 for further details.*

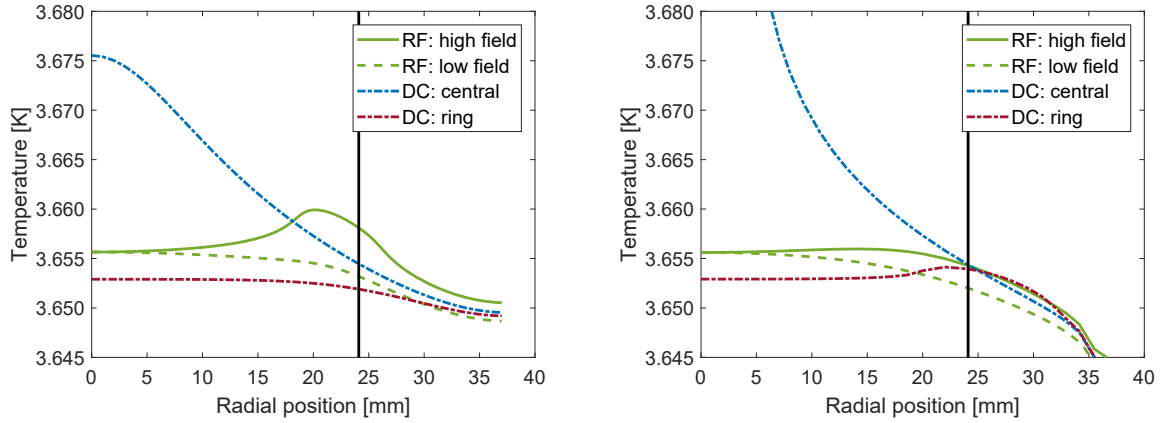

(a) *Temperature profiles on the RF surface.*

(b) *Temperature profiles on the sample bottom.*

Figure 3.22: *Exemplary simulation results for 50 mW of heater power applied to the different boundary heat sources individually. The radial position of the temperature sensor is indicated by a vertical black line. For the 2D temperature distribution due to RF heating see Fig. 3.21.*

The question remains, how vertical and horizontal gradients in temperature and RF field influence the calculated surface resistance. By definition (see Eq. 3.4) the measured surface average value is given by

$$\langle R_\mathrm{S} \rangle = \frac{\iint_\mathrm{sample} R_\mathrm{S}(T, H, \dots) |H|^2 \, \mathrm{d}S}{\iint_\mathrm{sample} |H|^2 \, \mathrm{d}S}. \tag{3.16}$$

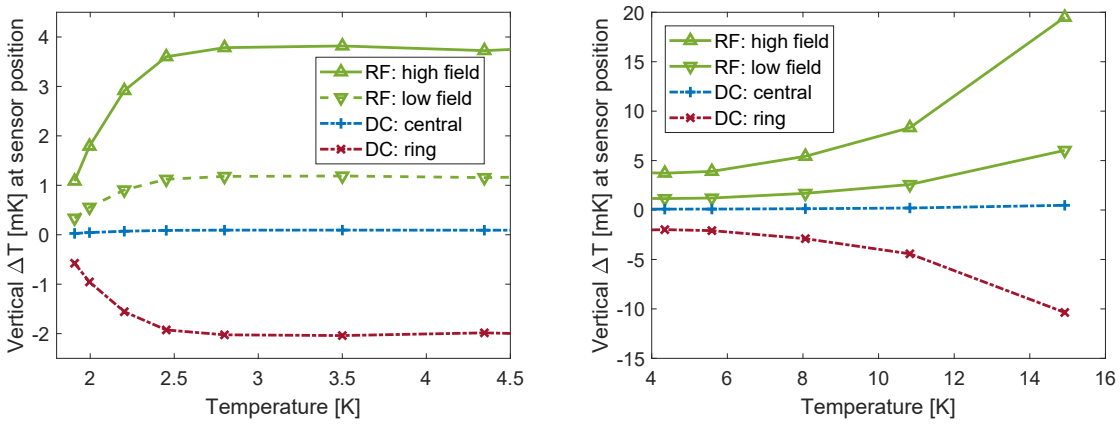

Figure 3.23: *Vertical temperature gradient $\Delta T = T_{top} - T_{sensor}$ at the location of the reference sensor. "low field" and "high field" denote the cases of mounting the sensor on the same radius but below the location of lowest resp. highest RF field.*

This average is now to be related to the temperature reading at the reference sensor position. Ideally, the measured average equals the surface resistance of the sample at the point which has the (measured) reference temperature. However, this depends on the actual temperature dependence of the surface resistance which is to be measured. In order to estimate this effect, a worst-case scenario of high BCS resistance is studied, represented by RRR 300 niobium with negligible residual resistance. Temperature distributions like the one given in Fig. 3.21 for different values of heater power and the corresponding $R_S(T)$ for Q1 and Q3 are used to calculate the surface average $\langle R_S \rangle$ and the "true" value at reference temperature. The results given in Fig. 3.24 show a systematic underestimation on the permille level.

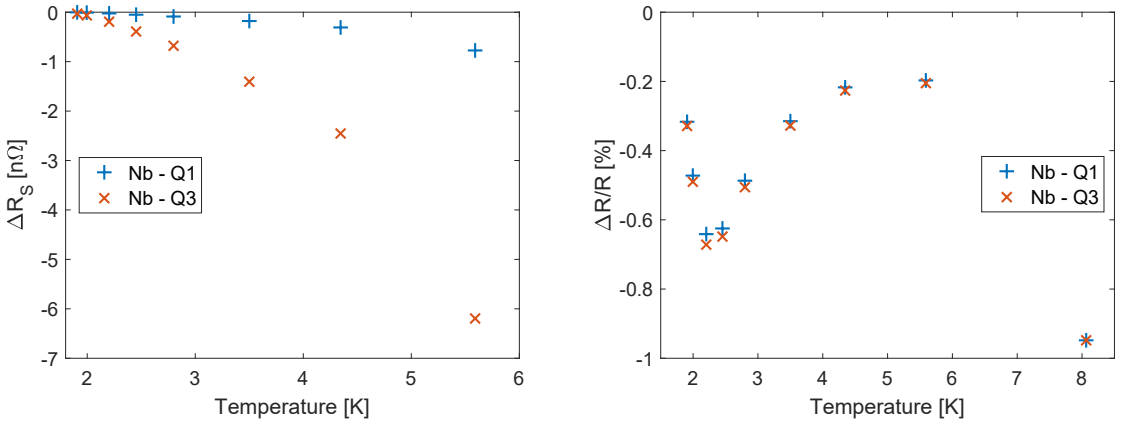

Figure 3.24: *Absolute and relative mismatch ($\Delta R_S = R_{S,meas} - R_{S,true}$) between measured average surface resistance and the true value at the point of reference temperature. $R_S(T)$ is calculated using SRIMP for RRR 300 niobium with zero residual resistance.*

Compared to other sources of uncertainty the effect of temperature gradients is rather low. However, it cannot be estimated from data without a simulation model. For the same reason localized heating, e.g. by defects or multipacting, can hardly be investigated in case of poorly performing samples. A potentially highly significant mismatch of measured values for R_S and B_{RF} arises from field-dependent surface resistance (Q-slope). The large gradient in RF field across the sample surface can lead to an underestimated Q-slope of more than 10 % at highest fields for the common assumption of $B_{RF} = B_{pk}$. Further, in the case of a nitrogen doped sample, where the surface resistance decreases with increasing B_{RF} over a certain range, the field level of minimum surface resistance is shifted systematically [80, 97].

Recently, a mathematical method was published that is capable of correcting systematic errors due to field-dependent surface resistance without knowing the actual non-linearity of the surface resistance a priori [98]. Based on the known RF field profile, a distribution function is computed that subsequently transforms an interpolation of the measurement data set using correction coefficients. In the Appendix Section A.4 those coefficients are calculated for the first three quadrupole modes and polynomial fits of up to fifth order. However, this method was not used in the later course of this thesis since the underlying assumption of a homogeneous sample surface is very likely violated, introducing again unknown systematic errors.

3.4 Upgrade II: Sample Chamber Assembly and Extended Diagnostic Capabilities

Besides its measurement capabilities the QPR provides the potential to have a sample geometry that is more compatible to surface preparation and thin film deposition techniques than the inner surface of an accelerating (single-cell) cavity. However, the sample chamber assembly containing a double-sided CF100 flange is still difficult to integrate into (wafer) coating devices and further diagnostic tools like optical or electron microscopes. For that reason, several designs of demountable sample chambers were studied and tested, the most successful one is presented here [81, 99, 100]. Fig. 3.25 shows a cut view of this design.

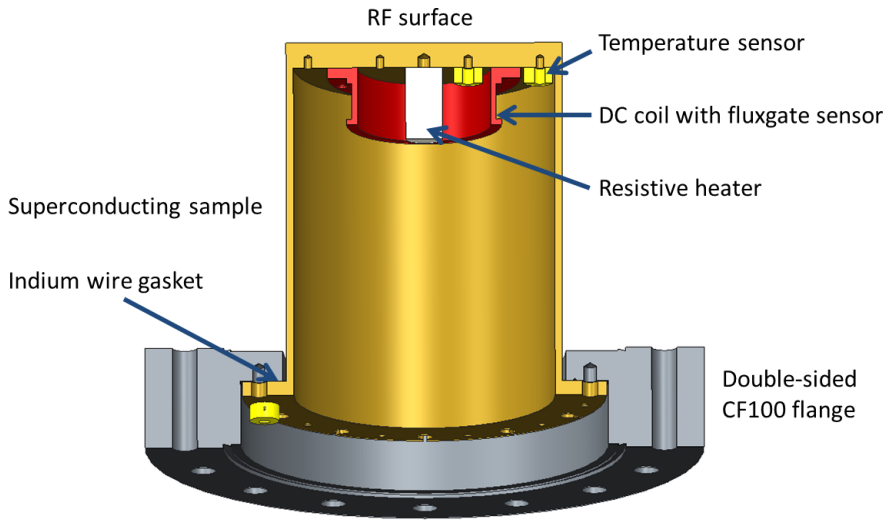

Figure 3.25: *Cut view of the demountable sample chamber, including heater and diagnostics. Not depicted are screws for chamber assembly and sensor mounting and the feedthrough flange closing the sample chamber at its bottom.*

The two main aspects are a detachable joint between sample part and CF flange and a disk-shaped sample. The outer surface of the sample chamber which is exposed to the RF field has no additional structures or features, hence preventing any impact on the RF field or parasitic losses. The top part is now one flat disk without a corrugated bottom surface as before (compare [15]). The impact of thermal gradients on the sample is negligible and well within the simulation uncertainty coming from the uncertainty in the assumed non-linear thermal conductivities of niobium and stainless steel. In case the sample piece is fully made of niobium, only one electron-beam (EB) weld near the RF sample is necessary, connecting top disk and tube part. Unlike in earlier designs, the weld at the sample surface and brazing steps are omitted. Furthermore, having one detachable part of high purity niobium enables contamination critical procedures, like heat treatments in an ultra-high vacuum (UHV) furnace, e.g. for diffusion coating with Nb_3Sn or for nitrogen doping/infusion.

The flat bottom surface of the sample provides more flexibility for usable diagnostics in terms of both, available threaded holes and achievable thermal contact. Also, the bottom part of the sample chamber piece can be used to host diagnostics like temperature sensors. In this way parasitic RF heating along the coaxial structure and at the CF flange can be monitored by comparing the temperature distributions for DC and RF heating. Together with the simulations discussed in Section 3.3.2 this also allows for a quantitative analysis.

The necessary UHV tight connection to the CF flange is implemented using an indium wire gasket. Experience showed reproducible performance which also resists thermal cycling to liquid helium temperature. It can be removed with low effort by scratching (e.g. with a copper tool), remnants on the niobium part are easily dissolved in nitric acid without solvating the underlying niobium. The resulting height offset due to the indium wire is about $(0.2 \pm 0.1)\,\mathrm{mm}$ which is acceptable for the gap calibration procedure. Repeated treatments or coatings of a sample will yield a reduced height since for each step chemical etching/polishing is needed to achieve a clean substrate again. Positive height adjustment of the sample chamber is possible by machining the flange. Mounting the sample to the flange "from below" provides the mechanical security measure that the RF gap to the quadrupole pole shoes cannot be too small in case of a thick indium gasket, hence touching is excluded. Unlike in earlier demountable designs, cleanroom handling of the gasket is improved significantly: Using a customized frame supporting the CF flange, mounting is done "upside down". Compared to the other existing QPR at CERN, the outer dimensions of the sample chambers have a height difference of 3.5 mm. By using different CF flanges this can easily be compensated, providing exchangeability among both systems.

The DC heater for active control of the sample temperature is custom made, and consists of a nichrome[2] wire wrapped around a copper rod. Nichrome is a non-magnetic alloy with high resistivity at cryogenic temperatures, thermal contact to the copper rod is enhanced by indium foil and epoxy glue. A twisted pair of wires is used to eliminate DC magnetic fields generated by the heater current. This is crucial, since systematic studies on trapped magnetic flux, thermocurrents, and cooldown dynamics require active heating during the superconducting transition.

For temperature measurements, calibrated Cernox® sensors are used (CX-1030-CU-1.4L, Lake Shore Cryotronics). Thanks to the clearance hole of the CU-package, sensors are attached with M2.5 screws made of titanium. Stress-free mechanical and thermal contact under cryogenic conditions is ensured due to the similar thermal contraction of niobium and titanium. The thermal contact of the sensors is further enhanced by applying a thin film of Apiezon N® grease. Including the electronic accuracy of the LS336 controller, an overall temperature accuracy of $\pm 5\,\mathrm{mK}$ is achieved for temperatures below 10 K, decreasing up to $\pm 9\,\mathrm{mK}$ at 20 K. The stability of the heater control loop is limited by the electronic precision of the LS336 controller to 0.1 mK, which coincides with the resolution limit of the temperature measurement.

[2] Composition: 80 % nickel, 20 % chromium

3.5 Measuring the RF Critical Field

Investigating the highest accelerating gradient achievable with a superconducting cavity, the intrinsic material limit is set by the critical magnetic (RF) field (see Section 2.2). Measuring at different temperatures gives access to both, the critical field extrapolated to 0 K as well as the critical temperature:

$$B_{\mathrm{c,RF}}(T) = B_{\mathrm{c,RF}}(0\,\mathrm{K}) \cdot \left(1 - \left(\frac{T}{T_{\mathrm{c}}}\right)^2\right) \tag{3.17}$$

Thanks to the thermal design of the QPR sample chamber, arbitrary and precisely stabilized temperatures above the liquid helium bath temperature are possible. This is especially relevant since, given by the quench limit of the QPR at about 120 mT, the sample has to be heated significantly in order to reduce its critical field.

The RF critical field is measured using single rectangular pulses of RF power. Software triggering of the RF signal generator enables non-periodic pulses of arbitrary separation, which in turn ensures stable sample temperature prior to each pulse. A quench suddenly decreases the quality factor of the resonator, leading to a drop of transmitted RF power. For power measurements, fast power meters (Keysight U2042XA) are used, providing a time resolution down to 50 ns. From the trace of such a pulse, the RF quench field can directly be taken from the peak value. Fig. 3.26 shows four exemplary pulse traces of transmitted RF power, converted to the peak RF field on the sample (Eq. 3.6). The LS336 device used to read out the temperature sensors, attached to the bottom surface of the sample, provides a maximum data rate of 10 samples per second. This is too slow to resolve the temporal evolution of the quench, but useful to distinguish between a quench of the sample or the resonator itself.

The requirement of a sudden decrease in transmitted power triggered by a quench puts limits on the loaded quality factor of the QPR and the measurement resolution. The unperturbed loaded quality factor Q_{L} has to be high enough, that it can be dominated by the partially normal conducting sample surface after a quench occurred. On the other hand, strong overcoupling and low values of Q_{L} are desired to minimize the quench time and RF heating (see Section 3.5.2). Assuming the initial situation of strong overcoupling ($Q_{\mathrm{L}} \approx Q_{\mathrm{input}}$) and a quenched sample quality factor of at most $Q_{\mathrm{s,q}} = Q_{\mathrm{input}}$, the minimum detectable quench size A_{q} can be estimated:

$$Q_{\mathrm{s,q}} = \frac{\omega U}{P_{\mathrm{sample}}} = \frac{2\omega U}{R_{\mathrm{S}} A_{\mathrm{q}} H_{\mathrm{pk}}^2} \tag{3.18}$$

$$A_{\mathrm{q}} = \frac{2\omega U}{Q_{\mathrm{input}} R_{\mathrm{S,nc}} H_{\mathrm{pk}}^2} = \frac{2\mu_0^2}{R_{\mathrm{S,nc}} \tau_{\mathrm{L}} c_2} \tag{3.19}$$

with $P_{\text{sample}} \approx \frac{1}{2} R_{\text{S,nc}} H_{\text{pk}}^2 A_{\text{q}}$ and $Q_{\text{input}} = \omega \tau_{\text{L}}$. $R_{\text{S,nc}}$ denotes the normal conducting surface resistance which can vary widely in the range of 0.6 mΩ for high-purity niobium in the anomalous limit (see Eq. 3.12 with $\rho\ell = 6 \cdot 10^{-16}\,\Omega\text{m}^2$ [41]) up to about 24 mΩ for NbTiN ($\rho_{\text{n}} = 35\,\mu\Omega\,\text{cm}$ [16]). This corresponds to quench sizes of $A_{\text{q}} = 0.7 - 29\,\text{mm}^2$ and $\tau_{\text{L}} = 1.8\,\text{ms}$ for Q1. In other words, a material-independent resolution criterion can be defined

$$\frac{2\mu_0^2}{\tau_{\text{L}} c_2} = A_{\text{q}} \cdot R_{\text{S,nc}} = 17.5\,\text{m}\Omega\,\text{mm}^2 \tag{3.20}$$

with the RF calibration constant $c_2 = \frac{B_{\text{pk}}^2}{U}$ (Eq. 3.7) relating peak RF field to stored energy.

Investigating the pulse traces shown in Fig. 3.26, the actually quenched sample area can be estimated. The quench does not only decrease Q_{L}, but also shifts the resonant frequency by several kHz which is much larger than the cavity bandwidth of 80 to 100 Hz. If one assumes that the PLL loses lock for about 1 ms, the QPR can be regarded as undriven and the decrease of stored energy is described by an exponential decay with time constant $\tau_{\text{quench}} < \tau_{\text{L}}$. Since in practice $Q_{\text{s,q}} < Q_{\text{input}}$, τ_{quench} is dominated by the quenched sample area which can be derived using Eq. 3.19. If the assumption that the PLL loses lock is not valid, the decay is slowed down, leading to an underestimated quench area. This effect is visible in the pulse traces shown in Fig. 3.26 for $T > 17\,\text{K}$: Due to the increasing penetration depth close to T_{c} (see Section 3.6), the jump in resonant frequency decreases. Eventually, the PLL keeps lock and the peak in transmitted power is less distinct. In this case, fits to the post-quench behavior are meaningless to deduce the quenched sample area. A detailed quantitative analysis of the RF quench field including the quenched sample area is given for the Nb_3Sn sample, see Section 4.4.

3.5.1 Uncertainty of RF Field Strength and Sample Temperature

The RF quench field is deduced from pulse traces, recorded by fast USB power meters, and converted to RF magnetic on sample using Eq. 3.6. As discussed earlier, the relative uncertainty of RF measurements is estimated with $\frac{\sigma_{\text{RF}}}{\text{RF}} = 9.2\,\%$ (see Section 3.3.2 and esp. Eq. 3.14). This applies for both P_{t} and Q_{t} yielding

$$\left(\frac{\sigma_{\text{B}}}{B}\right)^2 = \left(\frac{\sigma_{Q_{\text{t}}}}{2Q_{\text{t}}}\right)^2 + \left(\frac{\sigma_{P_{\text{t}}}}{2P_{\text{t}}}\right)^2 = \frac{1}{2}\left(\frac{\sigma_{\text{RF}}}{\text{RF}}\right)^2 \tag{3.21}$$

and hence

$$\frac{\sigma_{\text{B}}}{B} = \frac{1}{\sqrt{2}} \cdot 9.2\,\% = 6.5\,\%. \tag{3.22}$$

For sample temperatures up to 20 K the PID controlled heater provides temperature stability better than 1 mK. Pressure fluctuations of the liquid helium bath are actively compensated and hence negligible for this measurement. The temperature accuracy is set by the calibration

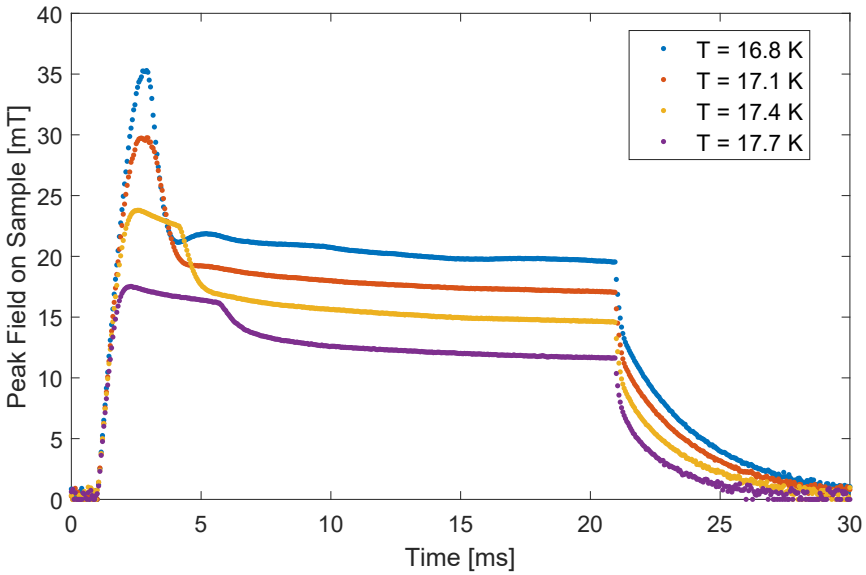

Figure 3.26: *RF field on the sample surface measured at the pickup probe at four different temperatures for the Nb_3Sn sample discussed in Section 4. A constant pulse length of 20 ms was used. The RF quench field is given by the peak value. The post-quench behavior changes with temperature since it depends on temperature dependent thermal properties of the sample and on RF characteristics like Lorentz-force detuning and the loaded quality factor of the QPR.*

accuracy of the respective temperature sensors. In terms of Cernox® sensors, this is ±5 mK for temperatures below 10 K, increasing up to ±9 mK at 20 K (see Section 3.4). Additional systematic uncertainty comes from temperature gradients across the sample. As discussed in Section 3.3.3, the reference temperature sensor is placed at the sample bottom, right below the region of highest RF field. Assuming a homogeneous, defect-free superconductor, this is the area where an RF-triggered quench occurs. Given by the vertical temperature distribution due to the central DC heater, the sample temperature is slightly underestimated. As shown in Fig. 3.23 for the case of bulk niobium, this effect is less than 0.5 mK for sample temperatures below 15 K and hence negligible. In case of defects on the superconducting sample surface, lateral temperature differences become relevant. The simulated horizontal temperature difference on the RF surface for bulk niobium is shown in Fig. 3.27. A maximum value of $\Delta T = 180$ mK is observed close to T_c. Note that this discussion only applies to the situation *before* the RF pulse. More important are temperature dynamics *during* the RF rise time which are studied in the next section.

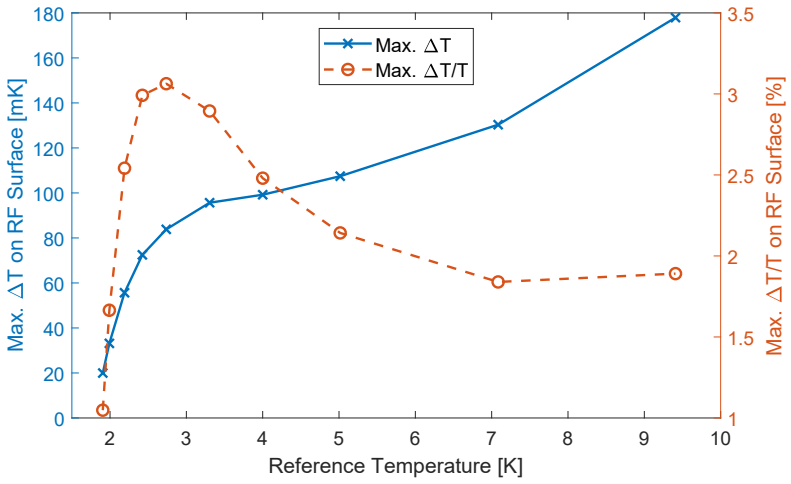

Figure 3.27: *Maximum absolute (solid line) and relative (dashed line) horizontal temperature differences on the RF surface. The curves are simulated for a bulk niobium sample with central DC heater.*

3.5.2 Systematic Error due to RF Heating

The intrinsic source of systematic error for the $B_{\mathrm{c,RF}}$ measurement technique presented above originates from RF heating during the RF rise time. Due to the intrinsic quench limit of 120 mT of the QPR itself, the sample must be heated significantly for its critical field to be below this value. Consequently, by approaching T_{c} the critical field becomes increasingly temperature dependent, hence the RF rise time has to be short enough to limit RF heating to an acceptable level. Significant heating will cause the observed critical field to be underestimated systematically due to an underestimated sample temperature. Reducing the RF time constant $\tau_{\mathrm{L}} = Q_{\mathrm{L}}/\omega$ increases the required RF drive power. In the limit of strong overcoupling, the required forward power is given by $P_{\mathrm{f}} = \frac{U}{4\tau_{\mathrm{L}}}$ [8]. The QPR is normally operated with an overcoupled input antenna (see Section 3.2.1) with the RF calibration constant $c_2 = \frac{B_{\mathrm{pk}}^2}{U}$ (Eq. 3.7) relating peak RF field to stored energy. Common values are $c_2 = 0.1 \ldots 0.15\,\frac{\mathrm{T}^2}{\mathrm{J}}$. Compared to a 1.3 GHz TESLA-shaped single-cell cavity with $\frac{B_{\mathrm{pk}}^2}{U} = 0.0013\,\frac{\mathrm{T}^2}{\mathrm{J}}$ [40] and assuming equal rise time and magnetic field, the required forward power is reduced by about two orders of magnitude.

In cavity measurements, pre-quench RF heating was identified to be a major issue, even when using a MW rated klystron and achieving quench times well below 1 ms [66, 101, 102]. Quench times of 50 to 200 µs led to errors due to heating of about 40 % [66]. For the QPR, the dependence of the observed quench field on the RF rise time, and hence the amplifier forward power, was studied in a dedicated measurement. Since the term "rise time" is a characteristic quantity of the pulse shape that does necessarily tell how long the RF power is actually rising, instead the expression "quench time" (t_{quench}) is used in the following. It measures the duration from switching on the RF power until a quench occurs. The forward power rise time can be

neglected since it is less than 15 ns. Fig. 3.28a shows the measured quench time as a function of forward power. A nitrogen-doped bulk niobium sample was used for this test, all points were taken at a sample temperature of 8.6 K and at the first quadrupole mode (Q1, 412 MHz). With increasing RF power the quench time drops, hence reducing the possible amount of unwanted heating. More important, Fig. 3.28b shows the impact of thermal issues on the obtained quench fields. Assuming a linear trend for $t_{\mathrm{quench}} \to 0$, the systematic underestimation of $B_{\mathrm{crit,RF}}$ at $t_{\mathrm{quench}} = 2.5\,\mathrm{ms}$ amounts to about 1 mT or 3 %. This is well within the RF measurement uncertainty of about 6.5 % (see Section 3.3.2). Furthermore, the amount of RF heating on the sample surface can be estimated: Extrapolating the value of $B_{\mathrm{c,RF}}(8.6\,\mathrm{K}, t_{\mathrm{q}} = 0) = 35.8\,\mathrm{mT}$ to 0 K using Eq. 3.17 yields $B_{\mathrm{sh}} \approx 264\,\mathrm{mT}$ (T_{c} =9.25 K). Reducing the critical field at 8.6 K by 1 mT corresponds to a temperature rise of $\Delta T = 20\,\mathrm{mK}$.

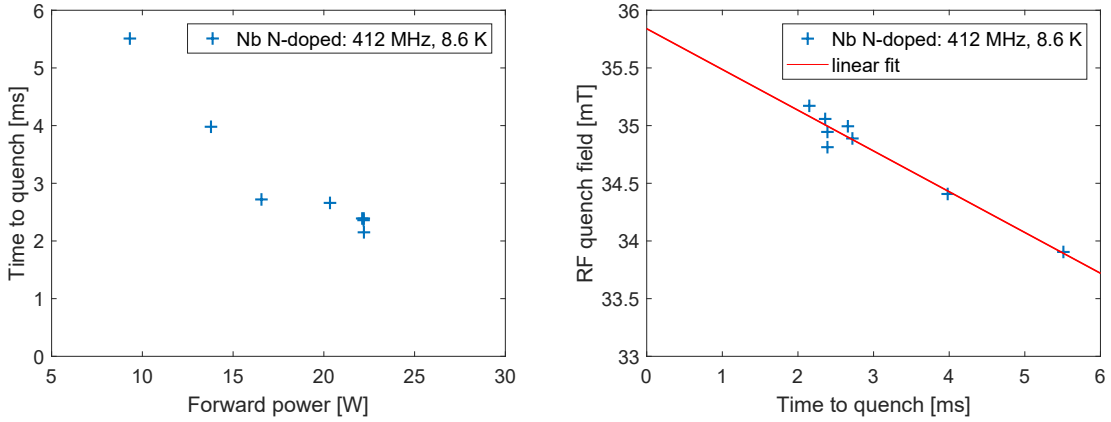

Figure 3.28: *Duration of rising RF field until a quench occurs as a function of forward power (left) and corresponding RF quench field (right). Data was measured on a nitrogen-doped bulk niobium sample at 8.6 K and Q1 (412 MHz).*

From the numerical comparison of RF field per stored energy for the QPR and a TESLA-shaped single-cell cavity as presented above, the RF forward power requirement for critical field measurements using the QPR seems low compared to the MW rated klystron as needed for single-cell cavities (see Fig. 3.28). Especially since quench times of few ms are acceptable for QPR measurements while severe thermal issues were observed on single-cell cavities at quench times well below 1 ms [66]. The systematic differences of those two measurement setups become clear when investigating the temperature dynamics of the RF sample. In order to do so, time-resolved simulations using COMSOL are computed. The simulation geometry introduced before (see Section 3.3.2) is simplified such, that only the niobium part of the sample chamber is taken into account without any further parts. Especially no connection to the liquid helium bath, i.e. no cooling, is implemented. The temperature at the bottom end of the niobium sample chamber responds with a time delay of about 0.5 ms. Since the thermal diffusivity of stainless steel is 6 orders of magnitude lower than the one of niobium, there is no significant impact of the stainless steel (or the liquid helium bath) on the time scale investigated in the following.

The temperature dependent heat capacity of niobium is taken from [103]. For technical details on the simulation see Appendix Section A.8.

The scenario modeled with COMSOL is similar to the measurement data shown in Fig. 3.28. Starting at the initial temperature of 8.6 K, a heat pulse with 2.8 W peak power and spatial distribution of this power across the sample surface that reflects the squared magnetic field of an RF pulse is used. This corresponds to $B_{\mathrm{pk,RF}} = 35\,\mathrm{mT}$ and $R_{\mathrm{S}} = 9000\,\mathrm{n\Omega}$ being the BCS surface resistance of RRR 300 niobium at 8.6 K [43]. The dissipated power is modeled to increase linearly with time until a quench occurs at the time t_{quench}, which is a simple and conservative assumption. Fig. 3.29 shows exemplary temperature dynamics for a short pulse of $t_{\mathrm{quench}} = 50\,\mu\mathrm{s}$ and various values of sample thickness. The RF sample is modeled as solid disk connected to the niobium tube of the sample chamber, a thickness values of 7 mm matches the design discussed in Section 3.4. Measurement data shown in Fig. 3.28 was taken on an "old" sample with corrugated sample bottom, in this case the simulation geometry implies a simplification.

In Fig. 3.30 the significant impact of the sample thickness on the maximum temperature rise is obvious. Compared to the estimated heating of 20 mK from the measurement data of Fig. 3.28, the simulated heating is rather high, which might be due to both, a mismatch of thermal properties and the conservative assumption of dissipation rising linearly with time.

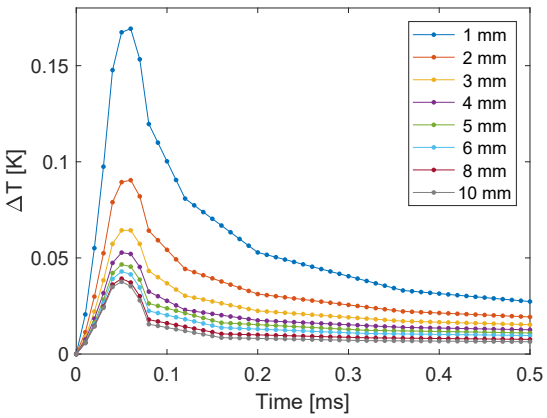

Figure 3.29: *Temperature dynamics of the sample surface at the location of highest magnetic field and various values of sample thickness. The RF heating rises linearly up to 2.9 W at 50 µs, corresponding to a quench of bulk niobium at 8.6 K ($R_S = 9000\,n\Omega$ and $B_{c,RF} = 35\,mT$).*

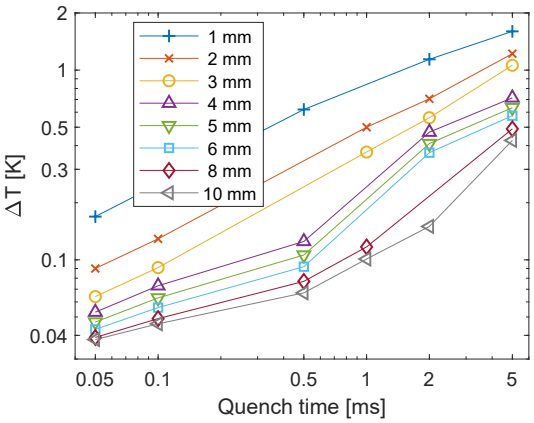

Figure 3.30: *Peak sample temperature rise vs. quench time and sample thickness. The peak dissipated power at t_{quench} is equal for all points, i.e. the slope of the rising field decreases towards higher values of quench time. Markers show calculated data points, missing points due to computational issues.*

Note that the situation of low sample thickness (2 or 3 mm) allows for an estimate of RF heating in cavity tests: Measuring at $T > 4.2\,\mathrm{K}$, single-cell cavities have to be operated in gaseous helium featuring very limited cooling. Comparing the cases of 2 mm and 10 mm, a thicker sample as in case of the QPR allows for quench times being larger by a factor 5 to 10 at the same level of peak temperature rise. In turn, the required RF forward power is reduced further as compared to a TESLA-shaped single-cell cavity.

Allowing for a systematically shifted temperature axis, Fig. 3.31 shows the impact on the observed critical field. It is further assumed that only the range $B < 0.5 B_{\mathrm{c},0}$ is experimentally accessible, as indicated by solid lines. In the inaccessible part at low temperature, dashed lines show the extrapolation from a fit to the obtained data points using Eq. 3.17. Shifting the temperature axis at low values results in an approximately equal relative error on $B_{\mathrm{c},0}$ while an error near T_c only affects this value. Note that any of those errors lead to lower values. In order to obtain a value of $B_{\mathrm{c},0}$ that is overestimated, a non-linear temperature shift that is increasing with sample temperature would be required.

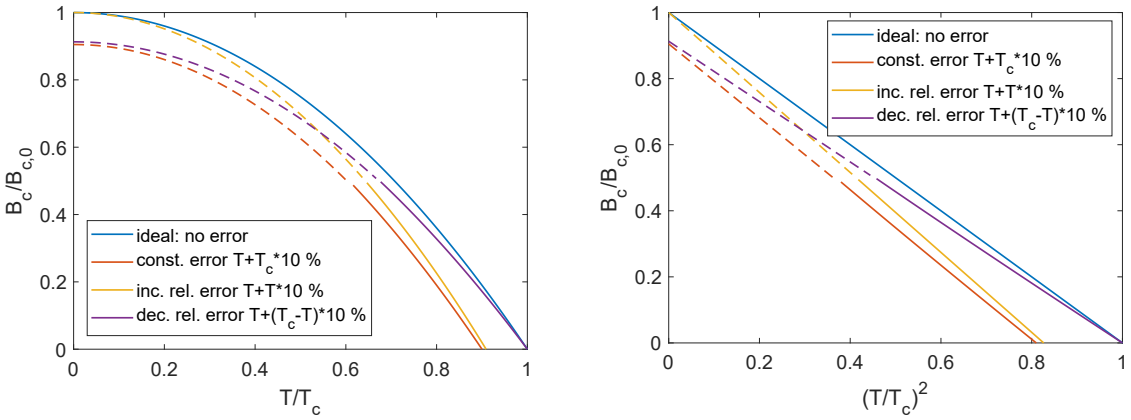

Figure 3.31: *Impact of a systematically shifted temperature axis on the observed critical field. Besides a constant offset two types of temperature dependence such as linearly increasing and linearly decreasing shift are studied. It is assumed that only the range $B < 0.5\,B_{\mathrm{c},0}$ is experimentally accessible, indicated by the solid line section of the shifted curves. The dashed section gives the extrapolation from a fit to the accessible range.*

3.5.3 Operational Experience II: Dynamic Detuning and Minimum Quench Time

The transmitted power is used to measure the instantaneously stored energy inside the resonator $U(t) = \frac{P_\mathrm{t}(t)Q_\mathrm{t}}{\omega}$. When driving a resonator with rectangular pulses of forward power, the time dependence $P_\mathrm{t}(t)$ is given by [8]

$$P_\mathrm{t}(t) = P_0 \left[1 - \exp\left(-\frac{t}{2\tau_\mathrm{L}}\right)\right]^2 \qquad \text{(switch on)} \tag{3.23}$$

$$P_\mathrm{t}(t) = P_0 \exp\left(-\frac{t}{\tau_\mathrm{L}}\right) \qquad \text{(switch off)} \tag{3.24}$$

with P_0 denoting the steady-state power level. The characteristic time constant $\tau_\mathrm{L} = Q_\mathrm{L}/\omega$ is determined by the loaded quality factor Q_L. Trying to reduce t_quench, i.e. the time that is required to reach a certain magnetic field on the sample surface, leads to minimizing the expression

$$t_\mathrm{quench}(\tau_\mathrm{L}) = -2\tau_\mathrm{L} \ln\left(1 - \sqrt{\frac{B^2_\mathrm{sample}}{4c_2\tau_\mathrm{L}P_\mathrm{forward}}}\right) \tag{3.25}$$

in the limit of strong overcoupling $U = 4\tau_\mathrm{L}P_\mathrm{forward}$. Since $Q_\mathrm{L} \approx Q_\mathrm{in}$, the input coupler is used to adjust τ_L. Fig. 3.32 shows t_quench as a function of Q_L for different values of B_sample. Operational experience showed deviations from the expected quench time towards increasing RF field. In Fig. 3.33 typical pulse traces of transmitted power are shown in case of high and low field with

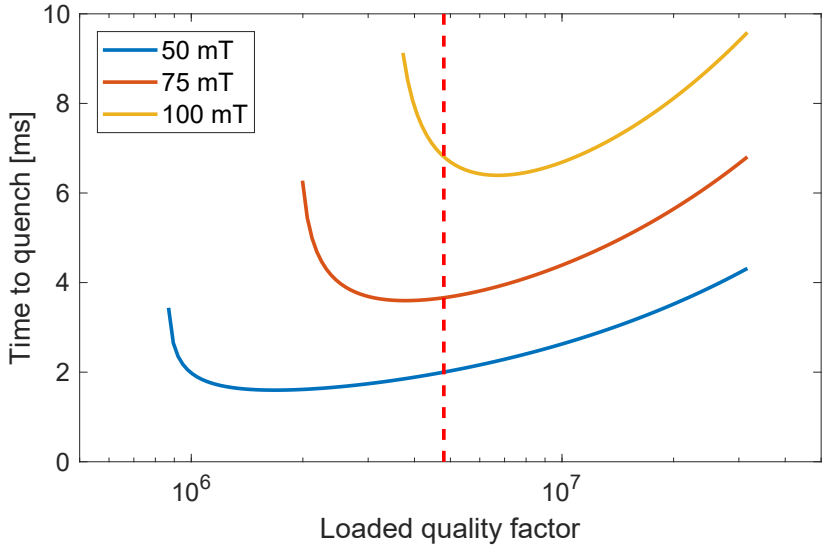

Figure 3.32: *Minimum achievable quench time as a function of loaded quality factor ($P_{forward} = 20\,W$, $f = 420\,MHz$). Q_L of the measurement shown in Fig. 3.28 is indicated with a dashed vertical line.*

fits according to Eqs. 3.23 and 3.24. In the case of high power a quench is observed. After switching off the RF power source, the decay of stored energy inside the resonator is given by τ_L which is comparable for both pulse traces as expected. Note that in case of a quenched sample, the transition back to the superconducting state happens on a much faster timescale. For the rising edge, only at low power a time constant is observed that is consistent with the falling edge. At high power, the quench occurs at $P_{\mathrm{t,pk}} \ll P_0$ which yields an ill-defined fit, especially when further restricting the data range to low power. For that reason, only a lower limit on τ can be derived with confidence. The value of $\tau_{2,\ \mathrm{rise}} > 5\,\mathrm{ms}$ indicates an effect that significantly delays the RF field build-up inside the resonator.

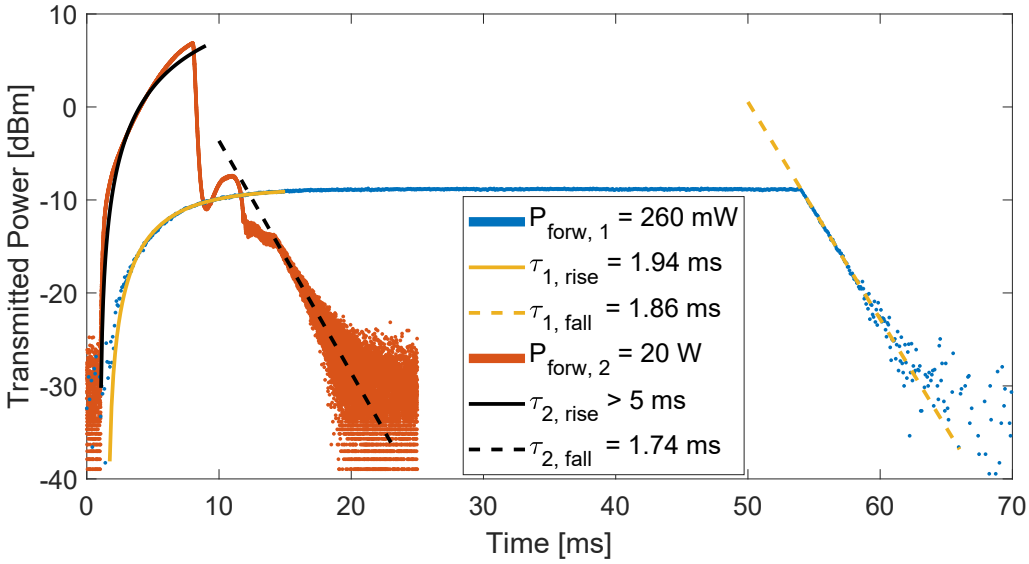

Figure 3.33: *Typical pulse traces of transmitted power for low and high RF field (with quench). Fits to rising and falling edge yield the characteristic time constant τ. RF build-up at high power is delayed significantly.*

Such behavior can be explained by dynamic detuning of the QPR with an amplitude that can not be instantaneously compensated by the PLL system. One possibility is given by microphonics: The most important vibrational frequencies near 100 Hz correspond to periods of about 10 ms. Since a quarter period is close to typical quench times, maximum detuning can occur on the relevant time scale. Detuning amplitudes of several kHz have been observed [85]. However, microphonics should affect the pulses at high and low RF power similarly. Field-dependent dynamics are caused by Lorentz Force (LF) detuning. Measurements during commissioning of the QPR gave a detuning constant $\mathrm{d}f/\mathrm{d}B = -0.96\,\mathrm{Hz/mT^2}$ [80], which again is much larger than for TESLA-type elliptical cavities ($-0.053\,\mathrm{Hz/mT^2}$ [40]). At high fields of $B_\mathrm{pk} = 100\,\mathrm{mT}$, Lorentz forces account for a peak detuning of $\Delta f = -9.6\,\mathrm{kHz}$. This value is large compared to the QPR bandwidth of 80 Hz to 100 Hz, hence, during the RF rise time, the PLL might not be able to follow the changing resonant frequency instantaneously, yielding the observed delay

in RF field build-up. Active feed-forward compensation acting on the signal generator could improve this behavior in the future. Operation with continuously pulsed RF at Q3 showed another effect caused by dynamic LF detuning: Using a spectrum analyzer on the transmitted power, the excitation of sideband frequencies was observed. This behavior vanished in CW mode which, again, indicates a dynamic effect. Since the Lorentz force is strong in the high-field region at the bottom end of the quadrupole rods, mechanical oscillations – microphonics – can be triggered. Due to the small mode separation at Q3, this coupled instability can lead to simultaneous excitation of a neighboring dipole mode. In case mechanical oscillations or deformations are present that break the quadrupole symmetry of the resonator, the exponential damping of fields propagating into the coaxial structure of the sample chamber is weakened. This leads to significantly increased RF losses on the bottom stainless steel flange that might explain the high values of surface resistance observed at Q3 for some samples [83].

3.6 Measuring RF Penetration Depth

Heating up a superconductor close to its critical temperature leads to an increasing penetration depth (see Eq. 2.3). In case of an SRF cavity, this is equivalent to an increasing magnetic volume of the cavity. By using Slater's theorem [104, 105] the change in resonant frequency is derived:

$$\frac{\Delta f}{f} = \frac{\frac{1}{4}\int_V^{V+\Delta V}\left(\epsilon_0|\boldsymbol{E}|^2 - \mu_0|\boldsymbol{H}|^2\right)\mathrm{d}V}{U} \tag{3.26}$$

The electric penetration depth for perpendicular fields is negligibly small [106], leading to $\Delta f < 0$. In case of the QPR, the sample can be heated separately, leading to a shift of resonant frequency only due to the penetration depth of the RF sample surface. In analogy to the geometry factor of RF cavity, a geometry factor of the sample G_{sample} is defined

$$G_{\mathrm{sample}} = \frac{\omega\mu_0\int_V|\boldsymbol{H}|^2\,\mathrm{d}V}{\int_{\mathrm{sample}}|\boldsymbol{H}|^2\,\mathrm{d}S} = \frac{\langle R_{\mathrm{S}}\rangle\,\omega U}{P_{\mathrm{sample}}} = Q_{\mathrm{sample}}\,\langle R_{\mathrm{S}}\rangle \tag{3.27}$$

that considers losses occurring on the sample surface only. Splitting the volume integral of Eq. 3.26 into surface and depth parts yields

$$\frac{\Delta f}{f} = -\frac{\pi\mu_0 f}{G_{\mathrm{sample}}}\Delta\lambda \tag{3.28}$$

$$\Delta\lambda = \lambda(T) - \lambda_0 = -\frac{G_{\mathrm{sample}}}{\pi\mu_0 f_0^2}\Delta f \tag{3.29}$$

with λ_0 and f_0 representing the approximately temperature independent values at low temperature. An alternative derivation of the same formula using a different perturbation method can be found in [107, 108]. Given by the temperature dependence $\lambda(T) \propto 1/\sqrt{1-(T/T_{\mathrm{c}})^4}$ (see Eq. 2.3), temperatures close to T_{c} are needed to measure a significant $\Delta\lambda$.

For the QPR, the expected maximum frequency shift of $|\Delta f| \approx 1\ldots20\,\mathrm{kHz}$ is disturbed by microphonics and changes in environmental pressure. Assuming a measurement time of 2 hours and a typical heat load of few Watts, yields a drift of center frequency by $\Delta f \approx -2\,\mathrm{kHz}$ due to the decreasing liquid helium level (see Section 3.2.3). This is superimposed by "fast" frequency fluctuations of about $\pm50\,\mathrm{Hz}$ on the timescale of 1 minute, coming from pressure fluctuations of the cryogenic system (see Section 3.3.2). Studies of the microphonic detuning gave an amplitude of several hundred Hertz, dominated by mechanical eigenmodes of the quadrupole rods with frequencies near 100 Hz [14, 80, 85]. In the following section, two different methods of measuring f vs. T for determining the penetration depth are discussed.

3.6.1 PLL-based Method

The frequency counter being part of the PLL system (Agilent 53181A) is used to monitor the resonant frequency when operating with CW RF, stabilized by the PLL (Section 3.2.2). This counter provides high-resolution measurements, the data rate of about 1 sample per second is limited by the computer readout system. On that timescale, microphonics are naturally suppressed by averaging. The heater controller can be operated in a ramp mode, with ramping speed down to 0.1 K/min. Assuming that this slow variation leads to a thermal quasi-equilibrium enables an automatized measurement of the penetration depth. Fig. 3.34 shows such a measurement of frequency vs. temperature with sample temperature ramped up and down again for the Nb_3Sn sample discussed in Chapter 4. At low RF field ($B < 0.5\,\mathrm{mT}$) the PLL is able to lock the resonance at temperatures up to few tens of mK below T_c. Approaching T_c, the surface resistance of the sample increases such, that the loaded quality factor – and hence the transmitted power – decreases substantially. Eventually, the pickup signal level is too low, causing the PLL to lose lock. The resulting temperature-independent frequency measurement seems to indicate the normal conducting state of the sample, but in fact is equal to the center frequency of the signal generator without any physical meaning. During post-processing, this range has to be excluded from the fitting procedure.

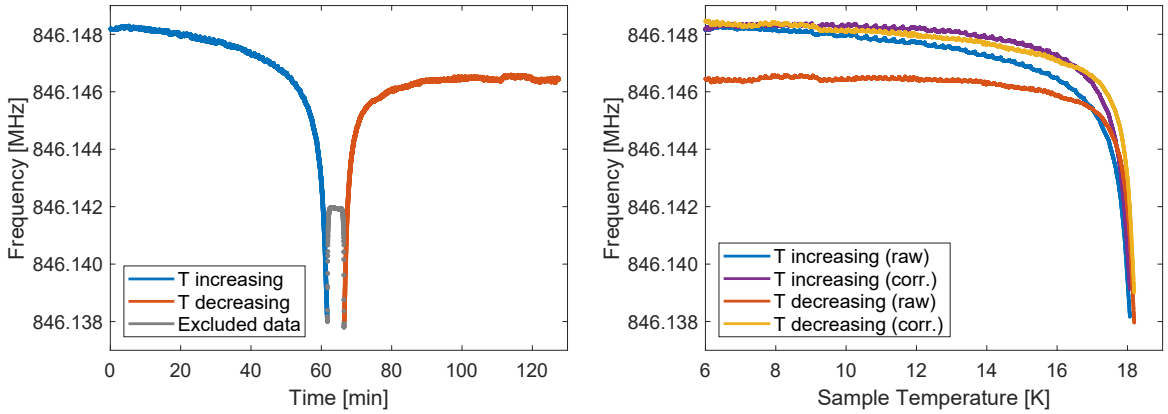

Figure 3.34: *PLL-based penetration depth measurement. "Corrected" data in the left plot shows the result after compensating changes in the helium level.*

Uncertainties due to statistics or measurement devices are negligible for this measurement technique. Both, relative and absolute accuracy of temperature and frequency measurements are very high, having no significant impact on the result. However, the calculated values for $\Delta\lambda$ and post-processing fits yielding λ_0 have severe accuracy issues due to systematic uncertainties: The helium level drift can be measured with long-time frequency monitoring (see Section 3.2.3). After compensating this effect, which is most visible at long times and low temperatures in Fig. 3.34, (virtual) hysteretic behavior is observed at temperatures close to T_c. This might have two reasons: a) An effectively true hysteretic behavior can arise from the temperature

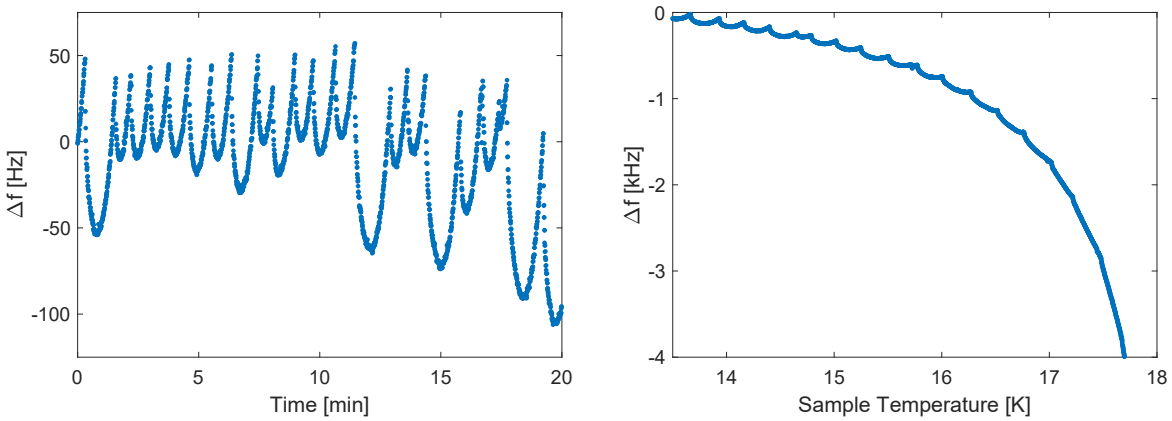

Figure 3.35: *Periodic frequency fluctuations due to active helium pressure control.*

profile on the sample surface. The scenarios of increasing or decreasing sample temperature have different temperature gradients on the RF surface. In the temperature range close to T_c, the derivative – and hence the sensitivity – $\mathrm{d}f/\mathrm{d}T$ is large. Here, deviations on the mK scale violate the assumption of a quasi-equilibrium state. b) Virtual hysteretic behavior is caused by slow oscillations of the resonant frequency due to pressure fluctuations in the cryogenic system (see Fig. 3.35). In the region of large $\mathrm{d}f/\mathrm{d}T$, the smallest possible ramp setting of 0.1 K/min may not provide sufficient sampling points to average this effect.

The systematic errors can be suppressed by stepwise changes of the sample temperature and long averaging times. Consequently, the high time resolution provided by CW measurements is not required, enabling the VNA-based method as discussed in the following section.

3.6.2 VNA-based Method

Alternatively to the PLL-based method discussed before, the resonant frequency of the QPR can be measured using a vector network analyzer (VNA, Agilent E8358A). In this case, the PLL system is bypassed such, that two ports of a VNA are directly connected to the antennas of the QPR. The resonant frequency is (ideally) given by the maximum value of the transmission scattering parameter S_{21}. A measurement using the reflection parameter S_{11} is more complicated, since both couplings are far off from critical. Fig. 3.36 shows two exemplary resonance scans. Given by the low output power of the VNA, RF heating is negligible.

Due to the strong microphonic detuning of the QPR, the resonance peak is distorted and oscillations in S_{21} are visible, corresponding to the periodic shift of resonant frequency. Assuming a symmetric distortion, the center frequency f_0 is obtained by fitting the dataset according to

$$S_{21}(f) = \frac{S_0}{1 + Q_L^2 \left(\frac{f - f_0}{f_0}\right)^2} \tag{3.30}$$

with peak value S_0 and loaded quality factor Q_L. Since the impact of microphonics is strongest near f_0, a windowed fit is applied cutting away the central region. This is done with a two-step fitting procedure as shown in Fig. 3.37. First, a rough estimate of f_0 is obtained using a horizontal data window. Subsequently, the central region $f_0 \pm 1\,\mathrm{kHz}$ is cut away and a second fit initialized by the previous results is computed. The outer limits of this vertically windowed fits are chosen consistently with the lower horizontal limit of step 1. The fit uncertainty amounts to $\sigma_f \approx 50\,\mathrm{Hz}$. Note, that the obtained fits depict a temporal average over many oscillation periods, leading to a broadened resonance curve and hence a value of Q_L that is systematically underestimated.

The impact of slow but periodic pressure fluctuations in the cryogenic system is suppressed by repeated VNA scans at stabilized sample temperature and averaging of fit results. For that, several minutes of measurement time per temperature point are required. Recording VNA scans at all three quadrupole modes yields a multi-frequency penetration depth measurement for one single thermal cycle. This method was used for the multilayer sample discussed in Chapter 5.

In summary, both methods discussed here – PLL-based and VNA-based – can be used to measure the penetration depth of a sample. The initial issue of temperature gradients causing hysteretic behavior can be solved in both cases using stepwise changes in temperature. In view of automatized measurement processes, the VNA-based method is preferred since the setup is easier to control and, compared to the more complex PLL-system, less sensitive to adjustment errors.

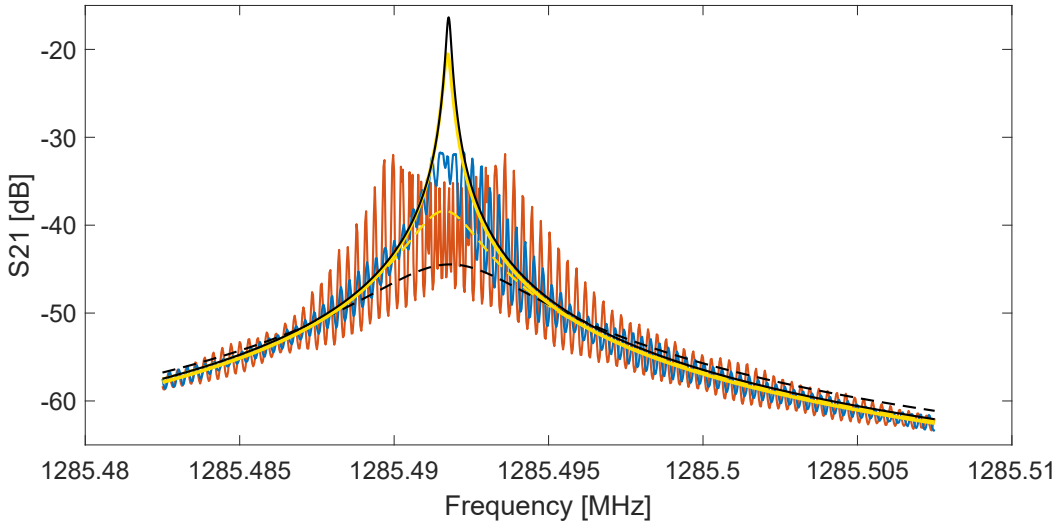

Figure 3.36: *Two VNA scans of Q3 (blue and red) measured in transmission. For each scan two fits are shown with different windowed data ranges based on cuts of a) S21 (dashed lines) or b) frequency axis (solid lines). Measurement data points are connected by solid lines to visualize microphonic detuning. For details on the fitting procedure see Fig. 3.37.*

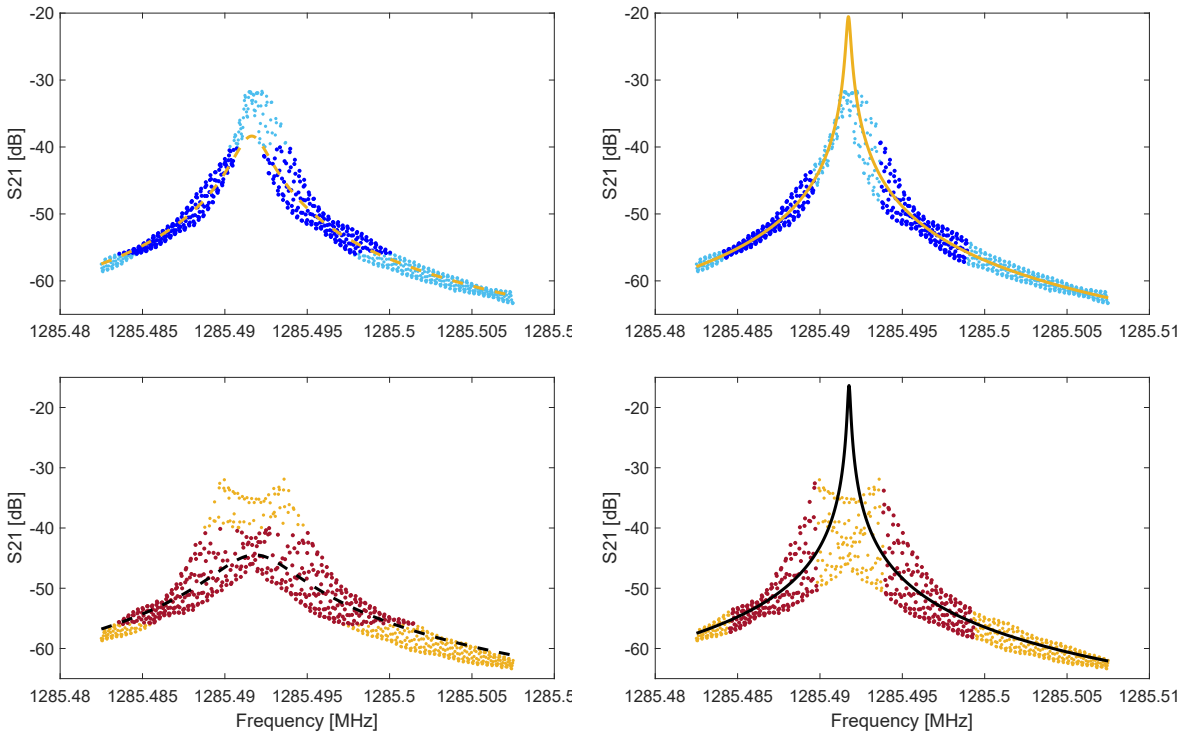

(a) *Horizontal data window.* ***(b)*** *Vertical data window.*

Figure 3.37: *Two-step fitting procedure for the VNA-based penetration depth measurement: Horizontally windowed fits (a) are used to define the vertical window* $f_0 \pm 1\,\mathrm{kHz}$ *and initial parameters for fits (b). In each plot the fitted data range is highlighted by darker colored points.*

4 RF Characterization of a Nb_3Sn Sample

Nb_3Sn is one of the most promising alternative materials to niobium for SRF cavities. Its critical temperature of about 18 K [109] is nearly twice that of Nb which allows, for example, to operate SRF cavities at 4.2 K at the same level of BCS losses as for Nb at 2 K. In that case, cavities can be operated in a liquid helium bath at atmospheric pressure with considerably simplifies the required cryo plant, reducing both operating and investment costs significantly. Close to stoichiometry, the superheating field of $\mu_0 H_{\mathrm{sh}} \approx 430\,\mathrm{mT}$ [3], compared to about 240 mT for Nb, potentially allows to operate TESLA-shaped $\beta = 1$ elliptical cavities at accelerating gradients up to $E_{\mathrm{acc}} \approx 100\,\mathrm{MV/m}$ [40]. Due to the low value of $\mu_0 H_{\mathrm{c1}} \approx 38\,\mathrm{mT}$, Nb_3Sn has to be operated in a metastable vortex free state. The question that therefore arises is how high in field the metastable state can be maintained.

Cryogenic tests of cavities revealed: (1) reproducible high Q_0 values on the order of 10^{10} at 4.2 K, corresponding to R_{S} values of about 27 nΩ which is beyond the fundamental limits of niobium. (2) reproducible sustaining of this high Q_0 to useful accelerating gradients above 16 MV/m corresponding to peak magnetic B_{pk} values in excess of 70 mT [110]; and (3) RF quench field close to the superheating field for temperatures $T \gtrsim 16\,\mathrm{K}$ [66]. The attained B_{pk} values are significantly higher than $\mu_0 H_{\mathrm{c1}}$ as derived from the electron mean free path extracted from low field surface impedance measurements, suggesting that vortex penetration at H_{c1} is not a limitation [66], but never exceeded $B_{\mathrm{pk}} \approx 135\,\mathrm{mT}$ [66, 102, 111] ($E_{\mathrm{acc,\,TESLA}} \approx 32\,\mathrm{MV/m}$).

Part of the measurement results that are discussed in the following were already published elsewhere. For surface resistance data refer to [100], the RF critical field is discussed in [76].

The goal of the measurement discussed here was to perform an RF characterization of as many parameters as possible that are relevant, i.e. defining the SRF performance, of a Nb_3Sn sample that was prepared in the same way as an accelerating cavity. In the first place, the surface resistance has to be recorded as a function of RF field, temperature and at different frequencies. This will directly translate to the achievable quality factor of an accelerating cavity and hence the cryogenic heat load. Secondly, the RF quench field corresponds to the maximum achievable RF field and hence the accelerating gradient. Penetration depth, critical temperature and superconducting energy gap will provide insights about the superconducting state, comparing those values to literature helps to evaluate the coating process.

[3] This value is calculated using Eq. 2.28 with $\kappa = 41$ and $\mu_0 H_{\mathrm{c}} = 520\,\mathrm{mT}$, both values are taken from [109].

4.1 Sample Preparation

The sample characterized in this work was prepared at Cornell University using the coating procedure commonly applied to single cell cavities [112]. As substrate material RRR 300 fine grain bulk niobium was used. Apart from small differences, the substrate geometry corresponds to the one introduced in Section 3.4. The development of a demountable sample chamber assembly was especially necessary for this test, since a pure niobium substrate, i.e. without stainless steel flange, is mandatory for the diffusion coating process. Prior to coating, the substrate was characterized at HZB showing very good residual resistance of about 4 nΩ and high RF critical field $B_{c,RF} = 220\,\mathrm{mT}$. Results are published as "Sample B" in [80].

For coating, the substrate is placed into a UHV furnace with a $SnCl_2$ tin source inside. The system is equipped with two heaters, allowing to independently control the temperature of the tin source and the niobium substrate. In a first step, both parts are heated up to 500 °C where tin evaporates from the source and forms nucleation sites on the niobium substrate. The actual coating consisting of diffusion of tin into niobium along with alloying to Nb_3Sn happens at a substrate temperature of 1100 °C with the source heated even further to 1200 °C. After 3 hours of coating, the source heater is switched off while the sample is kept at high temperature for approximately 6.5 hours in order to allow for further annealing and grain growth. For details on the coating process refer to [55]. Pictures of the sample chamber before and after coating with Nb_3Sn are shown in Fig. 4.1.

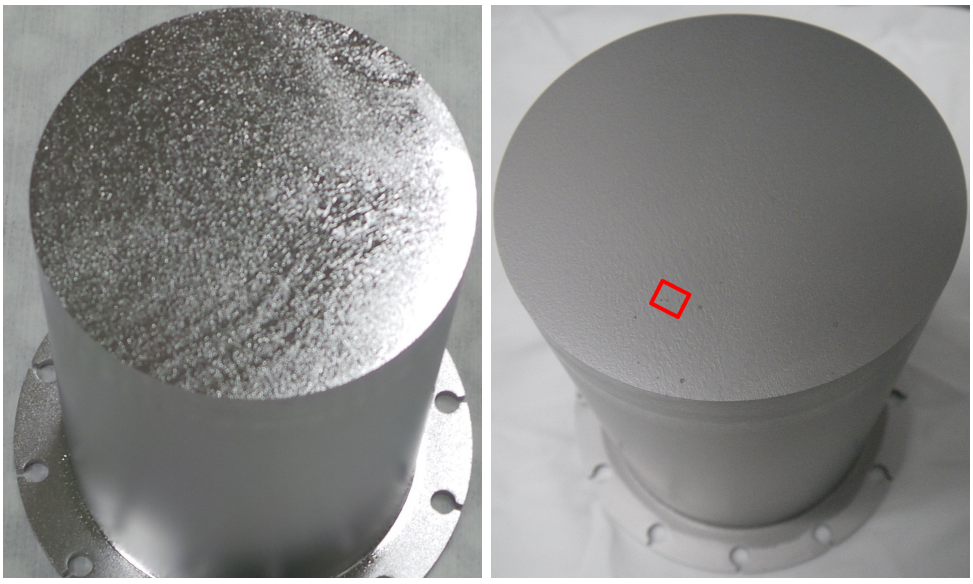

Figure 4.1: *QPR sample before (left) and after (right) coating with Nb_3Sn. The red colored rectangle highlights four black spots that are later investigated using an electron microscope (see Section 4.5.2 and Fig. 4.15a).*

4.2 Surface Resistance Measurements

For the sample discussed in this work surface resistance data is available for temperatures in the range of 2 to 10 K and RF fields of 10 to 70 mT, limited at high field by RF heating. Measurements were restricted to the first two quadrupole modes at frequencies of 414 and 846 MHz due to instrumentation issues. Compared to the geometry of a TESLA-shaped elliptical cavity, the RF field range corresponds to accelerating gradients E_{acc} of 2.3 MV/m to 16.4 MV/m [40]. This is similar to measurements of Nb_3Sn coated cavities [113], but rather incidentally than given by an intrinsic similarity. Note that the Nb_3Sn coating covers all exterior surfaces of the sample chamber. For that reason, RF losses on the sidewall of the sample are negligible and do not cause any bias in surface resistance measurements at high temperature.

Exploring the parameter space of sample temperature and RF field strength, the surface resistance was measured in data sets of varying RF field at constant temperature each. This is more time efficient than reversely, since after every change in sample temperature the reference heater power has to be recorded. During post-processing, $R_{\mathrm{S}}(T)$ curves are extracted for each value of RF field. Figs. 4.2 and 4.3 show exemplary curves of surface resistance vs. RF field and sample temperature, which also present the measurement limitations for that sample.

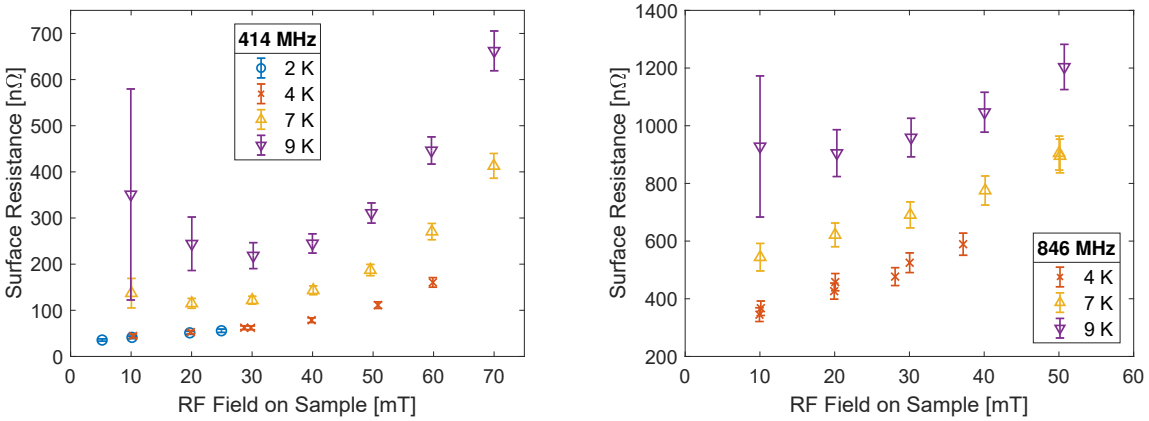

(a) 414 MHz *(b) 846 MHz*

Figure 4.2: *Surface resistance vs. RF field at different frequencies. Measurements towards higher fields are limited by RF heating. At low field, the uncertainty increases with temperature due to the small relative change in heater power.*

Towards low RF field, the measurement uncertainty increases due to the small relative change of DC heater power, as discussed in Section 3.3.2. This especially impacts the data analysis of $R_{\mathrm{S}}(T)$ at 10 mT towards increasing temperature (see Fig. 4.2). The maximum RF field accessible at a given sample temperature is limited by RF heating, i.e. the surface resistance. Note that at high temperature an increasing range of RF field can be accessible, even though R_{S} increases

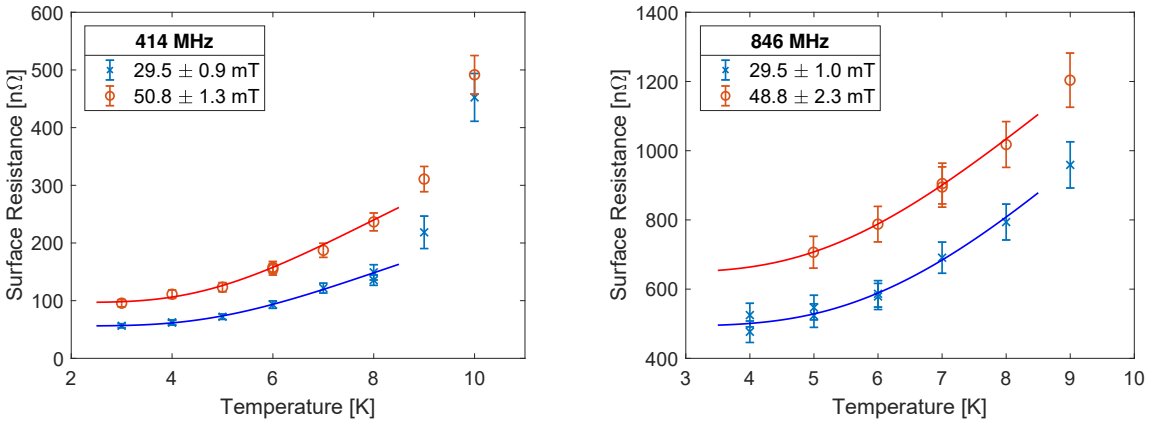

(a) *414 MHz* **(b)** *846 MHz*

Figure 4.3: *Surface resistance vs. sample temperature and corresponding BCS fits. The low-temperature limit of each $R_S(T)$ curve results from the high-field limit of the corresponding $R_S(B)$ curve. See e.g. R_S (846 MHz, 4 K, 40 mT) in Fig. 4.2b.*

exponentially (see Fig. 4.2). Looking again at $R_S(T)$, heating limits the minimum temperature on each curve. The impact of high surface resistance is especially visible at 846 MHz: At 50 mT, data is available above 5 K only, which results in only few points on this $R_S(T)$ curve (see Fig. 4.3b).

For each $R_S(T)$ curve the BCS approximation

$$R_S(T) = \frac{a}{T}\left(\frac{f}{414\,\mathrm{MHz}}\right)^2 \exp\left(-\frac{\Delta}{k_B T}\right) + R_{res} \tag{4.1}$$

is used to extract residual resistance R_{res}, BCS scattering parameter a, and the superconducting energy gap Δ. Note that a is normalized to the first quadrupole mode frequency. Fig. 4.4 shows the resulting parameters for both frequencies as a function of RF field. Fit data is available at integer multiples of 10 mT, straight lines are intended for illustration only. It can be disputed, if the restriction $T < T_c/2$ of Eq. 4.1 allows $T = 9$ K to be taken into account or not. In order to investigate the fit stability, dark colored areas in Fig. 4.4 represent the scatter of fit results if changing the upper temperature limit of the fits in the range of 7 to 9 K. Light colors show the maximum standard deviation of all fit parameters due to the uncertainty of input data points. Due to the very limited number of data points the BCS fits have non-negligible uncertainties. A detailed analysis of the resulting errors is given in [96].

Applying Eq. 4.1 to earlier experimental data, the surface resistance of Nb_3Sn was found to depend on temperature and RF frequency as [54] (see also Eq. 2.16)

$$R_{S,\,Nb_3Sn} = \frac{16.1\,\mu\Omega\mathrm{K}}{T}\left(\frac{f}{414\,\mathrm{MHz}}\right)^2 \exp\left(-\frac{3.4\,\mathrm{meV}}{k_B T}\right) + 2.74\,\mathrm{n}\Omega\left(\frac{f}{414\,\mathrm{MHz}}\right)^2. \tag{4.2}$$

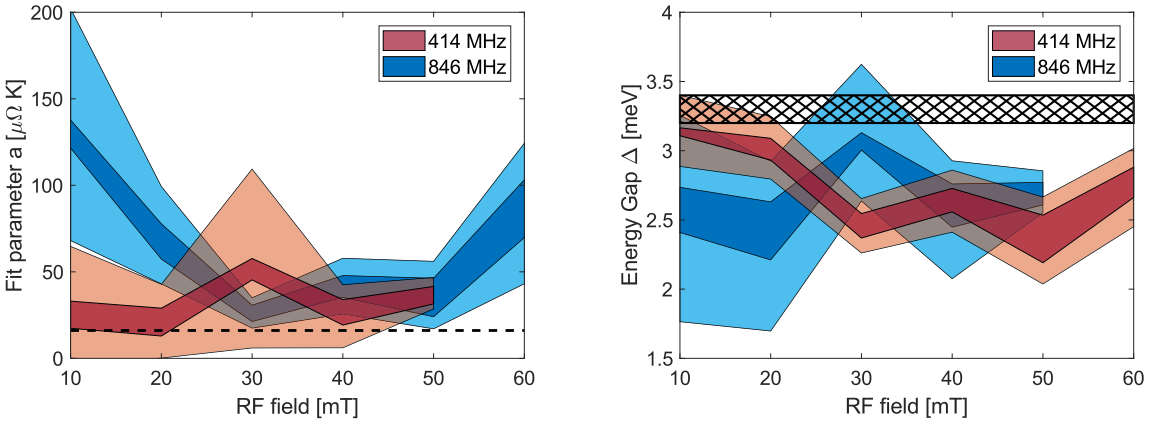

(a) BCS scattering factor a *(b) Energy gap Δ*

Figure 4.4: *Resulting BCS parameters obtained from fitting $R_S(T)$ curves for different values of RF field at frequencies of 414 MHz and 846 MHz. In the left plot the expected value of 16.1 μΩK according to Eq. 4.2 is indicated by a dashed horizontal line. In the right plot, a cross-hatched area shows the energy gap of Nb_3Sn for compositions close to stoichiometry [114].*

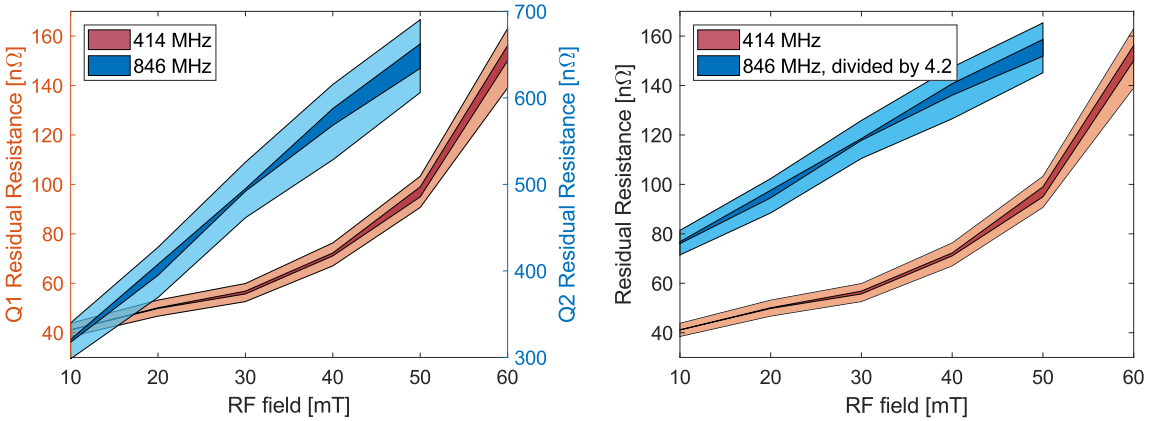

Figure 4.5: *Left: Residual resistance as obtained from fitting $R_S(T)$ data. In the right-hand plot R_{res} at 846 MHz is scaled assuming a quadratic dependence on frequency which is expected for intergrain losses.*

The lowest obtained values for the BCS scattering parameter a as shown in Fig. 4.4a are compatible with this empirical expectation of 16.1 μΩK, however the fit results scatter strongly and tend towards higher values, i.e. higher resistance. The values of Δ (see Fig. 4.4b) also scatter strongly and indicate values lower than expected for the case of stoichiometric composition. As we will see later in discussion of surface analysis data (see Section 4.5), tin depleted areas are present on the RF surface. According to the binary Nb-Sn phase diagram off-stoichiometric composition of lower fractional tin content leads to a reduced superconducting energy gap [114], in agreement with the values obtained here.

In contrast to the BCS parameters a and Δ, the residual resistance as shown in Fig. 4.5 can be determined within reasonable confidence limits. A strong dependence of R_{res} on both, frequency and field is observed. The increase with frequency cannot be explained by normal conducting losses $\left(R_{\mathrm{res}} \propto \sqrt{f}\right)$ which also excludes dominant residual resistance caused by trapped magnetic flux. From intergrain losses a scaling $R_{\mathrm{res}} \propto f^2$ is expected (see Section 2.1.4) which could be an explanation but still underestimates the actual scaling factor of 6.7 to 8.8, corresponding to a frequency scaling of $f^{2.7}$ to $f^{3.0}$. Within the uncertainties of the fitted residual resistance, a frequency scaling factor independent of RF field is possible. However, the phenomenological expression of Eq. 4.2 predicts values for R_{res} of 2.8 nΩ to 11.5 nΩ for the frequencies used in this study, indicating additional unexplained resistance contributions.

The simplified models represented by Eqs. 4.1 and 4.2 do not contain any dependence on the RF field. Hence, the field dependence of the resulting BCS parameters might be misleading. Recent theoretical work on the underlying assumptions of BCS and Mattis-Bardeen theory yielded models incorporating both, residual and RF field dependent surface resistance (see Section 2.1.3). However, given the high values of R_{res} at all levels of RF field and the non-stoichiometric Δ, a numerical analysis according to [38] is omitted since in this case physically meaningful results describing the properties of Nb_3Sn are not expected.

The critical field measurement will show that coating flaws locally suppress the Ginzburg-Landau parameter κ and the superheating field (see Section 4.4). Further, significant surface roughness has been identified as a possible issue of Nb_3Sn films prepared by diffusion coating [72]. A model of quenched grain boundaries has been used to successfully describe high-field Q-slope behavior of fine grain Nb cavities [71]. A similar mechanism of localized losses in small-sized quenched areas might be the cause of the strong Q-slope seen for this sample. Furthermore, as we will see later in the discussion of results from electron microscopy, regions of insufficient film thickness and tin depletion are identified on the sample surface. This has consistently been found before (e.g. [115]), and can be explained by inhomogeneities in the nucleation phase of the coating process. Contributions to RF losses from niobium-tin phases other than Nb_3Sn having a lower T_{c}, or even by the niobium substrate, are well compatible to the BCS fit result of an energy gap Δ being lower than 3.1 meV as expected from literature [16, 114]. Also, those weakly superconducting regions would explain a significant amount of residual resistance.

4.3 Penetration Depth

The penetration depth was measured using the PLL-based method (see Section 3.6.1) at the first two quadrupole modes (414 MHz and 846 MHz). During this measurement campaign, the frequency drift due to the decreasing liquid helium level was not recorded in a dedicated long-term measurement. Hence, the corresponding pressure sensitivity is derived from the penetration depth measurement itself. Fig. 4.6a shows measured raw data of frequency shift vs. sample temperature at the first quadrupole mode. For each mode, the temperature was increased to $T > T_c$ and decreased again. A successful helium level correction will – at least – overlap the data points at low temperature. For this reason, the temperature range of 6 to 10 K is used to derive the correction. This choice might appear arbitrary, but changing the upper limit by up to 2 K has no significant impact on the calculated pressure sensitivity. Since the change of helium level during the time of measurement is known, the observed frequency shift with time ($\mathrm{d}f/\mathrm{d}t$) is converted to a shift as a function of hydrostatic pressure. The correct pressure sensitivity $\mathrm{d}f/\mathrm{d}p$ is found with a trial-and-error method: A wide range of values for $\mathrm{d}f/\mathrm{d}p$ is applied for pressure compensation, subsequently a linear fit to each data set is computed. Fig. 4.6b shows the sum of squared errors (SSE) for all fits. Since all fits contain the same number of data points, the SSE directly measures the quality of $\mathrm{d}f/\mathrm{d}p$ and depends quadratically on the mismatch between applied and ideal value. Hence, the minimum of the interpolated parabola is chosen for the following analysis. The resulting values of $\mathrm{d}f/\mathrm{d}p$ as given in Tab. 4.1 are significantly higher than the ones in Tab. 3.2 which were obtained in another measurement run. This underlines the sensitivity of the resonator to mechanical pre-stress (see Section 3.2.3) and the necessity of doing this analysis for every measurement run.

Table 4.1: *Pressure dependence of resonant frequencies and liquid helium level compensation for the Nb_3Sn penetration depth measurement.*

Mode	$\mathrm{d}f/\mathrm{d}t$	$\mathrm{d}l_{\mathrm{He}}/\mathrm{d}t$	$\mathrm{d}f/\mathrm{d}p$
414 MHz	11.08 Hz/min	1.30 %/h	2.36 kHz/mbar
846 MHz	15.70 Hz/min	1.05 %/h	4.11 kHz/mbar

After helium level correction, the non-linear fit of Eq. 3.29 is computed, yielding T_c and λ_0, the effective penetration depth extrapolated to 0 K. The measurement data for temperature and frequency is obtained with high accuracy, however, environmental influences like pressure fluctuations and temperature gradients acting as systematic uncertainty may have significant impact on the fit. Again, a data-based method is used to extract an effective uncertainty of the fit results. The data set is split w.r.t. increasing or decreasing temperature. Then, the lower and upper temperature limits used for the range covered by the fits are varied, yielding values of root-mean-square-error (RMSE) as shown in Fig. 4.6d for the first quadrupole mode. For 846 MHz data see Appendix Section A.5. Note, that for this analysis RMSE = $\sqrt{\mathrm{SSE}/\mathrm{DFE}}$

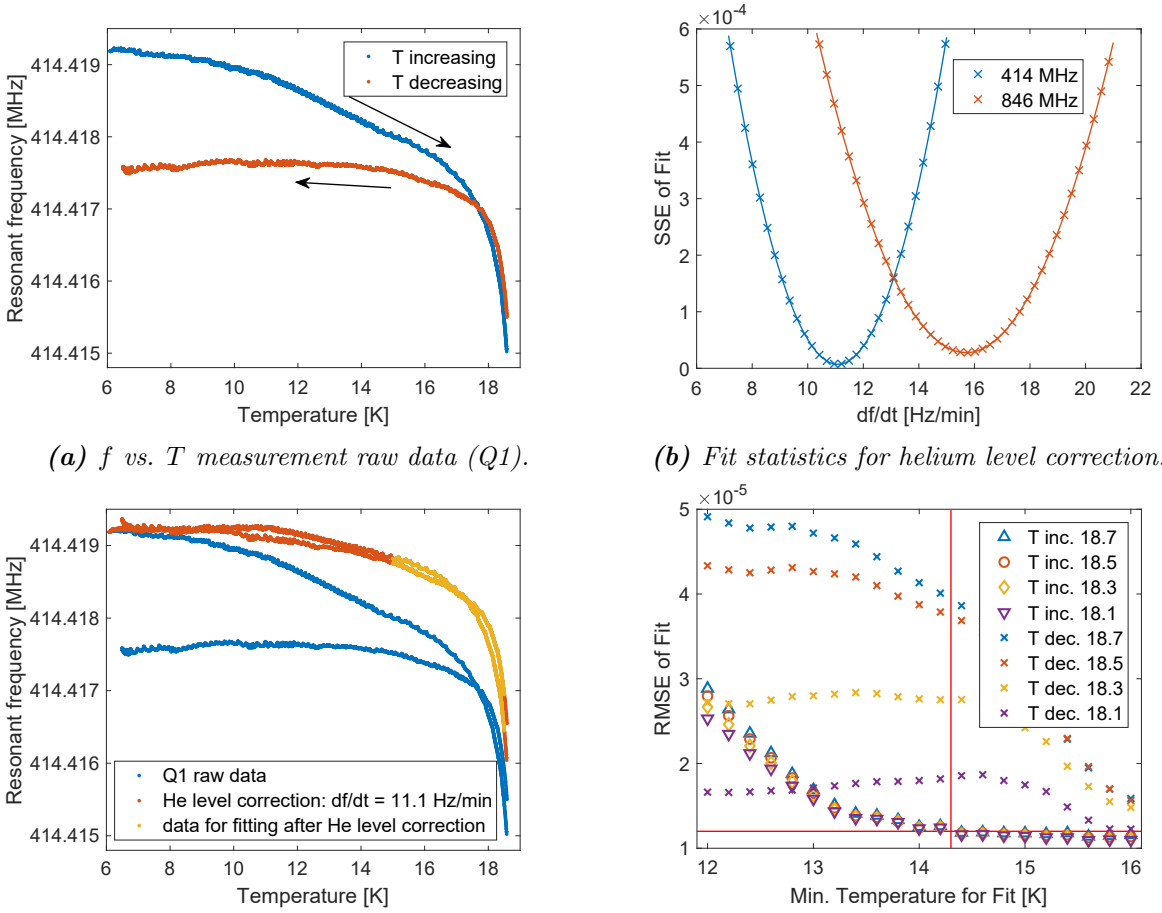

(a) f vs. T measurement raw data (Q1).

(b) Fit statistics for helium level correction.

(c) Effect of helium level correction.

(d) RMSE of penetration depth fits at 414 MHz.

Figure 4.6: *Liquid helium level correction and data processing for the penetration depth measurement. Red lines in Fig. 4.6d highlight the data selection, at 414 MHz only data points for increasing temperature and $T > 14.2\,K$ are used for further analysis.*

with DFE denoting the number of degrees of freedom has to be used, to make the fits of different input range comparable. The trend of decreasing RMSE for tighter fit limits is not surprising. However, at both frequencies only the data for increasing temperature shows consistently low values of RMSE. At 414 MHz and for $T_{\mathrm{min}} > 14.2\,\mathrm{K}$ stable RMSE is obtained, being only weakly dependent on fit limits. The same holds for 846 MHz for even lower T_{min}, i.e. less tight fit limits, but excluding the data at highest temperatures $T > 17.8\,\mathrm{K}$. For both frequencies, the data set of decreasing temperature yields significantly higher RMSE and very unstable fit parameters. The dependence of fit results on the input fit limits follows the same trend for both frequencies, indicating a systematic error due to thermal issues. For that reason, data sets for decreasing temperature are excluded from further analyses. The results are summarized in Tab. 4.2, the fit procedure and its uncertainties for 414 MHz are shown in Fig. 4.7. Corresponding plots for the second mode can be found in Appendix Section A.5. With the fit results for λ_0 and values

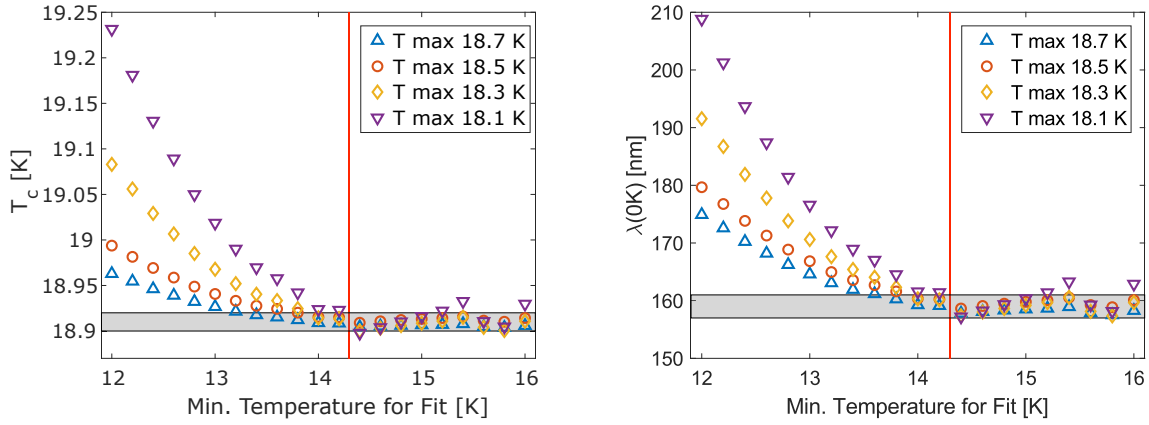

Figure 4.7: *Penetration depth results at 414 MHz: Only data points for $T > 14.2\,K$ are taken into account, gray areas show the uncertainties of resulting fit parameters.*

Table 4.2: *Results of the penetration depth measurement for Nb_3Sn. T_c and $\lambda(0)$ are directly given by non-linear fits; ℓ, κ and critical fields are derived using the weighted average $\lambda_0 = (160 \pm 2)\,\mathrm{nm}$ and values for λ_L, ξ_0, and H_c from literature as given below.*

Frequency	414 MHz	846 MHz	
T_c	$(18.91 \pm 0.01)\,\mathrm{K}$	$(18.15 \pm 0.04)\,\mathrm{K}$	
$\lambda(0\,\mathrm{K})$	$(159 \pm 2)\,\mathrm{nm}$	$(164 \pm 6)\,\mathrm{nm}$	
λ_L	$90\,\mathrm{nm}$		[58]
ξ_0	$7\,\mathrm{nm}$		[58]
$\mu_0 H_\mathrm{c}$	$520\,\mathrm{mT}$		[109]
λ_0	$(160 \pm 2)\,\mathrm{nm}$		
ℓ	$(2.4 \pm 0.1)\,\mathrm{nm}$		
κ	44.8 ± 1.1		
$\mu_0 H_\mathrm{c1}$	$(39.3 \pm 0.6)\,\mathrm{mT}$		
$\mu_0 H_\mathrm{sh}$	$(430.3 \pm 0.5)\,\mathrm{mT}$		

for λ_L, ξ_0 and H_c from literature, the electron mean free path ℓ, Ginzburg-Landau parameter κ and critical fields are derived, using the respective equations introduced in Section 2.2.1.

Both values for the penetration depth extrapolated to low temperature agree very well within their statistical uncertainty. In summary a weighted average of $\lambda_0 = (160 \pm 2)\,\mathrm{nm}$ is obtained. The reason for the discrepancy of T_c values is not clear, fits at both quadrupole modes converge with comparatively small uncertainty. One possible explanation could be different temperature gradients on the sample surface, since individual thermal cycles were used for each frequency. At the time of this experiment, thermal cycles were not standardized, leading to potentially irreproducible behavior. This would explain the disagreement of T_c values as well as the discrepancy of measurement data for increasing and decreasing temperature at each mode.

4.4 RF Critical Field

The RF quench field was measured at 414 MHz and various temperatures using software-triggered single pulses of high RF power as described in Section 3.5. Given by RF instabilities and the quenching resonator, measurements were possible up to $B_{\text{quench}} < 100\,\text{mT}$, corresponding to sample temperatures $T > 8\,\text{K}$. Exemplary pulse traces are given in Fig. 4.8, Fig. 4.9 shows the measured RF quench field vs. temperature on a linear scale.

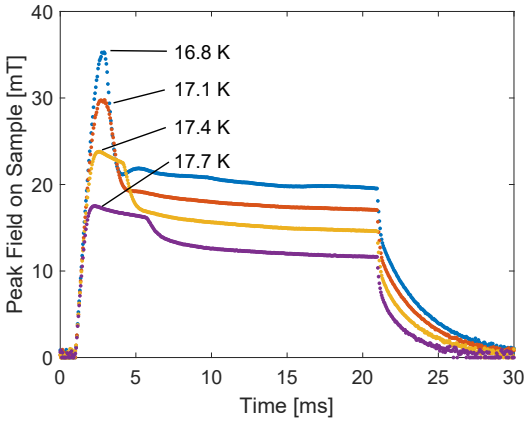

Figure 4.8: *RF field on the sample surface measured at the pickup probe at four different temperatures. A constant pulse length of 20 ms was used. The RF quench field is given by the peak value.*

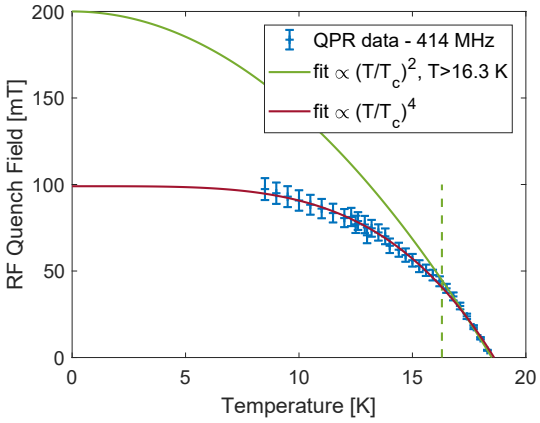

Figure 4.9: *RF quench field measurement data. The full data range can be described by a temperature dependence $\propto (T/T_c)^4$. For the fit to Eq. 3.17 only data with $T > 16.3\,K$ is used, as highlighted by a dashed line.*

For interpreting the obtained data the question remains, whether this quench is triggered by a global effect of exceeding the superheating field or locally in a region where the superheating field is suppressed. Alternatively, it is also possible that the quench is triggered prematurely by a thermal effect where a defect causes significant pre-quench RF heating. To analyze the possible impact of pre-quench heating, which would falsify the assumed sample temperature, the quenched sample area is estimated from the acquired pulse shapes according to the procedure described in Section 3.5. Fig. 4.10a shows a typical pulse trace with fits for post-quench decay time τ_{quench} and unperturbed falling edge decay time τ_{L}. After the RF drive power is switched off, the sample becomes superconducting within a few 100 µs, as visible from exponential fits to the falling edge decay curve (see Fig. 4.10a). Since $\tau_{\text{quench}} \approx 0.3\,\tau_{\text{L}}$ the surrounding QPR has still a significant impact on the true quench time τ_{q}. This is taken into account with the usual partition of quality factors, and hence decay times, using

$$\tau_{\text{q}} = \frac{\tau_{\text{L}}\tau_{\text{quench}}}{\tau_{\text{L}} - \tau_{\text{quench}}}. \tag{4.3}$$

With τ_q and the electrical resistivity of Nb_3Sn in the normal conducting state (8 to 20 µΩ cm [16]), the quenched sample area is estimated yielding 2 to 4 mm^2. Note that for $T > 16$ K the increasing temperature dependent surface resistance of the sample begins to reduce the decay time τ_L of the superconducting state (see Fig. 4.10b). For $T > 17$ K, the change of loaded quality factor decreases such, that no steep decrease of transmitted power is observed anymore. As mentioned earlier (see Section 3.5), the jump in resonant frequency at the instant of the quench decreases due to the increasing penetration depth when approaching T_c. Eventually, the penetration depth is very close to the normal conducting skin depth and the PLL keeps lock. In this case, fits of τ_{quench} are meaningless to deduce the quenched sample area. The increase observed for the 17 K point in Fig. 4.10b hence is considered to reflect this measurement difficulty. This behavior is also visible in the pulse traces shown in Fig. 4.8.

However, the fact that for $T < 17$ K τ_{quench}, and hence the quenched area, does not depend on temperature (see Fig. 4.10b) is a strong indication of a localized quench spot without excessive pre-quench heating affecting the measurement accuracy. In comparison, measurements of a bulk niobium sample with RF quench fields consistent with the global superheating limit showed a quench area of about 100 mm^2.

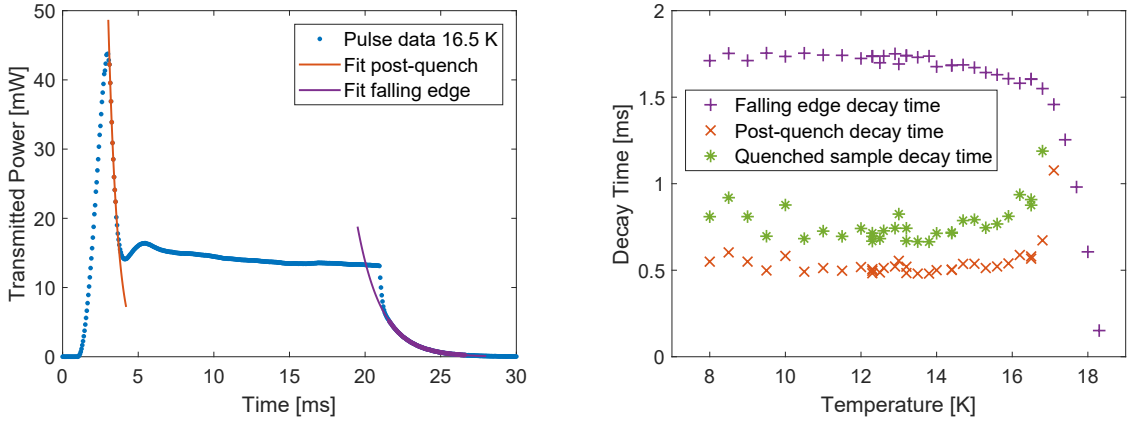

(a) *Typical pulse trace with fits for quenched decay time τ_{quench} (orange curve) and unperturbed falling edge decay time τ_L (purple curve). Colored data points indicate the data ranges used for fitting.*

(b) *τ_L, τ_{quench} and τ_q as a function of sample temperature. For $T > 16$ K the increasing surface resistance of the sample reduces τ_L. For $T > 17$ K no post-quench decay times can be derived.*

Figure 4.10: *Pulse trace analysis and quenched sample area.*

Looking at the temperature dependence of the measurement data shown in Fig. 4.9, the RF quench field as a function of temperature can be described by the empirical relation according to Eq. 3.17 only in the temperature range $T > 16.3$ K. Expanding the fit data range to lower temperature reduces the fit quality significantly as visible in Fig. 4.11. Extrapolation to low temperature using Eq. 3.17 yields $\mu_0 H_{c,RF} = (200 \pm 5)$ mT and $T_c = (18.5 \pm 0.1)$ K. The value of T_c is in agreement with the result of the penetration depth measurement. However, $H_{c,RF}$ is about a factor of two below the predicted superheating field $\mu_0 H_{sh} = 430$ mT, but clearly

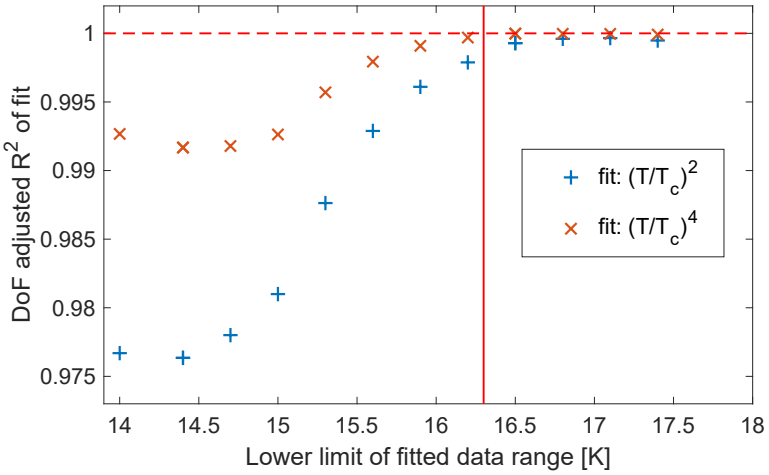

Figure 4.11: *Study of fit quality when varying the low-temperature limit of the fitted data range. The degree of freedom (DoF) adjusted R^2 values are shown for both, quadratic and quartic temperature dependence of $H(T)$. A vertical line at 16.3 K indicates the fit limit used in Fig. 4.9.*

exceeds the lower critical field $\mu_0 H_{c1} = 39\,\mathrm{mT}$ (see also Tab. 4.2). In agreement with the surface resistance measurement this confirms that H_{c1} is not a limitation for RF fields, hence no vortex penetration happens at H_{c1} (see also [66, 76]).

One cause of reduced vortex penetration field might be surface roughness. Recent analysis of Nb_3Sn surfaces showed roughness causing local field enhancement exceeding 50 % [72]. In that case, the measured $H_{c,RF}$ should not reach the theoretical values, but be suppressed by a factor 1/1.5. Another explanation for measurement data deviating from the expected quadratic behavior is given by vortex penetration at defects with a size on the order of the coherence length. The VLN model (see Section 2.2.4) gives an heuristic formula for this limitation, predicting a temperature dependence $H_{VLN}(T) \propto -(T/T_c)^4$. This model consistently describes the full data set, yielding $\mu_0 H_{VLN,0} = (100 \pm 3)\,\mathrm{mT}$ and $T_c = (18.6 \pm 0.1)\,\mathrm{K}$. Note that restricting the fit range to the same high-temperature range as used for the quadratic model (see Fig. 4.9), still yields a higher adjusted R^2 value for VLN (see Fig. 4.11). VLN has been applied to earlier measurements on Nb_3Sn and also showed better agreement than a quadratic fit [65, 66]. Putting the values of $\mu_0 H_{VLN,0}$ and $\mu_0 H_c = 520\,\mathrm{mT}$ [109] into Eq. 2.31 yields $\kappa = 5.2 \pm 0.2$. This value of κ is very small if compared to one from the penetration depth measurement or other experimental results from low field surface impedance ($\kappa = 43$ to 112 [66]) and low energy μSR measurements ($\kappa = 60 \pm 15$ [76]). A possible interpretation of these results is, that the values of κ might be locally suppressed and for this reason, the VLN model cannot give a quantitative prediction that represents the entire surface. However, a deviation from the quadratic temperature dependence can still be interpreted as local flux penetration at defects [76].

4.5 SEM Investigation

After RF characterization, a scanning electron microscope (SEM) available at JLab[4] was used for further surface analysis, data was taken by A.-M. Valente-Feliciano [116]. The setup uses a TESCAN VEGA3 device that is capable to host the entire sample chamber without the need of cutting small pieces. Besides a secondary electron (SE) detector for surface topography measurement, an X-ray detector for energy dispersive spectroscopy (EDS) probing the elemental composition was available.

As a result, the Nb_3Sn coating is found to have an atomic ratio of niobium and tin close to stoichiometry on most of the sample. Additionally, two kinds of structures were found which are discussed in the following and that could explain the observed RF performance: "patchy areas" and "white spots".

4.5.1 Patchy Areas

Fig. 4.12 shows two SEM scans of different magnification. Large structures visible as hills and valleys that are laterally up to several hundred µm in size correspond to the surface topography of the niobium substrate. The substrate surface was prepared by buffered chemical polishing (BCP), which is known to exhibit surface roughness on the µm scale and to emphasize grain boundaries. Initially, fine-grain bulk niobium was used, having a typical grain size of 50 µm. The observed grain growth is caused by the high temperatures during the coating process.

The zoomed view in Fig. 4.12b shows flat "patchy areas" with nearly uniform color and irregular shape. Their lateral size varies in the range of 10 µm to 50 µm. In order to study the elemental composition spatially resolved, an EDS map of the area highlighted by a blue square was taken. As visible in Fig. 4.13, all patchy areas show higher niobium content and in turn less tin. For the areas highlighted and labeled yellow, quantitative EDS data is available, see Tab. 4.3.

[4]Thomas Jefferson National Accelerator Facility (JLab), Newport News, VA 23606, USA

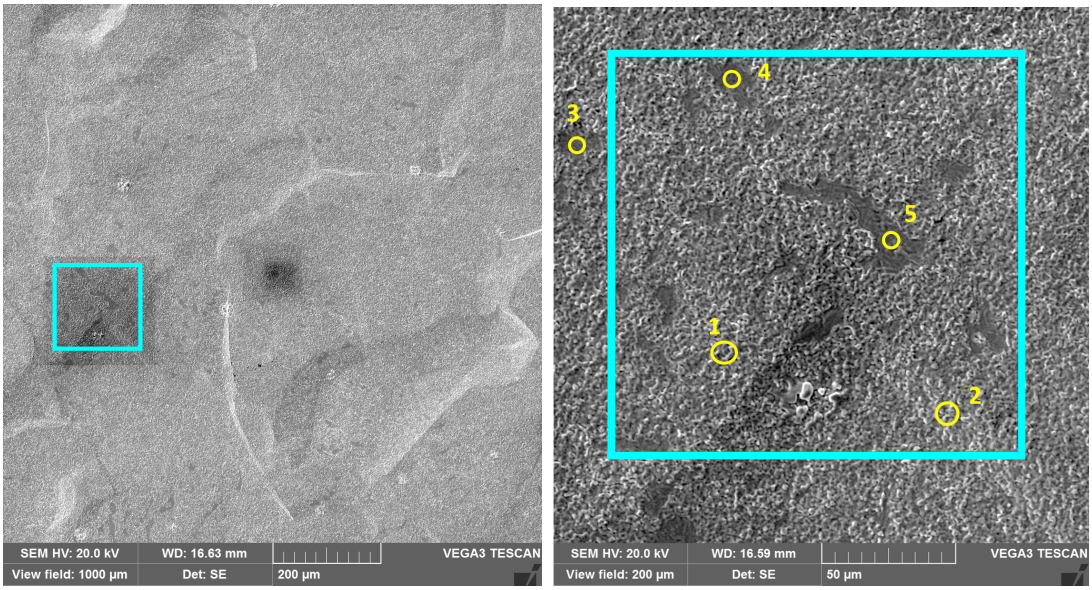

(a) *View field: 1.0 mm* ***(b)*** *View field: 0.2 mm*

Figure 4.12: *SEM images showing large structures associated with the niobium substrate at low magnification (a) and patchy regions of uniform color at higher magnification (b). The brighter structure in the lower third of Fig. (b) denotes a small white spot, as discussed in Section 4.5.2. Quantitative EDS data for the areas marked yellow is given in Tab. 4.3. An EDS map was taken for the area highlighted by a blue square, see Fig. 4.13.*

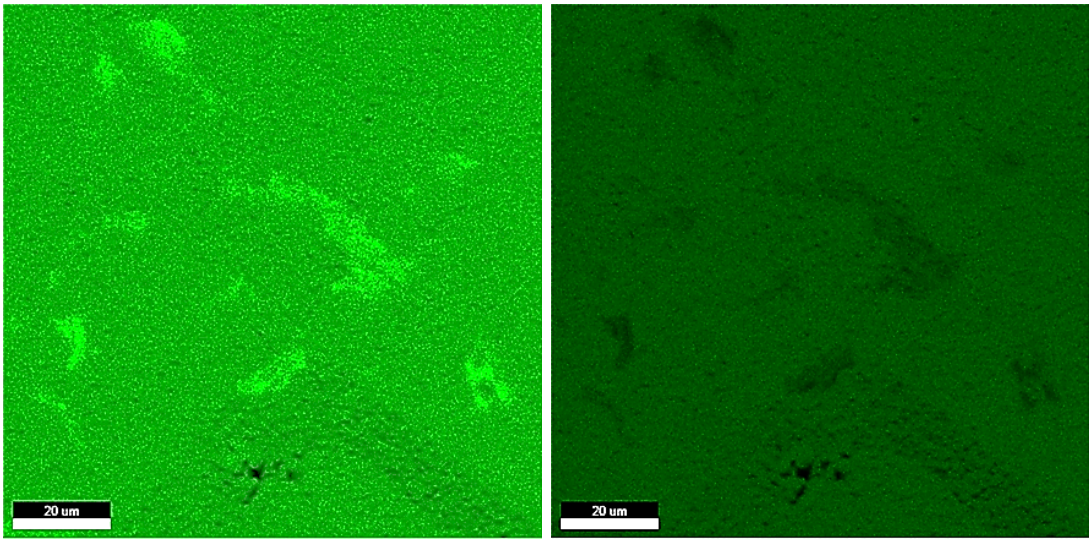

(a) *niobium* ***(b)*** *tin*

Figure 4.13: *EDS maps of niobium and tin for the scan area marked in Fig. 4.12. Flat patchy areas exhibit higher niobium content and in turn less tin, compared to the surrounding material. Note that both surface types show homogeneous composition.*

Table 4.3: *EDS data for the scan areas highlighted yellow in Fig. 4.12b. The areas 1 and 2 show a Nb/Sn ratio close to the stoichiometric value 3. For patchy areas (3–5) the relative tin content is significantly lower.*

Area	Nb [at.%]	Sn [at.%]	C [at.%]	O [at.%]	Ratio Nb/Sn
1	68.7 ± 1.4	22.5 ± 0.5	5.8 ± 0.9	3.0 ± 0.6	3.05 ± 0.09
2	69.6 ± 1.5	21.6 ± 0.5	6.0 ± 0.9	2.8 ± 0.6	3.22 ± 0.10
3	75.6 ± 1.5	15.8 ± 0.4	6.0 ± 0.9	2.6 ± 0.5	4.80 ± 0.15
4	75.6 ± 1.6	15.8 ± 0.5	5.8 ± 0.9	2.7 ± 0.5	4.78 ± 0.17
5	72.9 ± 1.5	18.6 ± 0.5	5.9 ± 0.9	2.5 ± 0.5	3.93 ± 0.13

The areas 1 and 2 show a Nb/Sn ratio close to the stoichiometric value 3. For the patchy areas (3, 4 and 5) values of 3.9 to 4.8 are obtained, corresponding to an atomic tin content of only 17.2 to 20.3 at.% if calculated for the binary system niobium-tin.

The question remains, if those values can be interpreted as surface tin deficiency, since the SEM measurement gives a volume average over the electron penetration depth which in turn depends on the accelerating voltage. This issue was addressed in [115] using a combination of SEM and cross-sectional transmission electron microscopy (TEM) measurements on Nb_3Sn cavity cutout samples. "Cold" cutouts with Nb_3Sn film thickness of 3 µm as intended did not show any deficiency for SEM voltages $U \leq 30\,\mathrm{kV}$. For patchy regions similar to the ones observed here, a film thickness of less than 100 nm was measured along with SEM data indicating tin deficiency at accelerating voltages down to $U = 13\,\mathrm{kV}$ [115]. Looking at the RF penetration depth of 160 nm (see Tab. 4.2), this film thickness is not sufficient to carry all RF currents and to fully screen the substrate. Hence, an electron accelerating voltage of $U = 20\,\mathrm{kV}$ – which was consistently used for this work – is well suited to detect regions with Nb_3Sn coating thickness being too thin for SRF applications. Furthermore, since several multiples of the RF penetration depth are required to fully screen the RF currents, an SEM Nb/Sn ratio close to 3 confirms both, sufficient thickness and correct composition of the Nb_3Sn coating.

Looking back at the $R_S(T)$ fits, the obtained superconducting energy gap Δ was significantly lower than expected for stoichiometric composition (see Fig. 4.4b). The observations of tin deficient regions and decreased values of Δ are in good agreement with the strong dependence of Δ on atomic composition as shown in Fig. 4.14. Hence, patchy regions are likely a cause of increased RF surface resistance. From Fig. 4.14 a similar reduction of T_c would be expected which was not observed in the penetration depth measurement. This is not contradictory since the penetration depth measurement yields a surface average over the high-field region of the sample and the impact of patchy off-stoichiometric regions on the measurement result is suppressed due to the comparatively low surface fraction covered by those structures.

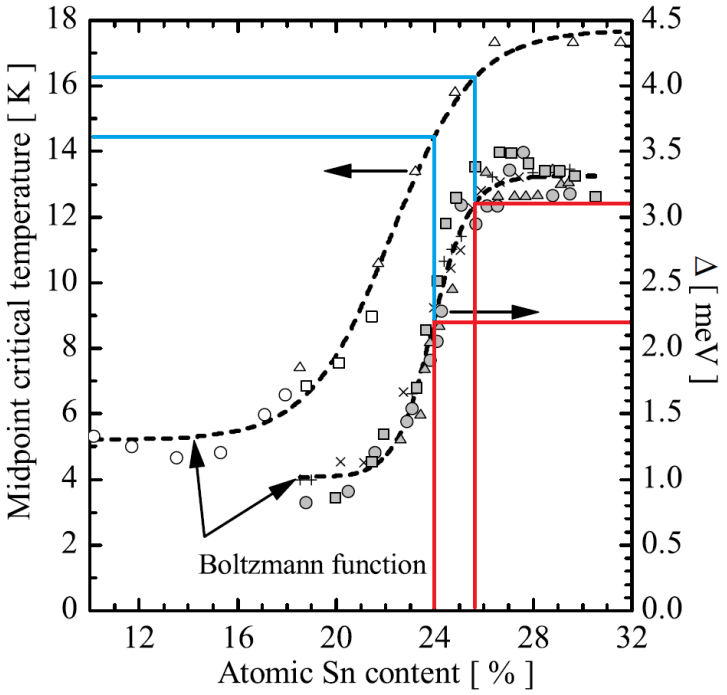

Figure 4.14: *Critical temperature as a function of composition. Colored lines highlight the range of Δ values obtained from $R_S(T)$ fits and corresponding values for tin content and T_c. The plot is reproduced from [114] with initial data of [117].*

4.5.2 White Spots

A second type of suspicious surface structures is given by white spots as visible in Fig. 4.15. Naming those spots "white" only refers to the visual impression from SEM images, as opposed to the rather darkly colored patchy areas described above. The largest spots with diameters of about 400 µm are visible by eye and appear almost black (see red rectangle in Fig. 4.1). Besides few large spots, small white spots with diameter of 20 to 30 µm are present all over the sample surface (see Figs. 4.15b and 4.15c). The high magnification images in Fig. 4.16 show that large and small spots have a very similar structure of "unconnected" grains. The maximum grain size of up to 10 µm is significantly larger than for the surrounding Nb_3Sn film. An EDS map was taken for the area highlighted by a blue square in Fig. 4.16b. The result shown in Fig. 4.17 confirms a laterally uniform composition of those crystalline structures. Quantitative EDS data for the spots and areas marked yellow is given in Tab. 4.4.

Note that all SEM scans were consistently performed with an accelerating voltage of 20 kV. Compared to the patchy areas discussed above, this proves a sufficient thickness of the Nb_3Sn coating inside the white spot areas, screening all RF currents from the niobium substrate. However, the (visually) unconnected grains inside the spots are candidates for enhanced intergrain losses, contributing significantly to the measured RF dissipation. Increased carbon content in some of the white spot areas (EDS area 3 and 5) might be a indication of contaminated grain

boundaries that further weakens the RF current transport properties across individual grains. Theoretical models exist for intergrain losses that predict both field dependent and residual surface resistance [8, 51] (see also Section 2.1.4). Assuming weak coupling and low magnetic fields, however, the observed dependence of the surface resistance on both frequency and RF field is higher than the expectation from such models.

The critical field measurement showed quench fields lower than the superheating limit with small-sized quench areas. Significant field enhancement at prominent grain structures or weakly linked grains as present in those white spot areas could lead to early flux penetration and hence reduced RF quench fields. Note that for this behavior single or few spots are sufficient to limit the performance of the entire sample.

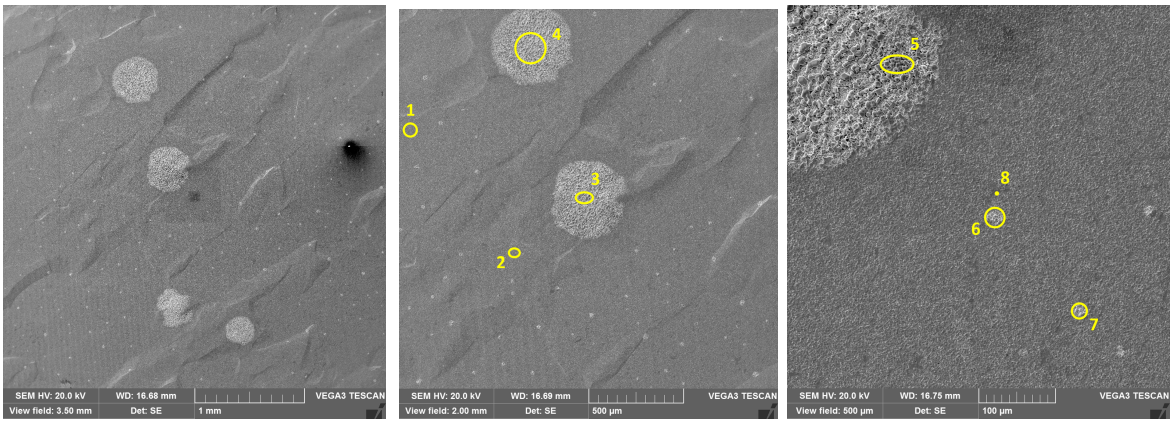

(a) *View field: 3.5 mm* **(b)** *View field: 2.0 mm* **(c)** *View field: 0.5 mm*

Figure 4.15: *SEM images showing large and small white spots at different levels of magnification. At higher magnification (right), patchy areas also become visible. Quantitative EDS data for the spot and areas marked yellow is given in Tab. 4.4.*

Table 4.4: *EDS data for the scan areas highlighted yellow in Figs. 4.15b and 4.15c. The niobium-tin ratio is identical outside (1, 2) and inside (3–7) of white spots. EDS spot 8 is placed inside a patchy region, showing again very little tin content.*

Area	Nb [at.%]	Sn [at.%]	C [at.%]	O [at.%]	Ratio Nb/Sn
1	67.6 ± 1.3	22.2 ± 0.4	7.9 ± 0.8	2.3 ± 0.3	3.04 ± 0.08
2	67.8 ± 1.3	22.5 ± 0.4	7.5 ± 0.7	2.3 ± 0.3	3.02 ± 0.07
3	66.7 ± 1.3	21.5 ± 0.4	8.0 ± 0.8	2.8 ± 0.4	3.10 ± 0.08
4	66.6 ± 1.3	21.3 ± 0.4	8.8 ± 0.9	3.3 ± 0.4	3.12 ± 0.08
5	64.5 ± 1.3	20.9 ± 0.4	10.1 ± 1.1	3.4 ± 0.5	3.09 ± 0.09
6	66.5 ± 1.3	21.6 ± 0.4	7.5 ± 0.8	2.8 ± 0.4	3.07 ± 0.09
7	63.9 ± 1.2	20.8 ± 0.4	11.9 ± 1.1	2.8 ± 0.4	3.07 ± 0.08
8	76.8 ± 1.6	11.0 ± 0.3	9.3 ± 1.0	2.4 ± 0.4	7.00 ± 0.24

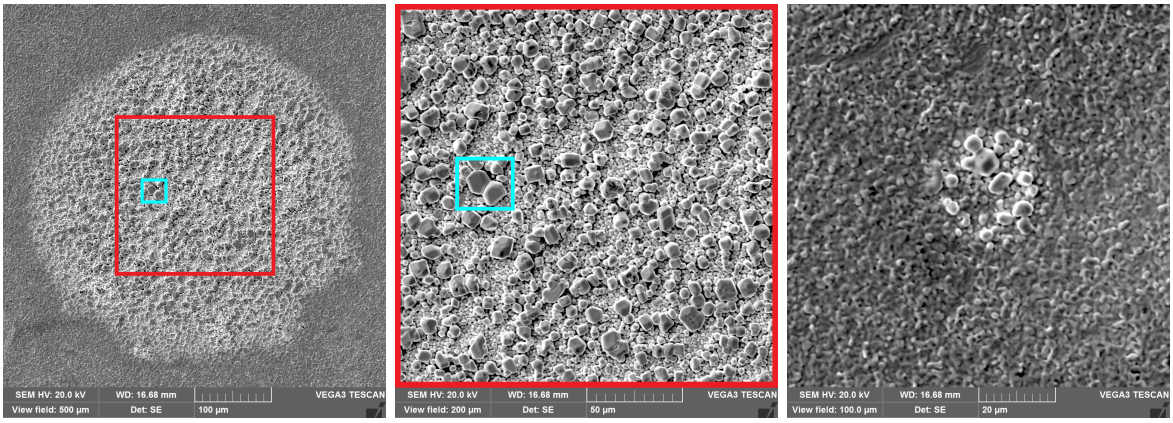

(a) *View field: 500 µm* **(b)** *View field: 200 µm* **(c)** *Small spot, view field 100 µm*

Figure 4.16: *High magnification SEM scans of large and small white spots. An EDS map was taken for the area highlighted by a blue square, see Fig. 4.17.*

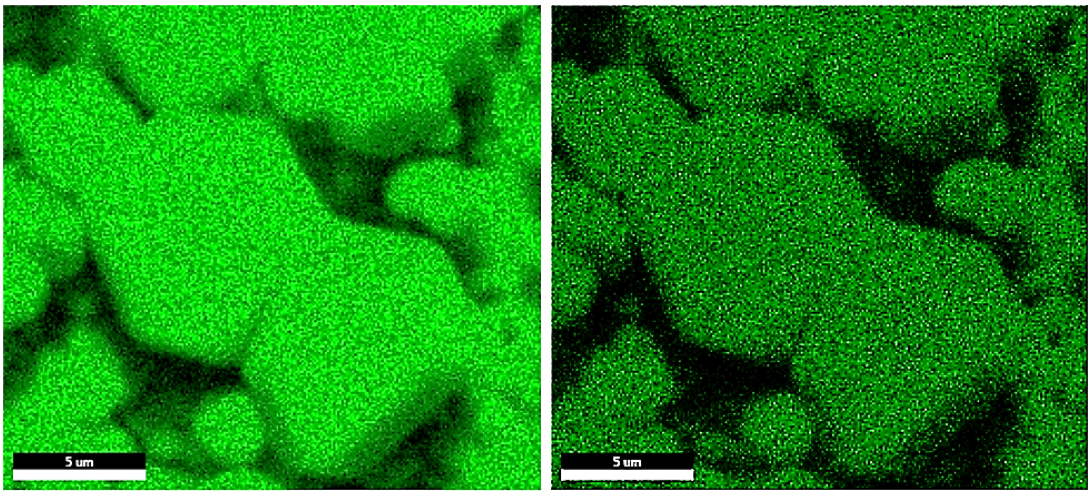

(a) *niobium* **(b)** *tin*

Figure 4.17: *EDS maps of niobium and tin for the scan area marked in Fig. 4.16. The crystalline grains visible in this image show laterally homogeneous composition of niobium and tin.*

4.6 Summary

In summary, the EDS data discussed in Section 4.5, showing a high coverage of the RF sample surface with niobium-tin at a ratio close to Nb_3Sn stoichiometry, is well in line with the results for T_c from measurements of the RF penetration depth and the critical field. For an atomic tin content $\gtrsim 25$ at.% a high transition temperature of about 18 K together with a superconducting gap $\Delta \gtrsim 3.1$ meV is expected [117]. Fits to $R_S(T)$ data give lower values for Δ, however the uncertainty of the results is rather big given by the limited data range and the number of data points.

During penetration depth measurements, a very low RF field is applied and the obtained value corresponds to a surface average of the high-field region. Hence, possible coating flaws in the coaxial structure do not contribute, furthermore the impact of patchy areas and white spots is very low given by the comparatively small area covered by those structures. For surface resistance and critical field measurements this statement does not hold, in these cases single spots or small-sized areas can dominate the results. Those measurements show a superconducting performance of this sample that is significantly below the theoretical limits: The temperature dependence of the RF critical field $\propto -(T/T_c)^4$ indicates early flux penetration according to the VLN model (see Section 2.2.4) and the measured surface resistance exhibits strong field-dependence. The regions of high surface resistance that dominated the R_S measurement showed lower values for Δ than expected for stoichiometric composition. This non-ideal behavior might be attributed to the observation of patchy areas and white spots. In [115], patchy areas of too thin coating were identified on cavity cutouts. Prior to cutting of the samples, the cavity also showed strong Q-slope and high residual resistance in RF measurements. In addition to those patchy regions, white spots found on this specific sample are likely to contribute to the observed surface resistance. Simple models for intergrain losses based on weak Josephson coupling lead to a surface resistance increasing up to quadratically with frequency and applied RF field. Localized heating of those regions, similar to the Q-slope model in [71], might further enhance the dependence on RF field, explaining the observed behavior. White spot areas possibly showing field enhancement at prominent grain structures or weakly linked grains could also lead to early flux penetration and hence explain the reduced RF quench field.

5 RF Characterization of a NbTiN-AlN-Nb Sample

Pushing SRF systems beyond the fundamental limits of (bulk) niobium, thin films and multilayer structures provide another promising way besides Nb_3Sn. Coatings of Nb_3Sn or Nb are considered as "thick" films since the deposited film thickness d is large compared to the RF penetration depth λ, justifying the assumption of one bulk-like superconductor carrying all screening currents. In thin film systems with $d = O(\lambda)$, screening currents are distributed between several layers, requiring an additional thick film or bulk superconductor underneath. Theoretical work shows that coating niobium with a superconductor of higher T_c and specific thickness significantly increases B_{sh} and reduces the BCS surface resistance ([19], see also Section 2.3). Inserting an insulating layer in between the superconductors prevents vortices, that might be generated at defects, from penetrating the entire superconducting structure.

The second sample that was characterized within this work is an S-I-S′ structure of NbTiN and Nb with AlN as intermediate insulator. NbTiN and AlN were deposited by DC magnetron sputtering on a bulk Nb substrate at Jefferson Laboratory (JLab). Prior to coating, a QPR baseline test of the substrate was performed. In the following, the results of baseline and coated sample are discussed simultaneously to provide comparability.

5.1 Sample Preparation

Compared to the Nb_3Sn sample discussed in Section 4, this substrate has a different mechanical design: The Nb part of the sample chamber is not detachable but brazed to the stainless steel flange at the bottom. Furthermore, two EB welds were performed. One circular weld on the RF sample surface, inserting a disk of high RRR Nb into a ring of RRR 50. This ring was then EB welded to the niobium tube that has the same low RRR. Fig. 5.1 shows a picture of the coated sample chamber. The high RRR disk on the RF surface was mechanically polished and possible contamination of the fully assembled sample setup were removed by electro-polishing (EP). After baseline measurement at HZB, the sample was sent back to JLab and cleaned again by EP prior to the coating process. After mounting into the coating chamber and evacuation to $5 \cdot 10^{-10}$ mbar, the sample was heated up to 600 °C ($p = 2 \cdot 10^{-9}$ mbar) to reduce the natural oxide layer of the niobium substrate.

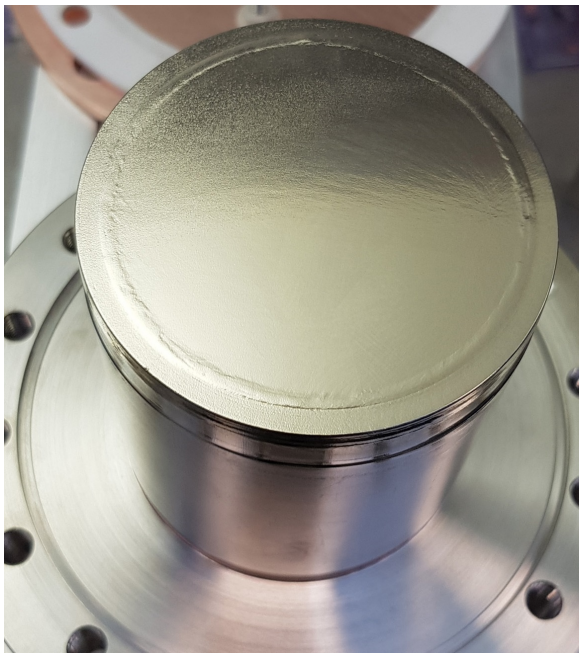

Figure 5.1: *QPR sample with AlN and NbTiN coating on the top RF surface. Electron beam welds are visible on the top surface and on the sidewalls. The niobium tube is brazed to the stainless steel bottom flange. Courtesy: A.-M. Valente-Feliciano (JLab).*

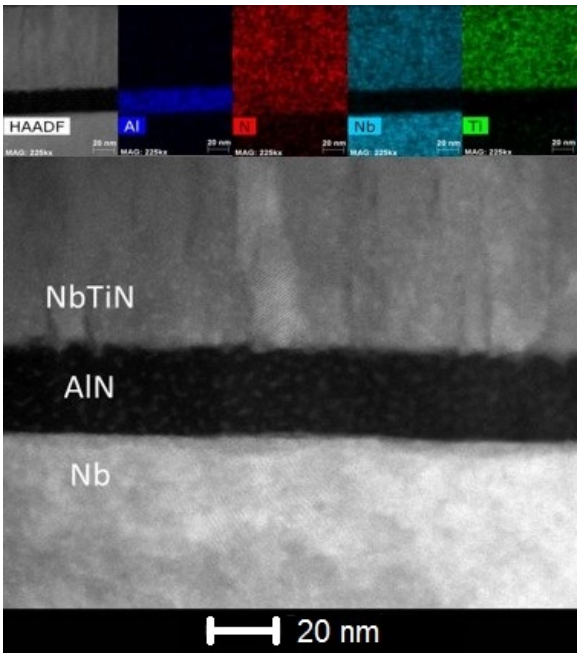

Figure 5.2: *Cross sectional SEM images of a witness sample coating. The bottom part gives a detailed view of the AlN insulating layer and the interfaces to the Nb substrate and the NbTiN upper layer. On top, EDS maps show the composition of the layers. Courtesy: A.-M. Valente-Feliciano (JLab).*

Sequentially, 15 nm of AlN and 75 nm of NbTiN were deposited by DC magnetron sputtering. The coating temperature was set to 450 °C to prevent diffusion of aluminum and corresponding contamination of the substrate or the top layer coating. Given by the deposition technique and the coating chamber setup, only the top RF surface of the sample chamber and its outer edge are covered by the S-I layers. This will later be important to estimate additional RF dissipation during the surface resistance measurement (see Section 5.2). Small witness samples were coated together with the QPR sample. Fig. 5.2 shows a cross sectional composition map of a similar witness sample, coated under comparable conditions with increased insulator height of 20 nm. The composition map was obtained by EDS using an SEM. The cross section was prepared by the focused ion beam (FIB) technique. Well defined interfaces to the Nb substrate and the NbTiN upper layer are visible. The EDS maps also indicate homogeneous composition without visible diffusion of constituents into neighboring layers.

5.2 Surface Resistance

5.2.1 Baseline Measurement

Prior to the coating process, a baseline surface resistance measurement of the bulk niobium substrate was performed at 414 and 846 MHz. As for the Nb_3Sn sample, BCS fits according to Eq. 4.1 were calculated (see Section 4.2). The resulting fit parameters as a function of the applied RF field strength are shown in Fig. 5.3. Measurement data as a function of temperature is shown later, together with the one obtained for the coated sample (see Fig. 5.6a).

The residual resistance is nearly independent of RF field for both frequencies (see Fig. 5.3c). Assuming a field independent scaling factor of $73/23 \approx 3.2$ corresponds to a frequency dependence of $R_{\mathrm{res}} \propto f^{1.63}$. Similar scaling has been observed before on multi-mode test cavities and seems to be typical for bulk niobium [118, 119]. The absolute values however indicate non-ideal behavior, scaling to a 1.3 GHz TESLA-shaped cavity yields $R_{\mathrm{res}} = 150\,\mathrm{n\Omega}$ and $Q_0 = 1.8 \cdot 10^9$ [40]. The residual resistance might be due to increased losses on the outer "ring" of the sample. As mentioned above (see Section 5.1), only the inner "disk" of the sample surface is made of high quality, high RRR niobium. Given by the high temperatures during EB welding, the "ring" may have contaminated the "disk" due to diffusion. In the case of such an inhomogeneity, the true residual resistance of the outer ring would be even higher, since the calorimetric measurement principle always gives a surface average value. Note that the fit uncertainty indicated by semi-transparent areas in Fig. 5.3c is dominated by the systematic RF measurement uncertainty of 9.2 % (see Section 3.5.1). This is mainly relevant when comparing different frequencies since RF calibration errors systematically shift the entire data set obtained at one quadrupole mode. In case of the scattering parameter a, the statistical uncertainty of the fit is larger than the RF measurement uncertainty, while the energy gap Δ is independent of such systematic shifts. For a detailed discussion how measurement errors impact BCS fit parameters see [96].

After subtracting an RF field independent residual resistance of 23 nΩ and 73 nΩ for Q1 and Q2, respectively from measurement data, the temperature dependent BCS resistance is shown as a function of RF field in Fig. 5.4. At low fields of 10 mT and 20 mT the data perfectly matches the expectation of $B_{\mathrm{BCS}} \propto f^2$. Correspondingly, this excludes significant frequency specific, systematic errors of the RF measurement system. Towards higher RF field, the increase of R_{BCS} is suppressed at higher frequency. Note that systematic errors due to losses in the coaxial structure may affect the Q-slope behavior and also depend on frequency (see Section 3.3.2). Comparing the observed rise of R_{BCS} to the fit parameters in Figs. 5.3a and 5.3b, this can be consistently attributed to the scattering parameter a. The obtained Δ values are compatible with a mean of 1.87 meV that is independent of RF field and frequency. Such behavior agrees with empirical extensions of the BCS model of Eq. 4.1, introducing polynomial dependence of

a on the RF field in order to describe non-linear BCS effects and medium-field Q-slope [41]. Note that from literature a lower value of $\Delta = 1.5\,\text{meV}$ is expected [120].

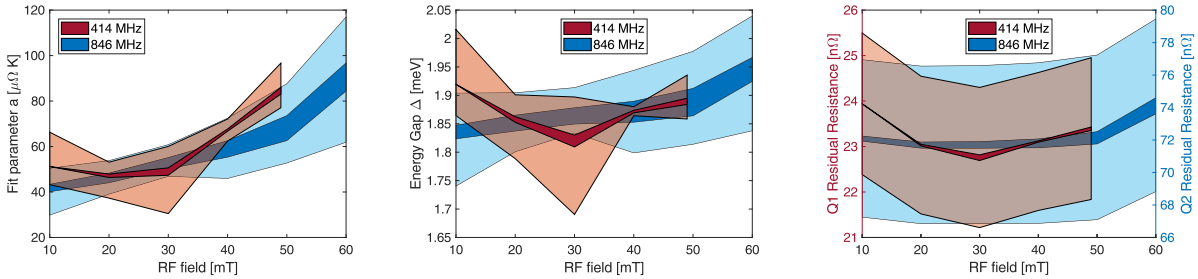

(a) *Scattering factor a* **(b)** *Energy gap* Δ **(c)** *Residual resistance* R_{res}

Figure 5.3: *Baseline BCS results obtained from fitting* $R_S(T)$ *curves for different values of RF field at frequencies of 414 and 846 MHz. Dark colored areas show the impact of whether or not taking into account data at 4.5 K* ($\approx T_c/2$)*. Semi-transparent areas give the fit uncertainty including the systematic RF measurement uncertainty.*

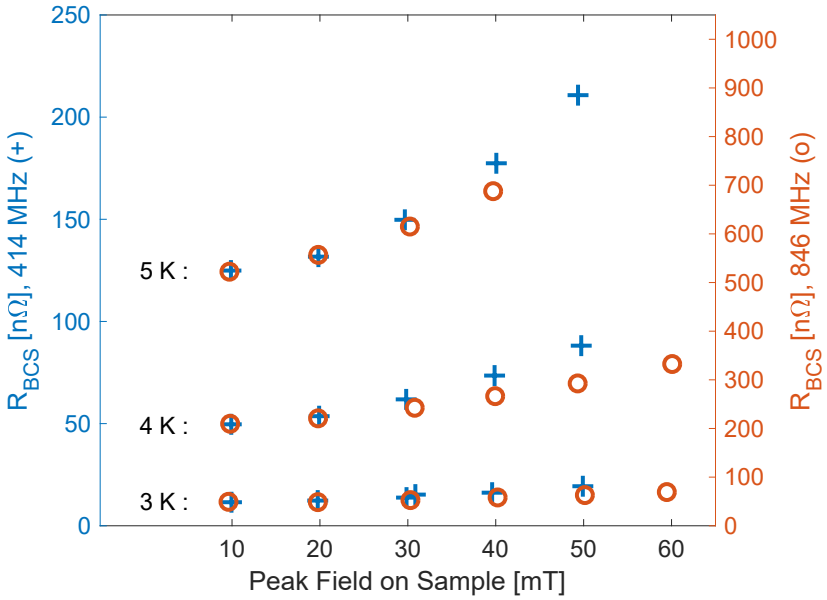

Figure 5.4: *Temperature dependent BCS surface resistance vs. RF field on sample for the baseline measurement. The values were calculated by subtracting an RF field independent residual resistance from measurement data of 23 nΩ and 73 nΩ for Q1 and Q2, respectively (see Fig. 5.3c). Note that the ordinates are linked quadratically by* $(846/414)^2 \approx 4.2$*, i.e. a quadratic frequency dependence would yield perfectly overlapping curves in this representation.*

5.2.2 NbTiN-AlN-Nb Sample and Comparison with Baseline Data

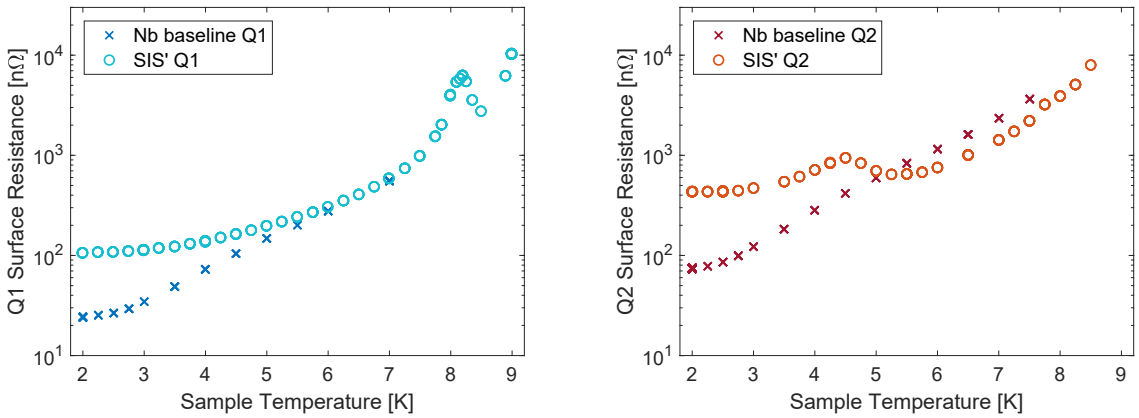

(a) Q1 *(b) Q2*

Figure 5.5: *Measured surface resistance vs. sample temperature for baseline and S-I-S′ measurement at QPR modes Q1 and Q2. All points were taken at $B_{RF} = 10\,mT$.*

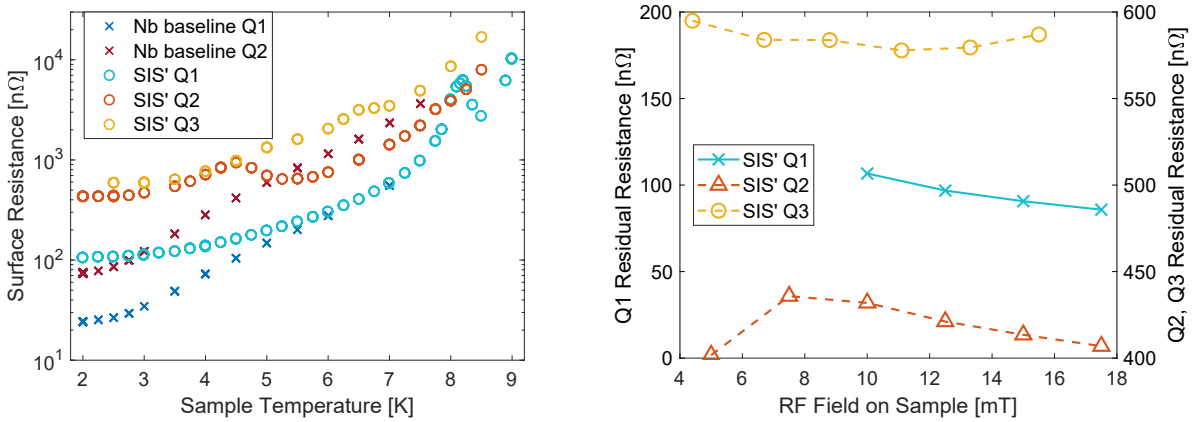

(a) Measured R_S *(b) Residual resistance*

Figure 5.6: *(a) Measured surface resistance vs. sample temperature for baseline and S-I-S′ measurement. Q3 data was taken at $B_{RF} = 8.8\,mT$. For clarity, data for Q1 and Q2 of Fig. 5.5 is shown again. (b) S-I-S′ temperature independent residual resistance as a function of RF field. The right-hand y-axis for data points at Q2 and Q3 is shifted but has the same scaling as the left-hand axis. For baseline R_{res} see Fig. 5.3c.*

Measurement data for surface resistance vs. sample temperature is shown in Figs. 5.5 and 5.6a for both, baseline and S-I-S′ sample. For clarity, Fig. 5.5 first gives the direct comparison of baseline and S-I-S′ measurement at similar frequency, i.e. identical RF mode of the QPR. Fig. 5.6a then allows to compare the surface resistance of the same sample at different frequencies. Note that all data points at the quadrupole modes Q1 and Q2 were taken at constant RF field of $B_{\mathrm{RF}} = 10\,\mathrm{mT}$, for Q3 $B_{\mathrm{RF}} = 8.8\,\mathrm{mT}$. For the S-I-S′ sample, $R_{\mathrm{S}}(T)$ curves at all three

frequencies show unexpected behavior that is both significant and reproducible. At Q1 and Q2 a region of non-monotonic dependence on temperature is observed, each featuring a distinct local maximum that differs in position and width. At Q1, comparable values of surface resistance are obtained at temperatures of 8.2 K and 8.9 K with an interjacent decrease of more than 50 %. For Q2 the maximum lies near 4.5 K with a following decrease of 300 nΩ (or 30 %) that is less pronounced than at Q1 but wider in temperature, spanning 1.9 K. For the third quadrupole mode less data points are available. However, a decrease spanning several Kelvin can be excluded while a change of slope is visible in between 6.5 K and 7 K. Note that an increasing contribution of the niobium substrate is expected at elevated temperatures since the S-I coatings do not cover the sidewalls of the sample chamber. However, this contribution is strictly monotonic in temperature and cannot explain the observed features (see baseline measurement results). In

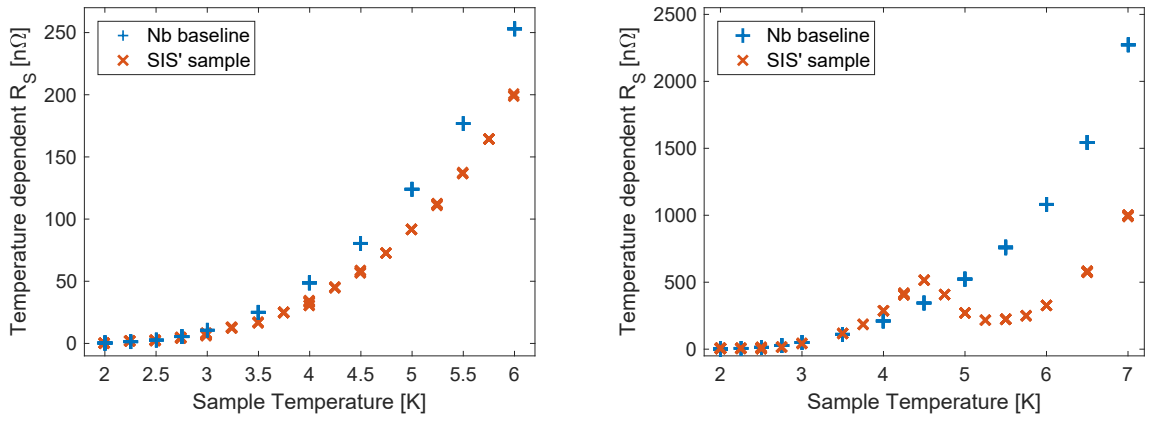

(a) Q1 *(b) Q2*

Figure 5.7: *Temperature dependent surface resistance vs. sample temperature for baseline and S-I-S′ measurement after subtraction of R_{res} according to Figs. 5.3c and 5.6b. All points were taken at $B_{RF} = 10\,mT$.*

the following, the partition of measured surface resistance into residual and BCS contribution for investigating $R_S(T)$ might be arguable. For that reason, the BCS approximation given by Eq. 4.1 is used only to extract a temperature independent residual resistance. This is justified due to the fact that for a certain low-temperature range, both RMSE and R_{res} values vary reasonably little when limiting the temperature range for the fit to $T_{max} \leq 5\,K$. Corresponding plots of the fit procedure can be found in the Appendix (see Figs. A.11–A.13), resulting values are shown in Fig. 5.6b. Compared to the baseline measurement, a strong increase of residual resistance is observed. However, the increase of surface resistance with temperature is suppressed, which is expected given the comparatively high T_c of NbTiN. At the first quadrupole mode, this becomes clearly visible after subtracting R_{res} from the measurement data (see Fig. 5.7a).

For Q2 the effect of non-monotonic $R_S(T)$ "overcompensates" the higher R_{res}, leading to a lower total surface resistance than for baseline niobium for $T \gtrsim 5.2\,K$. Subtracting R_{res} yields the

contradicting picture of higher temperature dependent surface resistance in the range of ~ 3.5 to 4.7 K than for bulk niobium (see Fig. 5.7b). This confirms the earlier statement that the observed non-monotonic behavior of $R_S(T)$ is more likely a consequence of a temperature range with enhanced surface resistance, i.e. a local maximum, than of a mechanism reducing R_S.

A mechanism of enhanced losses also fits to the visual impression of $R_S(T)$ at Q1 in the temperature range of 7.8 K to 8.5 K. At the peak, the measured R_S even exceeds the data obtained at 845 MHz (Q2). Furthermore, such a mechanism could explain the comparatively small change in surface resistance when increasing the frequency from Q2 to Q3 (see Fig. 5.6a): Continuing the trend of a peak in R_S at T_{pk}, and assuming that T_{pk} decreases with frequency might lead to $T_{pk} < 2.5$ K at Q3 (1286 MHz). Unfortunately, surface resistance measurements were impossible in this temperature range due to high RF heating. Hence, the value of $R_{res} = 584\,n\Omega$ could be affected significantly. Remember, so far we only investigated data measured at constant RF field of $B_{RF} = 10$ mT (8.8 mT in case of Q3).

The measured surface resistance as a function of RF field at Q1 and Q3 is given in Fig. 5.8. Again, significantly different behavior is observed when changing the frequency. At the second quadrupole mode, a detailed two-dimensional measurement data grid was possible, as shown in Fig. 5.9. Intersections of the black grid lines denote measured data points, the color representation is interpolated for better readability.

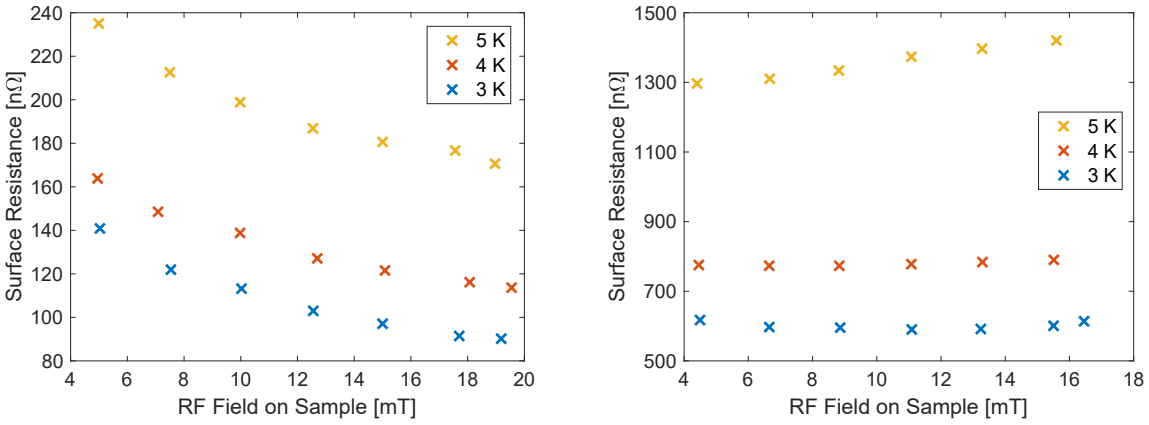

(a) Q1 *(b) Q3*

Figure 5.8: *Surface resistance vs. RF field on sample for the S-I-S′ sample. For comparison to the baseline measurement see Fig. 5.4.*

At Q1, the surface resistance consistently decreases towards higher field. At low temperatures of 3 and 4 K this effect is stronger than the increase of $R_S(T)$. This requires an RF field dependent residual resistance, as also visible in Fig. 5.6b. At Q2, a similar but quantitatively smaller decrease of surface resistance with RF field is restricted to field levels larger than 7.5 mT and temperatures below 3.5 K. Approaching the local peak in R_S at 4.5 K yields a surface resistance growing with field. For higher temperatures ($T \gtrsim 5$ K), R_S depends only slightly on field. For

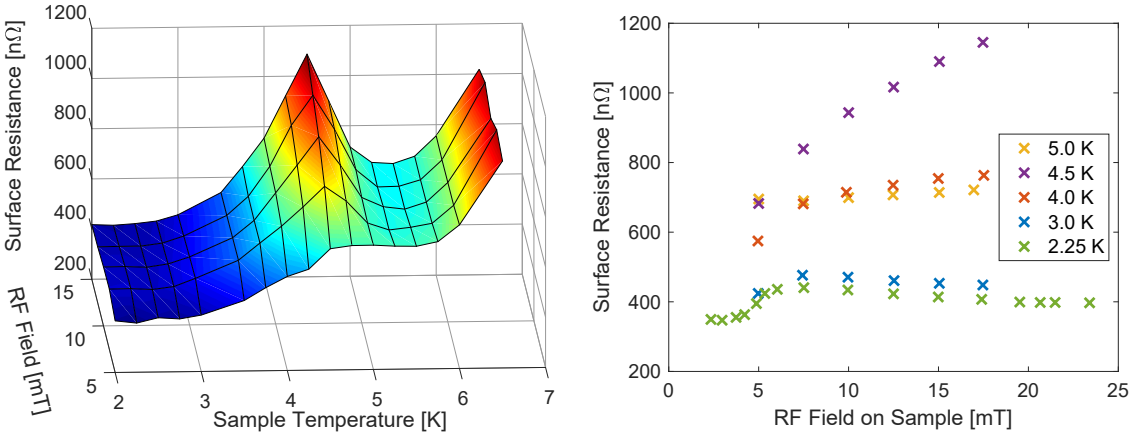

Figure 5.9: *Measured surface resistance vs. sample temperature and RF field strength at 845 MHz (Q2). Intersections of the black grid lines denote measured data points, colors are interpolated for better readability.*

Q3, the surface resistance also depends slightly on RF field with a tendency of increasing Q-slope towards higher temperature which is another indication for a comparatively low value of $T_{\mathrm{pk,Q3}}$ that was not accessible experimentally.

As for the curves of $R_{\mathrm{S}}(T)$, the behavior of $R_{\mathrm{S}}(B)$ changes at or near the characteristic temperature $T_{\mathrm{pk}}(f)$. This allows for a consistent description of the measured data for $R_{\mathrm{S}}(T, B)$ at all three frequencies: For $T \ll T_{\mathrm{pk}}$ the surface resistance decreases with field. Near T_{pk}, R_{S} increases with RF field, while it becomes nearly independent of the applied RF field strength for $T \gg T_{\mathrm{pk}}$. The value of T_{pk} itself decreases for higher frequency and denotes a distinct temperature range of enhanced surface resistance. Note that the cause of this behavior has to include RF field dependent residual resistance.

The physical reason for this behavior is still unclear. One possibility might be a coupling mechanism of the two superconducting layers similar to Josephson-junctions. In that case, the ratio of the insulator thickness ($d_{\mathrm{I}} = 15\,\mathrm{nm}$) to the superconducting coherence length would be important. For NbTiN the value of 3 leads to strong suppression of Cooper pair tunneling, while for niobium a ratio of only 0.4 is obtained. Theoretical models for Josephson-junctions and weak links that predict stepwise changes and non-monotonic behavior of the microwave surface resistance as a function of applied field or current [121, 122]. Looking at the surface resistance vs. temperature, non-monotonic behavior has been observed before on Y-Ba-Cu-O superconducting samples [123]. Literature exists stating that for high-T_{c} superconductors a non-monotonic behavior of $R_{\mathrm{S}}(T)$ showing a local maximum is often observed for high-quality samples below about $0.8\,T_{\mathrm{c}}$ [58]. However, in other measurements this local maximum disappeared for samples with smallest R_{S} [124, 125]. In any case, the theoretical model of [21] presented in Section 2.3 and used throughout this work adding up BCS dissipation of each superconducting layer based on the calculated current density is not sufficient to describe the measurement results.

5.3 Penetration Depth

In order to apply one of the penetration depth measurement techniques introduced in Section 3.6 to multilayer systems, a single-valued penetration depth has to be defined for use with Eq. 3.29. In analogy to the simple case of $B(x) \propto \exp(-x/\lambda)$ and $\lambda = \int_0^\infty \exp(-x/\lambda)\,\mathrm{d}x$, the effective value λ_{eff} is defined as

$$\lambda_{\mathrm{eff}}(T) = \frac{1}{B(T, x=0)} \int_0^\infty B(T, x)\,\mathrm{d}x. \tag{5.1}$$

$B(T, x)$ is calculated using the analytic expression of Eq. 2.35, with temperature dependence of the individual layers according to the Gorter-Casimir expression (Eq. 2.3). For simplicity, the integration is calculated numerically for x in the interval $[0\,\mu\mathrm{m}, 5\,\mu\mathrm{m}]$ with variable resolution of $\mathrm{d}x = 0.1\,\mathrm{nm}$ for $x \leq 500\,\mathrm{nm}$ and $\mathrm{d}x = 0.5\,\mathrm{nm}$ for $x > 500\,\mathrm{nm}$. When exceeding the critical temperature of a layer, λ_i is replaced by the normal conducting skin depth δ_{nc}. Normal state resistivities are taken from literature with $\sigma_{\mathrm{Nb,RT}} = 6.58 \cdot 10^6\,\mathrm{S/m}$ [126] and $\sigma_{\mathrm{NbTiN,cryo}} = 2.86 \cdot 10^6\,\mathrm{S/m}$ [16]. For niobium, the conductivity at cryogenic temperatures is obtained by multiplying σ_{RT} with the RRR value.

Ideally, the contribution of niobium can be described by T_{c} and $\lambda(0\,\mathrm{K})$ only, with the latter yielding both, RRR and δ_{nc}. However, depending on $T < T_{\mathrm{c,Nb}}$ or $T > T_{\mathrm{c,Nb}}$, a very different sample volume is probed by the RF field. Especially the substrate purity (RRR, ℓ) can change significantly, in this case one penetration depth consistently fitting the entire temperature range does not exist. Hence, $\mathrm{RRR_{sc}}$ for the superconducting state and the normal conducting δ_{nc} are fitted individually, allowing for a vertical change in purity of the niobium substrate. Subsequently, the bulk RRR is obtained from δ_{nc} assuming the normal skin effect according to $\delta_{\mathrm{nc}}^{-2} = \pi\mu_0 f \sigma_{\mathrm{RT}}\,\mathrm{RRR}$ with room-temperature conductivity σ_{RT}.

In order to reduce coupled uncertainties and the number of free parameters, the values of ξ_i and $\lambda_{\mathrm{L},i}$ for each (superconducting) layer are fixed. Furthermore, an iterative fit procedure is applied: The critical temperatures are determined in preliminary fit runs, in case of $T_{\mathrm{c,Nb}}$ the data range is restricted to $T < 9.25\,\mathrm{K}$. Subsequently, the parameters $\mathrm{RRR_{sc}}$, δ_{nc} and λ_0 are obtained using a global fit to the full temperature range of 4 K to 18 K. Measurement data for the S-I-S′ sample at all three quadrupole modes is shown in Fig. 5.10, corresponding fit results can be found in Tab. 5.1. The measurements were done using the VNA-based method as described in Section 3.6.2. Individual thermal cycles were carried out for the three quadrupole modes.

The critical temperature of the niobium substrate is found throughout all three frequencies to be in very good agreement with the expectation from literature of $T_{\mathrm{c,Nb}} = 9.25\,\mathrm{K}$ [120]. The superconducting $\mathrm{RRR_{sc}}$ – or more precisely its value for the uppermost $\approx 100\,\mathrm{nm}$ – scatters

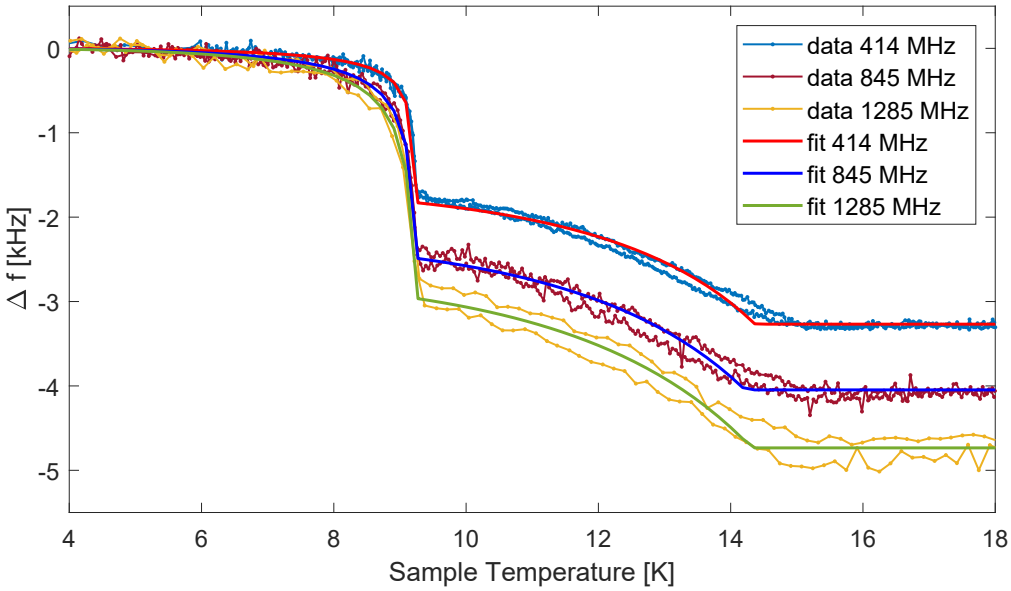

Figure 5.10: *Measured frequency shift vs. sample temperature for all three quadrupole modes. Fits using Eq. 5.1 are shown with solid lines, result data is given in Tab. 5.1.*

Table 5.1: *S-I-S′ penetration depth measurement. Error bars give statistical fit errors.*

	Frequency	414 MHz	845 MHz	1285 MHz
bulk Nb substrate	$T_{c,\,Nb}$	(9.26 ± 0.01) K	(9.28 ± 0.04) K	(9.29 ± 0.08) K
	$\lambda(0\,K)$	(46.2 ± 2.1) nm	(50.4 ± 2.1) nm	(44.2 ± 3.9) nm
	δ_{nc}	(515.4 ± 3.5) nm	(377.8 ± 2.9) nm	(298.9 ± 5.5) nm
	λ_L		32 nm (fixed)	[29]
	ξ_0		39 nm (fixed)	[29]
	RRR_{sc}	20.9 ± 3.6	15.3 ± 2.1	25.2 ± 9.6
	RRR_{nc}	350 ± 5	319 ± 5	335 ± 12
NbTiN layer	$T_{c,\,NbTiN}$	(14.37 ± 0.03) K	(14.22 ± 0.05) K	(14.32 ± 0.13) K
	$\lambda(0\,K)$	(245.5 ± 2.1) nm	(248.2 ± 2.7) nm	(236.6 ± 6.0) nm
	δ_{nc}	14.63 µm	10.24 µm	8.30 µm
	ξ_0		5 nm (fixed)	[16]
	κ	49.1 ± 0.4	49.6 ± 0.5	47.3 ± 1.2

strongly but the weighted average of $RRR_{sc} = 17 \pm 2$ is consistent within the statistical fit uncertainty for all three values. Note that in the superconducting state the penetration depth should be independent on frequency. The observed scatter together with the absolute values can be interpreted as an indication for compositional inhomogeneities, since the RF field distribution on the sample surface is similar but not identical for the different quadrupole modes. In contrast to that, RRR_{nc} has no clear dependence on frequency, even though being obtained from significantly different depths x of the probed sample volume. Hence, for $x \gtrsim 200$ nm, i.e. below the region of sc RF currents, the niobium substrate is found to be homogeneous and

of high purity. This is consistent with the nominal RRR of $\gtrsim 300$ from the used sheet material. While not being visible in the SEM cross section (see Fig. 5.2), part of the deposited coating could be diffused into the RF layer of the substrate, explaining the comparatively low values of $\mathrm{RRR}_{\mathrm{sc}}$.

For reference, the results of the penetration depth measurement for the niobium substrate, obtained during baseline measurement prior to coating, are given in the Appendix (see Section A.7). Note that these RRR values – even though also being significantly lower than 300 – can hardly be compared with the ones discussed here. In case of bulk niobium surface oxides and impurities are known to reduce the RRR of the surface, i.e. the volume of RF currents probed by this measurement technique [127]. However for the coated sample, the surface was cleaned by EP prior to the coating, removing about 100 µm. Furthermore, the natural oxide layer of the niobium was removed by an UHV bakeout in the deposition chamber.

For the NbTiN top layer very consistent results are obtained for all three frequencies. The result of $\lambda(0\,\mathrm{K}) \approx 246\,\mathrm{nm}$ is higher than literature values of 150 nm to 200 nm [16] but can be explained by a reduced mean free path due to the film deposition technique. The observed critical temperature of about 14.3 K is significantly lower than the expected value of $T_{\mathrm{c}} = 17.3\,\mathrm{K}$ [16]. This indicates issues of the coating that might be a reason for the very high residual resistance compared to the baseline measurement, or the small critical field as discussed in the following section.

5.4 RF Critical Field

The RF quench field of the bulk niobium substrate was obtained in the baseline measurement using the single pulse technique as described in Section 3.5 at 414 and 846 MHz. Experimental data is shown in Fig. 5.11 together with quadratic fits according to Eq. 3.17. The temperature range used for fitting is shown by solid lines, dashed lines indicate the extrapolation to 0 K. Quantitative fit results are given in Tab. 5.2. The weighted average of $B_{0,\mathrm{Nb}} = (240 \pm 15)\,\mathrm{mT}$ is in very good agreement with the expected superheating limit for niobium $B_{\mathrm{sh}} = 240\,\mathrm{mT}$ [8]. However, a strictly quadratic dependence on temperature is observed only at high temperatures, the sample could exhibit reduced quench fields at lower temperature. Unfortunately, the QPR quench limit ruled out further measurements in that range. For the S-I-S′ sample, first hints for

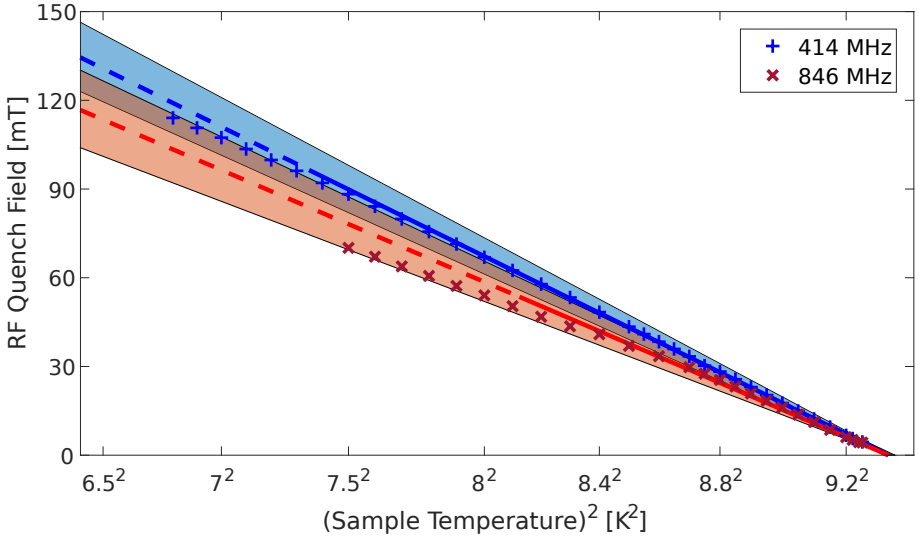

Figure 5.11: *Baseline RF quench field of the bulk Nb substrate. Semi-transparent areas give the total fit uncertainty, which is dominated by the systematic uncertainty of the RF system. Fit parameters are given in Tab. 5.2.*

a low RF quench field were observed during surface resistance measurements: The measured R_{S} jumped up suddenly when exceeding a field level of about 20 mT. This behavior consistently occurred for CW and pulsed RF power, indicating both, good thermal connection to the substrate and a "magnetic" origin of the quench. Thermal runaway – even accelerated by observed the Q-slope – can be excluded: Given by the long thermal path of the QPR sample chamber, a typical sample can be operated "on the edge" where such a runaway occurs. Increasing the RF field by few µT triggers a "slow" runaway that takes several seconds for a temperature rise of the order of Kelvins. Much higher fields, of course, will lead to fast thermal quenches that can not be resolved in time domain by eye. However, for this sample, very stable sample temperature – and R_{S} data – was obtained close to the quench point with instantaneous jumps of several Kelvin (or µΩ) when slightly increasing the RF field.

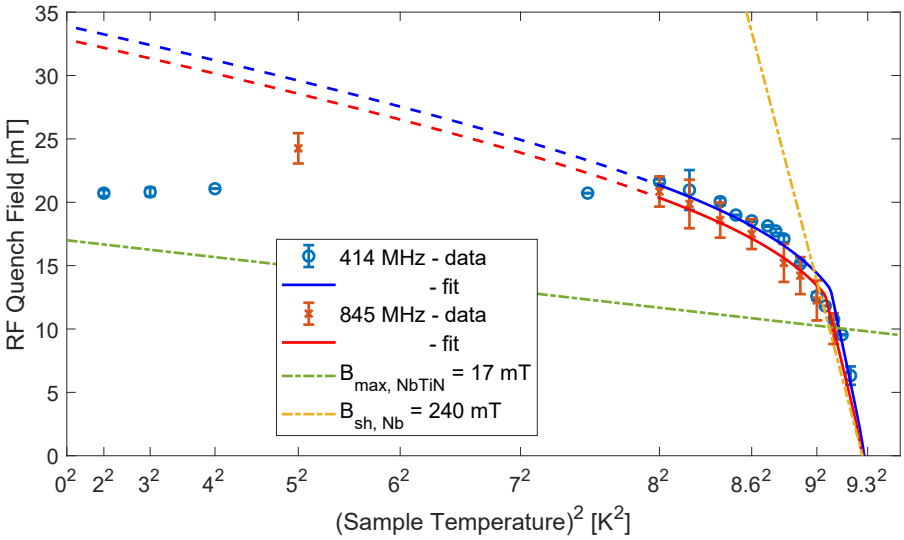

Figure 5.12: *RF quench field of the S-I-S′ sample, measured at 414 and 845 MHz. Fit parameters are given in Tab. 5.2. The error bars give statistical uncertainty and reproducibility only, 6.5 % of relative systematic RF uncertainty has to be added.*

Table 5.2: *Fit results of the critical field measurements for the bulk Nb substrate (baseline) and the S-I-S′ sample. The systematic error on B_0 is defined by the uncertainty of the RF system. Note that this also impacts T_c in the non-linear S-I-S′ fit.*

	Frequency	$B_{0,\mathrm{Nb}}$ [mT]	$T_{\mathrm{c,Nb}}$ [K]
Nb baseline	414 MHz	254 ± 3 (stat.) ± 17 (sys.)	9.33 ± 0.01
	846 MHz	220 ± 10 (stat.) ± 14 (sys.)	9.34 ± 0.01

	Frequency	$B_{0,\mathrm{NbTiN}}$ [mT]	$T_{\mathrm{c,Nb}}$ [K]
S-I-S′ sample	414 MHz	17.2 ± 0.8 (stat.) ± 1.1 (sys.)	9.28 ± 0.02 (stat.) ± 0.01 (sys.)
	845 MHz	17.0 ± 0.6 (stat.) ± 1.1 (sys.)	9.27 ± 0.03 (stat.) ± 0.01 (sys.)

For quantitative investigation of the RF quench field, the single pulse technique was applied again at 414 MHz and 845 MHz. Measurement data is shown in Fig. 5.12. Non-linear fits use the expression of Eq. 2.41, including the temperature dependencies of λ_i and $B_{\mathrm{sh},i}$ for each layer. For simplicity, the empirical quadratic dependence on temperature of Eq. 3.17 is used for $B_{\mathrm{sh},i}$. Resulting fit parameters are given in Tab. 5.2. The temperature axis of Fig. 5.12 is scaled quadratically to improve readability at high temperature. Note that for S-I-S′ structures non-linear behavior is expected in this representation.

The data confirms an RF quench field in the range of 20 mT to 25 mT which is even below the lower critical field of $H_{\mathrm{c1,NbTiN}} = 30\,\mathrm{mT}$ [16]. Measurements at 414 MHz and 845 MHz are consistent within the measurement uncertainty. Fits according to Eq. 2.41 are shown by solid lines and extrapolated to low temperature as indicated with dashed lines. Near 9.1 K the transition of the quenching top layer ($T < 9.1\,\mathrm{K}$) to the quenching substrate ($T > 9.1\,\mathrm{K}$) is

visible. Below 8 K the observed RF quench field does not depend on temperature as expected but stays nearly constant. This is interpreted as additional non-fundamental quench limitation, possibly due to local defects with early vortex penetration.

The fitted temperature range contains only few data points on each curve. In order to prevent overfitting with unphysical results, only $T_{c,Nb}$ and $B_{0,NbTiN}$ are fitted, all other parameters were fixed to the results of the penetration depth measurement (see Tab. 5.1). The RF field limit for the niobium substrate is taken from the baseline measurement. For the NbTiN layer a low-temperature quench field of $B_{0,NbTiN} \approx 17\,\mathrm{mT}$ is obtained at both frequencies. This is about half of $H_{c1,NbTiN}$ and far below the expected superheating limit of $H_{sh,NbTiN} \approx 440\,\mathrm{mT}$ [75]. Coating flaws as already suspected from the high residual surface resistance and the low critical temperature would also explain these values as well as early vortex penetration.

The DC magnetic field of first vortex penetration was measured for a witness sample that was coated together with the QPR sample [116]. The result of $B_{vp} = 15-20\,\mathrm{mT}$ is very close to the observed RF quench field but far less than expected for such film thickness. A witness sample prepared under comparable conditions with slightly increased thicknesses of 80 nm NbTiN and 20 nm AlN showed $B_{vp} = 160\,\mathrm{mT}$ [116]. Further measurements on the coating characteristics are ongoing.

The discussion of pre-quench RF heating led to the conclusion that a short quench time, i.e. high forward power, is preferred (see Section 3.5.2). In contrast to this, the applied forward power had to be limited to few Watts for this sample. Otherwise, pulse traces as shown in Fig. 5.13 were obtained, yielding systematically overestimated values of the quench field.

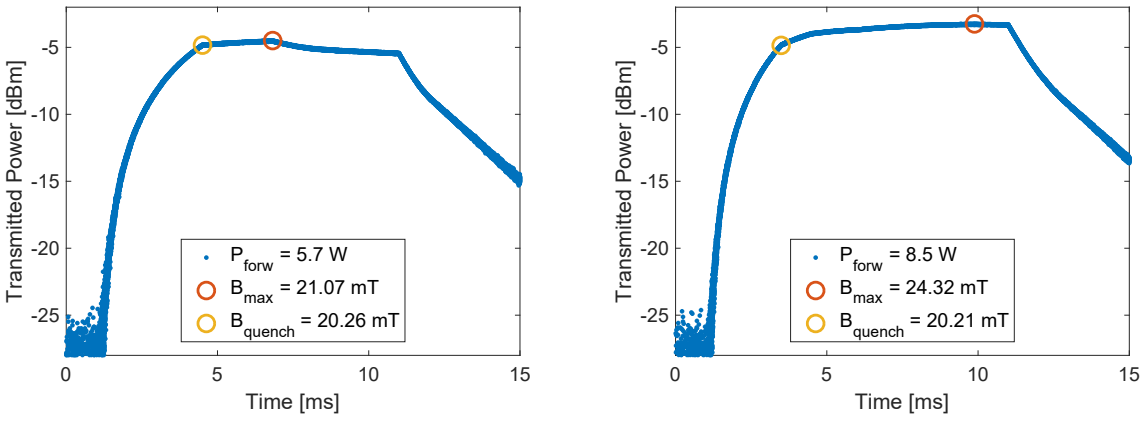

(a) $P_{forward} = 5.7\,W$ **(b)** $P_{forward} = 8.5\,W$

Figure 5.13: *Typical pulse traces showing post-quench field rise in case of too high forward power. Data was taken at 414 MHz and 4 K sample temperature.*

The single-pulse method relies on a sudden decrease of the RF field level (i.e. transmitted RF power) at the very instant of a quench. For that, a sudden and distinct drop of Q_{L} or change in penetration depth (i.e. resonant frequency) is required. On a quench of the thin superconducting top layer, these effects are not large enough, hence the PLL system keeps lock and the RF field level continues to rise. Then, the only consequence of a quench is a change of rise time, visible as salient point in the pulse trace (see Fig. 5.13). Reduced forward power enhances the impact of a quench on the pulse trace. For this sample, the applied forward power was limited to maximum 6 W at temperatures up to 8 K and both RF modes. At higher temperatures, the increasing surface resistance of the sample reduced Q_{L} of the QPR – and hence the input coupling – leading to a slightly relaxed power limit of $P_{\mathrm{forward}} \leq 10\,\mathrm{W}$. Note that from the discussion of CW quench behavior being very similar to the case of pulsed RF power (see beginning of this section), RF heating due to the immanently prolonged quench time at lower forward power is not considered to be an issue.

5.5 Summary

In summary, a first successful measurement campaign of an S-I-S′ sample using a quadrupole resonator together with quantitative analysis using recent theoretical methods is reported. Surface resistance data is available at frequencies of 414, 845 and 1286 MHz, in the temperature range of 2 K to 9 K. The RF quench limit restricted measurements to $B_{\mathrm{RF}} \lesssim 23\,\mathrm{mT}$. $R_{\mathrm{S}}(T)$ data at Q1 and Q2 shows non-monotonic behavior with local maxima at $T_{\mathrm{pk,Q1}} = 8.2\,\mathrm{K}$ and $T_{\mathrm{pk,Q2}} = 4.5\,\mathrm{K}$. Near this characteristic temperature the dependence of R_{S} on the RF field changes as well. For $T \ll T_{\mathrm{pk}}$, total and residual surface resistances decrease towards higher field; while at T_{pk} a strong increase of R_{S} with field is observed.

Earlier RF measurements of bulk NbTiN at 4 GHz [128] or in S-I-S′ configuration at 7.4 GHz [129, 130] indicated the potential of NbTiN for SRF applications by showing lower surface resistance than for bulk niobium at elevated temperatures $\gtrsim 4.2\,\mathrm{K}$. With the sample studied in this work, a reduction of temperature dependent surface resistance compared to the baseline test is shown, at 845 MHz and temperatures above 5 K even the total surface resistance is smaller than before. However, significant non-monotonic behavior of $R_{\mathrm{S}}(T)$ is observed that changes with frequency and also impacts the dependence of the surface resistance on RF field. Up to now, theoretical models of the surface resistance in S-I-S′ structures sum up the Joule heating of each layer independently, which does not predict any non-monotonic behavior. Further studies on the role of the insulating layer and on possible coupling effects are ongoing.

The performance of the coatings on this specific sample is very likely limited by non-fundamental issues: The observed critical temperature of $T_{\mathrm{c,NbTiN}} \approx 14.3\,\mathrm{K}$ is significantly lower than expected and R_{res} is clearly higher than for the niobium baseline measurement. The temperature-independent RF quench field for $T < 8\,\mathrm{K}$ indicates early vortex penetration, which occurs preferentially at weakly superconducting locations, e.g. at defects or spots of incorrect composition. In that case, single or few quench spots limit the global performance while the surface averaging penetration depth measurement is far less sensitive to small-sized effects. However, for temperatures above 8 K non-quadratic behavior as predicted by multilayer models is observed. The frequency shift measurement is also consistent with the S-I-S′ theory yielding a value of the penetration depth that is close to the ones available in literature. This gives confidence in the theoretical models describing the magnetic field profile and the current densities in the superconducting layers.

6 Summary and Outlook

6.1 Performance of the Quadrupole Resonator

Within the scope of this thesis, the QPR at HZB advanced from the commissioning phase to a state, where routine testing of samples is possible. The high performance in surface resistance measurements at low frequency was already demonstrated early on [80], while for higher harmonic modes significant work on the RF system was needed. The measurement capabilities were continuously expanded beyond the surface resistance, enabling RF characterization of samples with respect to quench field, penetration depth and critical temperature. From those directly measured values, quantities such as DC critical fields, mean free path, RRR and the Ginzburg-Landau parameter can be derived. Low-power measurements above T_c provide access to the bulk RRR and the normal state resistivity.

Studying the capabilities of the QPR revealed important practical and theoretical limitations. The most important practical limitation is set by parasitic RF losses on parts of the calorimetry chamber other than on the sample surface of interest. Especially at higher harmonic frequencies this prevents surface resistance measurements in the low nΩ range, which in fact is required if fundamental limits of superconductors and possible alternative materials to niobium are investigated. Hence, the findings of this work can be used to path the way towards a significant evolution of a next-generation Quadrupole Resonator. Main aspects are:

Improved damping of RF fields penetrating the coaxial structure. Reducing parasitic losses on the sample chamber assembly is crucial to achieve high accuracy surface resistance measurements without systematic bias effects. Analytical calculations show that changing the radial dimensions of the coaxial structure does not significantly change the damping coefficient [81]. Extending the sample chamber vertically only improves losses on the bottom flange but not on the sidewalls of the calorimetry chamber. This is especially relevant since thin film coatings typically cover the sample surface and minor parts of the sidewalls only. In the development of high-gradient CW cavities, e.g. for ERLs, absorbing materials have been studied that are compatible to SRF environments. Including lossy material in the coaxial structure that is not in contact with the thermal system of the calorimetry chamber could suppress RF fields significantly and hence sources of parasitic heating and systematic errors.

Reducing the susceptibility of the QPR to microphonics and environmental pressure changes. Work on the microphonics spectrum of the QPR showed that pendulum movements of the rods are the most important contribution [80, 85]. If the rods may not be shortened – in order not to lose the low frequency operation at 420 MHz – damping concepts successfully applied to quarterwave cavities such as passive dampers can be downscaled to meet the dimensions of the QPR. The wall thickness of the rods should only be increased with care since reduced cooling by LHe limits the performance at high-fields or CW RF power. Furthermore, the field distribution along the rods changes significantly at higher harmonic frequencies which has to be taken into account. Unfortunately, niobium coatings on copper are still limited to quench fields below that of high-RRR niobium, which otherwise would be ideal for high-field regions of the screening cavity. The frequency shift due to changes in environmental pressure might be reduced significantly by external reinforcement of the cylindrical cavity.

Stabilizing pulsed performance of the RF system at high fields. High-field measurements of surface resistance and critical field have to be done with pulsed power for several reasons. In this case Lorentz-Force detuning was identified to be a limiting issue for PLL operation. Dynamic detuning during the pulse rise time potentially triggers microphonics and mode cross talk. When reducing the susceptibility to microphonics – which is mainly an issue for the quadrupole rods – mechanical reinforcement likewise reduces the LF detuning coefficient. As an alternative approach or to suppress remaining LF detuning, active feed-forward compensation can be applied to the signal generator making use of the deterministic behavior of LF detuning. In contrast to accelerating cavities where operation at fixed frequency requires mechanical compensation [131], the excitation frequency would be adjusted such that the QPR is continuously driven at its resonant frequency.

Extending the capabilities of the QPR to DC magnetic fields. So far, the study of magnetic flux trapping in the sample is complicated by the fact that an external magnetic field cannot be applied easily, as it is shielded by the superconducting host cavity. The concepts of calorimetric RF-DC compensation and thermal decoupling from the screening cavity can be exploited much further. Since RF losses inside the cavity, especially its Q_0, are irrelevant, a fully superconducting cavity is not essential. Up to now, DC magnetic fields that are parallel to the RF surface of the sample and of comparable amplitude as in the case of vertically tested accelerating cavities are hardly possible, given by the screening effects of the pole shoes very close to the RF sample surface [80]. This screening distorts any applied DC magnetic field. Including parts of non-magnetic, normal conducting material (e.g. copper) opens the possibility to apply externally generated DC magnetic fields to the sample surface. Since thermal cycling of the sample chamber takes several tens of minutes (as compared to several hours for the entire cavity), this enables systematic and extended studies of flux trapping with high surface resistance resolution.

Tuning the RF field profile on the sample. The measurements of the Nb_3Sn sample shed light on the practical limitations of surface resistance measurements: At low field and high sample temperature, the change in heater power due to RF dissipation is low, leading to increased uncertainty. To improve this situation, the reference heater power has to be smaller which can be realized by increasing the integral thermal resistance from the sample surface to the liquid helium bath. The same effect is obtained by increasing the RF dissipation on the sample, i.e. by enlarging the surface fraction illuminated with high RF field. However, both would severely impact the high-field limitation. As also seen with the Nb_3Sn sample, surface resistance measurements are limited by RF heating when increasing the field level. Hence it is beneficial to reduce the sample area that is illuminated with RF field. Ideally, the field is constant in that area and close to zero outside, likewise eliminating all systematic Q-slope distortion. Admittedly, this would reduce the theoretical resolution and low-field performance of the QPR, but enhances the accessible field range significantly. Otherwise, measurements with $T \leq 2.0\,\mathrm{K}$ and $B_{\mathrm{RF}} \geq 40\,\mathrm{mT}$ at the same time are restricted to high-performance samples of $R_{\mathrm{S}} \leq 10\,\mathrm{n\Omega}$ or short-pulse operation.

6.2 Nb_3Sn Coatings

Nb_3Sn is currently the most promising alternative material to niobium for SRF cavities. Within this work a sample prepared by the same coating process as used for single-cell accelerating cavities was characterized. Penetration depth, electron mean free path and critical temperature are in good agreement with values in literature and obtained in cavity measurements. The critical temperature is also confirmed by the RF quench field measurement. In summary, this indicates consistent bulk properties of the Nb_3Sn film, since the frequency shift measurement gives an average over the RF penetration volume without being sensitive to localized irregularities.

Surface resistance data is available up to 10 K and 70 mT with a resulting energy gap from BCS fits that is consistent with literature but lower than expected for stoichiometric composition. At high temperatures, anti Q-slope behavior similar to N-doped niobium cavities is observed while the low-temperature performance is limited by notable residual resistance. Furthermore the residual resistance exhibits strong scaling with frequency of $f^{2.7}$ to $f^{3.0}$.

Measurement data of the RF quench field clearly exceeds H_{c1} but is limited significantly below H_{sh}. The temperature dependence of the RF quench field is described better by the vortex line nucleation model than by the quadratic behavior as expected from the thermodynamic critical field, indicating a non-fundamental limitation. The RF data and deviations from expected or ideal behavior can be explained by results from the SEM analysis performed after the QPR measurements: The sample surface clearly shows patchy regions of systematically reduced tin content, leading to smaller values for critical temperature and energy gap. This is consistent

with other studies of such structures showing insufficient film thickness to screen all relevant RF currents. White spots also visible in the SEM data with increased roughness and weakly linked grains potentially contribute to increased RF losses and lead to early flux penetration, i.e. reduced RF quench fields. Advanced coating procedures that focus on the initial nucleation phase of tin provide promising ways to continue Nb_3Sn sample studies.

6.3 Multilayer Structures

The RF characterization of (multi-)layered structures of superconductors and the interplay with intermediate insulators just started. The measurements on a system of NbTiN-AlN-Nb conducted during this thesis were the first using a Quadrupole Resonator with its capabilities of studying several frequencies and a wide parameter space of RF field and temperature.

The penetration depth measurement shows two distinct superconducting transitions and a shift of resonant frequency that is consistent with recently developed theoretical models. Also the extracted value of the penetration depth is close to the ones available in literature. However, the RF quench behavior is limited to an unexpected low value that is independent of temperature for $T < 8\,\mathrm{K}$. This indicates a non-fundamental limitation, possibly due to local defects in the coating. For temperatures above 8 K non-quadratic behavior as predicted by multilayer models is observed. Together with the penetration depth data this gives confidence in the theoretical models describing the magnetic field profile and current densities in the superconducting layers.

The surface resistance was measured at three frequencies as a function of temperature and RF field. Reduced temperature dependent R_S as compared to the baseline test is shown at elevated temperatures, at Q2 even the total surface resistance is smaller than before. This confirms earlier RF measurements on NbTiN indicating the possibility to achieve an SRF performance beyond the limits of niobium. However, significant non-monotonic $R_\mathrm{S}(T)$ is observed at temperatures that depend on frequency and which also impacts the behavior of $R_\mathrm{S}(B)$. This is in contradiction with simple models of S-I-S′ surface resistance summing up BCS losses of individual superconducting layers. Studying the question whether this behavior is intrinsic for NbTiN similar to the R_S of YBCO or connected to the S-I-S′ structures due to a coupling as in Josephson-junctions is a promising path for continuing the work of this thesis.

A Appendix

A.1 QPR Mode Scans

The mounting position of the sample chamber, i.e. the gap between RF sample and QPR pole shoes, strongly influences the resonant frequencies of RF modes. In the following some measurement examples are shown, depicting rather extreme conditions:

- run #001: Smallest gap observed so far, leading to high-frequency quadrupole modes
- run #011: "Typical" gap, Q3 is very close to the mode at 1287 MHz
- run #012: Increased gap and low Q# frequencies after several steps of surface chemistry

Figs. A.1–A.3 show VNA scans covering the first three quadrupole modes and neighboring cavity modes. Note that increasing the gap height shifts some non-quadrupole modes to higher frequency.

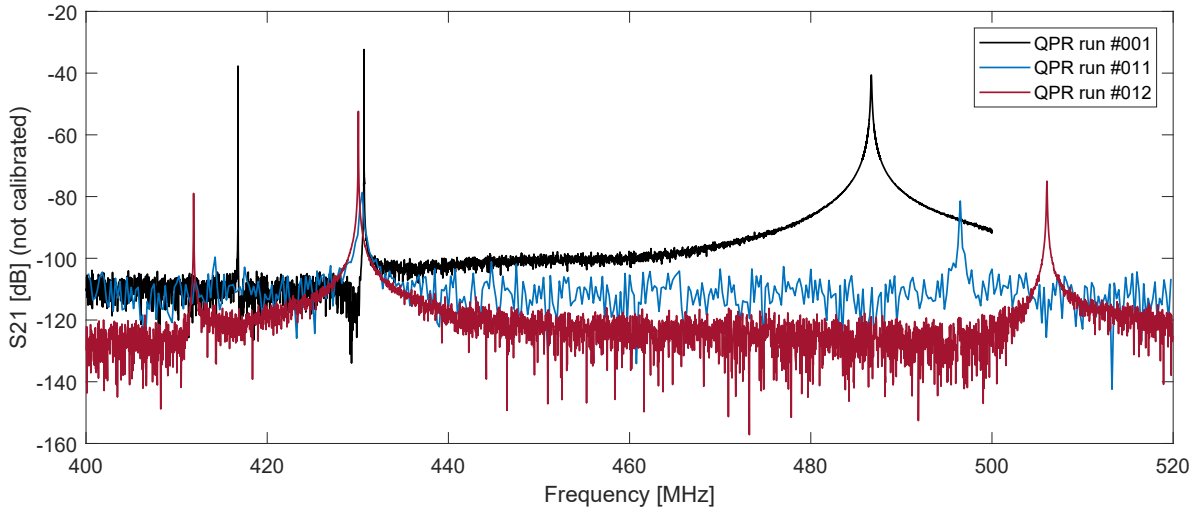

Figure A.1: *VNA mode scans 400 MHz to 520 MHz.*

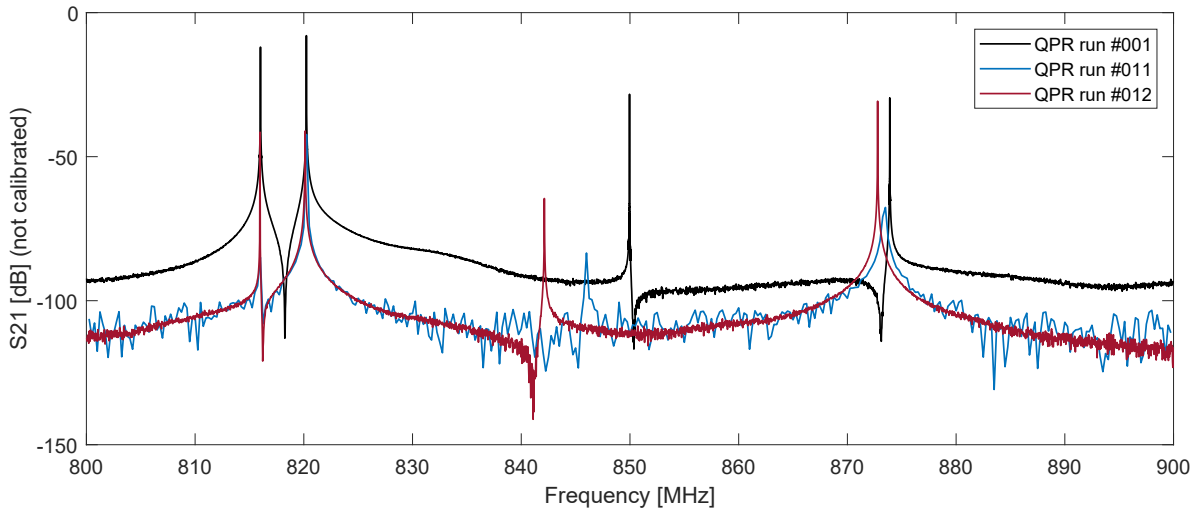

Figure A.2: *VNA mode scans 800 MHz to 900 MHz.*

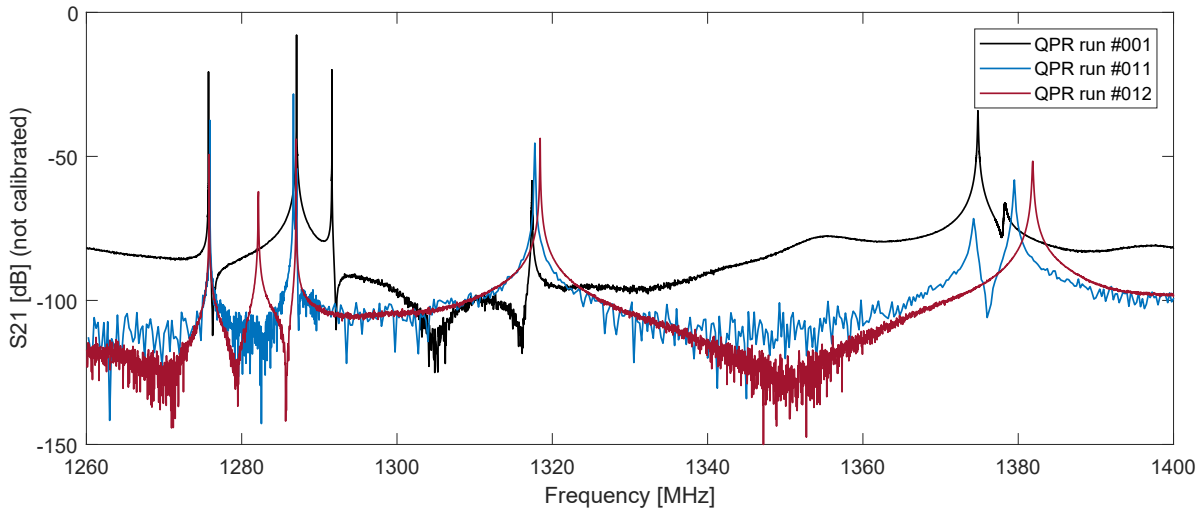

Figure A.3: *VNA mode scans 1.26 GHz to 1.40 GHz.*

A.2 Antenna Coupling

As addendum to Section 3.2.1, Figs. A.4 and A.5 show the external quality factor of initial and new loop coupler for the first 17 modes of the QPR (up to 1.33 GHz). For commissioning, the new pickup coupler was mounted on port "A" while keeping both initial couplers on "B". For technical details on the simulation see Appendix Section A.8.

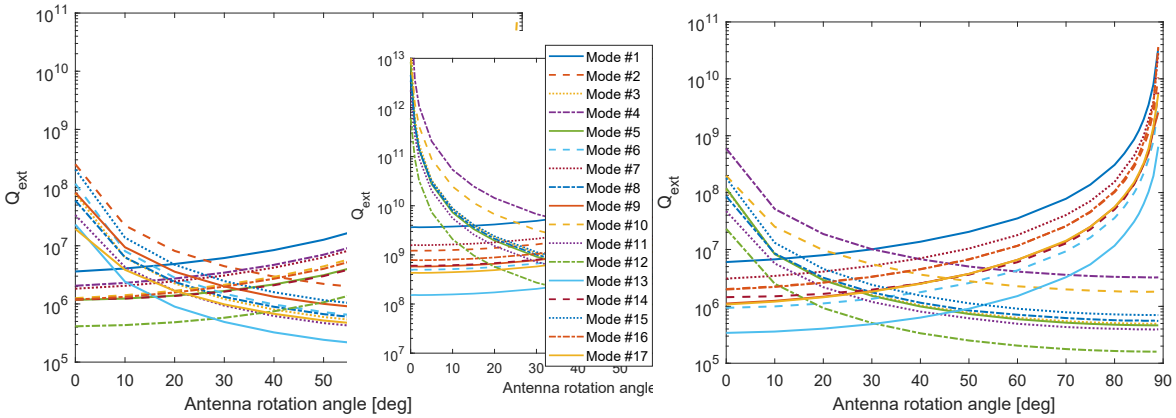

(a) Position "A" *(b) Position "B"*

Figure A.4: *Q_{ext} of the initial loop coupler for the first 17 modes (up to 1.33 GHz).*

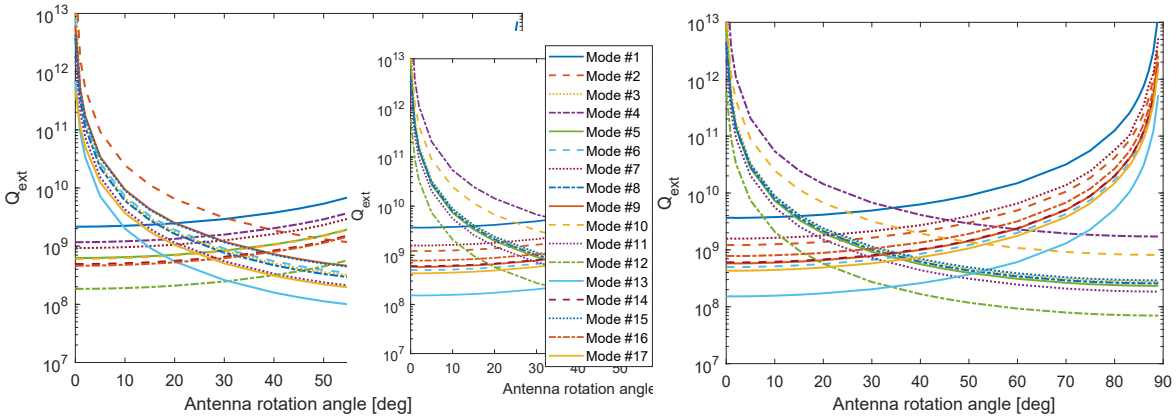

(a) Position "A" *(b) Position "B"*

Figure A.5: *Q_{ext} of the new loop coupler for the first 17 modes (up to 1.33 GHz).*

A.3 RF Gap Calibration

During commissioning of the QPR, R. Kleindienst measured and simulated the dependence of the first quadrupole mode frequency (Q1) on the gap height between sample surface and QPR pole shoes. Based on this cross-calibration, analytic expressions were developed that provide the necessary RF calibration constants for all three QPR modes.

The deviation Δg from the nominal gap distance of $g_0 = 500\,\mu\text{m}$ is given by

$$\Delta g = \frac{418.3\,\text{MHz} - f_{\text{Q1}}}{0.95} \cdot 100\,\mu\text{m} - 75\,\mu\text{m}. \tag{A.1}$$

RF calibration constants are obtained using polynomial fits with values of Δg in mm:

Q1:

$$\begin{aligned} c_1\left[\tfrac{1}{\text{m}^2}\right] &= 1318.5 - 344\,\Delta g + 204\,(\Delta g)^2 \\ c_2\left[\tfrac{\text{T}^2}{\text{J}}\right] &= 0.14827 - 0.1355\,\Delta g + 0.088\,(\Delta g)^2 \\ G\,[\Omega] &= 74.89 + 46.69\,\Delta g \end{aligned} \tag{A.2}$$

Q2:

$$\begin{aligned} c_1\left[\tfrac{1}{\text{m}^2}\right] &= 1399 - 364\,\Delta g + 209\,(\Delta g)^2 \\ c_2\left[\tfrac{\text{T}^2}{\text{J}}\right] &= 0.1394 - 0.137\,\Delta g + 0.088\,(\Delta g)^2 \\ G\,[\Omega] &= 170.94 + 125\,\Delta g \end{aligned} \tag{A.3}$$

Q3:

$$\begin{aligned} c_1\left[\tfrac{1}{\text{m}^2}\right] &= 1542.9 - 403\,\Delta g + 229\,(\Delta g)^2 \\ c_2\left[\tfrac{\text{T}^2}{\text{J}}\right] &= 0.1577 - 0.171\,\Delta g + 0.112\,(\Delta g)^2 \\ G\,[\Omega] &= 252.94 + 217.8\,\Delta g \end{aligned} \tag{A.4}$$

with

$$c_1 = \frac{B^2_{\text{sample, pk}}}{\int_{\text{sample}} |B|^2 \text{d}S} \qquad c_2 = \frac{B^2_{\text{sample, pk}}}{U} \qquad G = \frac{\omega\mu_0 \int_V |H|^2\,\text{d}V}{\int_{\text{sample}} |H|^2\,\text{d}S} = \frac{\langle R_{\text{S}}\rangle\,\omega U}{P_{\text{sample}}}$$

f_{Q1} has to be measured at room temperature with equal pressure conditions inside and outside the QPR. Simulated values are available for gap distances of $g = 0.50 \ldots 0.95\,\text{mm}$, this is equivalent to frequencies of $f_{\text{Q1}} = 417.59 \ldots 413.31\,\text{MHz}$. Outside of this range, the equations given above yield extrapolated results with unknown accuracy.

A.4 Systematic Errors due to RF Field Dependent Surface Resistance

The effect of a systematic error in surface resistance (or quality factor) measurements due to non-linear field-dependent R_S is not unique to the QPR. In general, SRF cavity measurements rely on a surface average similar to Eq. 3.16. Recently, a mathematical method was published that is capable of correcting this effect without knowing the actual non-linearity of the surface resistance a priori [98]. From the known RF field profile on the sample surface (or the cavity wall), a distribution function $a(h)$ is computed, denoting the fractional surface area that is exposed to an RF field $|H| \leq hH_{\mathrm{pk}}$ with $h \in [0;1]$ and peak field H_{pk}. Fig. A.6 shows $a(h)$ for the first three quadrupole modes. The fact that $a_{\mathrm{Q3}} \geq a_{\mathrm{Q2}} \geq a_{\mathrm{Q1}}, \forall h$ indicates stronger focusing of the RF field to the high-field region at higher frequency. In order to compensate field-dependent bias in R_S measurement data, correction coefficients $\beta(\alpha)$ are computed that transform an interpolation of measurement data

$$R_S\left(\frac{H}{H_0}\right) = R_0 \sum_{\alpha_i} r_{\alpha_i} \left(\frac{H}{H_0}\right)^{\alpha_i} \tag{A.5}$$

according to

$$r_{\alpha_i} \rightarrow r^*_{\alpha_i} = \beta(\alpha_i) r_{\alpha_i} \tag{A.6}$$

with $R_0 = R_S(0)$, $\alpha_0 = 0$, $\beta(\alpha_0) = 1$, $r_{\alpha_0} = 1$ and $\alpha_i < \alpha_j$ if $i < j$. $\beta(\alpha)$ is given by

$$\beta(\alpha) = \frac{2\int_0^1 h\,[1 - a(h)]\,\mathrm{d}h}{(2+\alpha)\int_0^1 h^{1+\alpha}\,[1 - a(h)]\,\mathrm{d}h}. \tag{A.7}$$

In general, α_i do not need to be integer numbers, but in practice Eq. A.5 will probably be a polynomial fit to experimental data. For fits up to 5^{th} order Fig. A.7 shows the necessary functions to calculate $\beta(\alpha)$ for the first quadrupole mode. The resulting correction coefficients $\beta(\alpha)$ for the first three quadrupole modes are given in Tab. A.1. Intermediate values in case of non-integer α are obtained by interpolation or re-evaluation of $(1-a)h^{1+\alpha}$ [98]. The fact that $\beta(\alpha) > 1$ for $\alpha > 0$ is equivalent to the statement that a field-dependent surface resistance as measured with the QPR is systematically underestimated. Note that this method yields consistent results compared to the one of [97] with the advantage that this method is applicable to any unknown RF field dependence of R_S without the need for an iterative numerical computation each time a new set of measurement data is obtained.

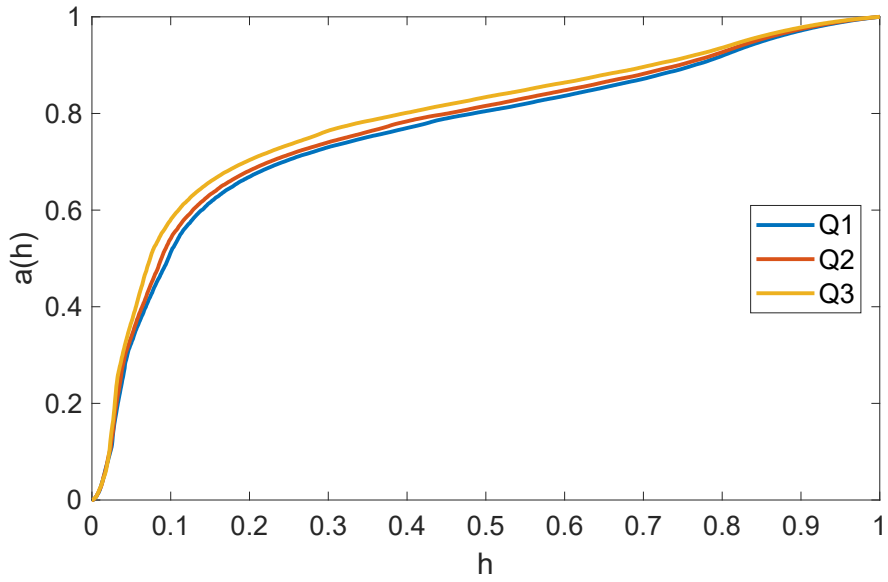

Figure A.6: *Field distribution function $a(h)$ denoting the fractional sample area exposed to an RF field $|H| \leq hH_{pk}$ for the first three quadrupole modes.*

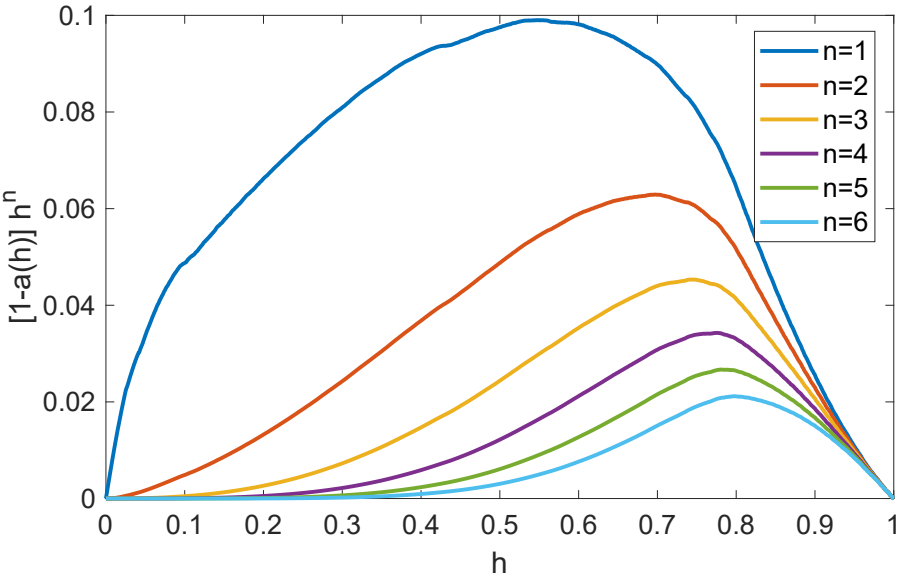

Figure A.7: *Products of $(1-a)$ with integer powers of h as needed for the calculation of $\beta(\alpha)$ (Q1 only).*

Table A.1: *Correction coefficients $\beta(\alpha)$ for the first three quadrupole modes at integer values of α, i.e. polynomial fits of the surface resistance. By definition $\beta(0) = 1$.*

α	0	1	2	3	4	5
Q1	1	1.38	1.75	2.14	2.55	2.99
Q2	1	1.39	1.78	2.19	2.62	3.07
Q3	1	1.41	1.81	2.24	2.68	3.16

A.5 Nb_3Sn Penetration Depth Measurement at 846 MHz

In this section details on data processing and fit procedure for the Nb_3Sn penetration depth measurement at 846 MHz (Q2) are given. For raw data of the frequency shift as a function of time resp. sample temperature see Fig. A.8. For temperatures too close to T_c the PLL failed to keep lock and the frequency counter measured the open loop center frequency of the signal generator only (see Fig. 3.5 for details on the PLL system). This range is excluded from further analysis. Details on the helium level correction are given in the main part, see Fig. 4.6b.

When varying the input data range for penetration depth fits according to Eq. 3.29, only data for increasing sample temperature gives consistent and low values of RMSE. This is observed at Q1 as well, indicating a systematic error due to thermal issues. As highlighted by a horizontal red line in Fig. A.9, input data with $T > 12\,\mathrm{K}$ can be accepted for penetration depth fits. Resulting values for T_c and λ_0 are given in Fig. A.10, gray areas indicate the uncertainty of fit parameters.

Final results are:

$$T_c = (18.15 \pm 0.04)\,\mathrm{K}$$
$$\lambda_0 = (164 \pm 6)\,\mathrm{nm}$$

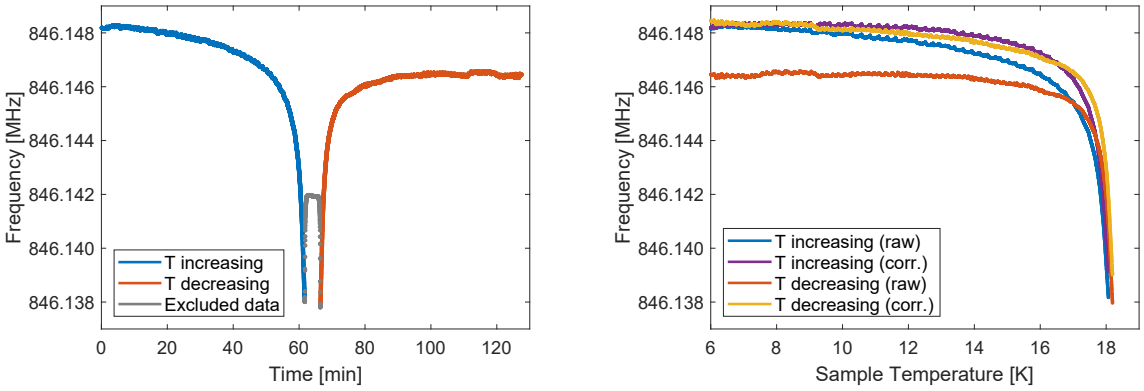

Figure A.8: *Measurement data for frequency shift vs. sample temperature at 846 MHz before (left) and after (right) helium level correction.*

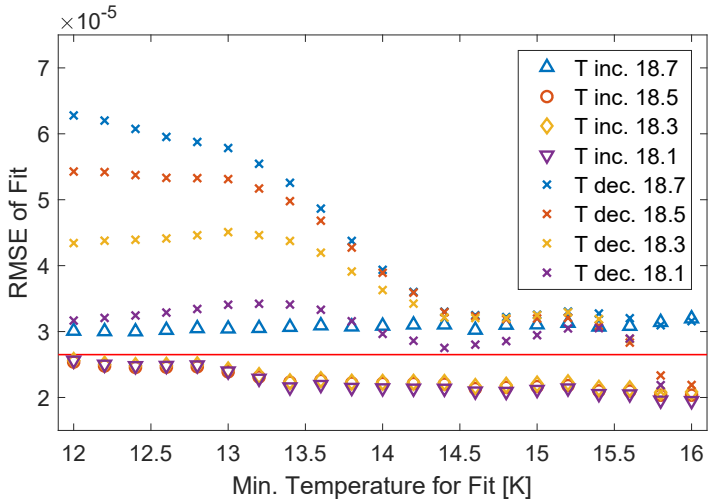

Figure A.9: *RMSE of penetration depth fits at 846 MHz when varying lower and upper boundaries of the input data range. Fits with RMSE above the horizontal red line are excluded, this especially concerns data for decreasing sample temperature.*

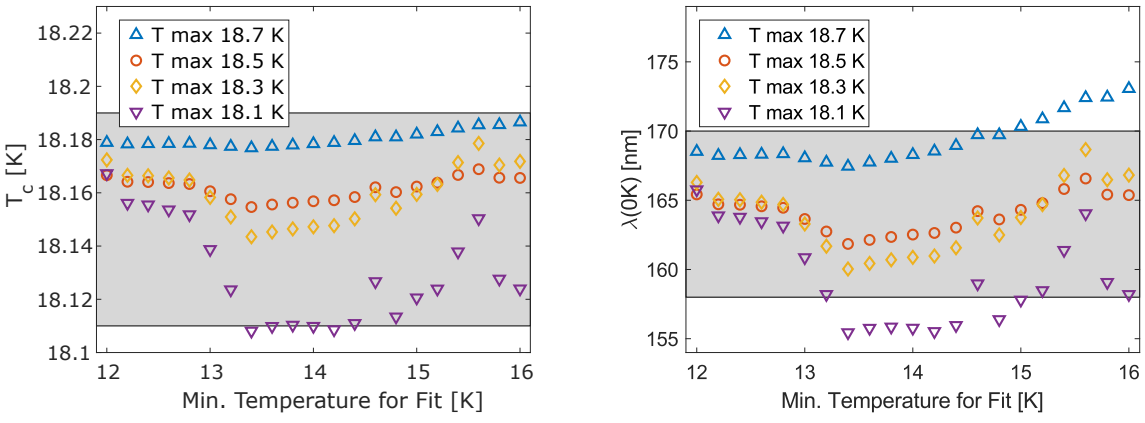

Figure A.10: *Penetration depth fit results at 846 MHz. The estimated fit uncertainties are highlighted gray.*

A.6 Residual Resistance Fits for the NbTiN-AlN-Nb Sample

The residual resistance for the S-I-S′ sample is obtained from BCS fits to measured surface resistance data using Eq. 4.1. A more complex dependence on temperature is theoretically expected due to the different BCS contributions of the two superconducting layers, furthermore, non-monotonic behavior in temperature is experimentally observed. Hence, this fit procedure is valid only approximately but its applicability is confirmed with the following plots.

For all three quadrupole modes (Q1 to Q3) the RMSE value of BCS fits vs. upper limit of the input data range is shown first. For each mode, a threshold temperature T_{max} is defined with acceptable fit quality for $T < T_{\mathrm{max}}$. For each quadrupole mode T_{max} is indicated by vertical red lines. Subsequently, the fitted values of R_{res} in the appropriate data range are averaged as highlighted by horizontal colored lines. This is done for each level of RF field strength individually, resulting values are shown in Fig. A.14 (see also Fig. 5.6b). Since both RMSE and R_{res} vary comparatively little, the obtained values can be regarded as temperature-independent (residual) surface resistance. Note that this procedure does not make a statement whether or not the total measured surface resistance as a function of temperature has its source in the BCS theory.

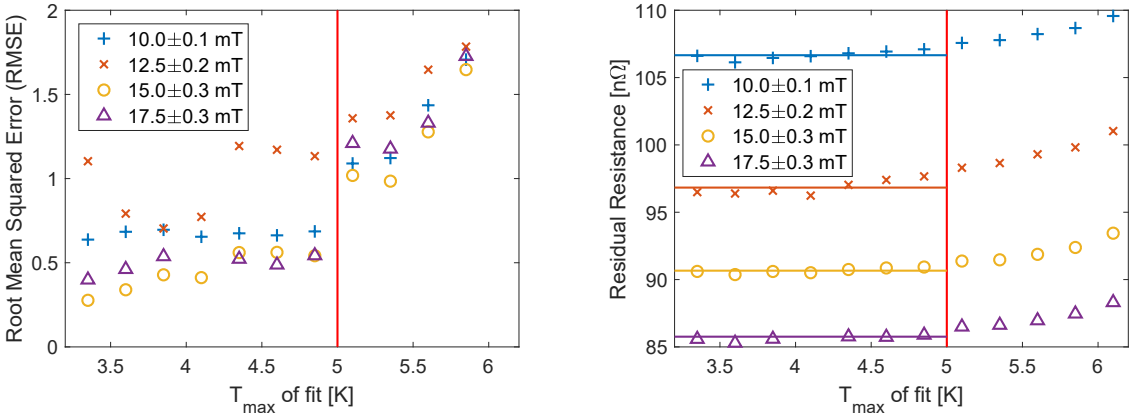

Figure A.11: *S-I-S′ residual resistance fits at 414 MHz for different applied RF magnetic fields.*

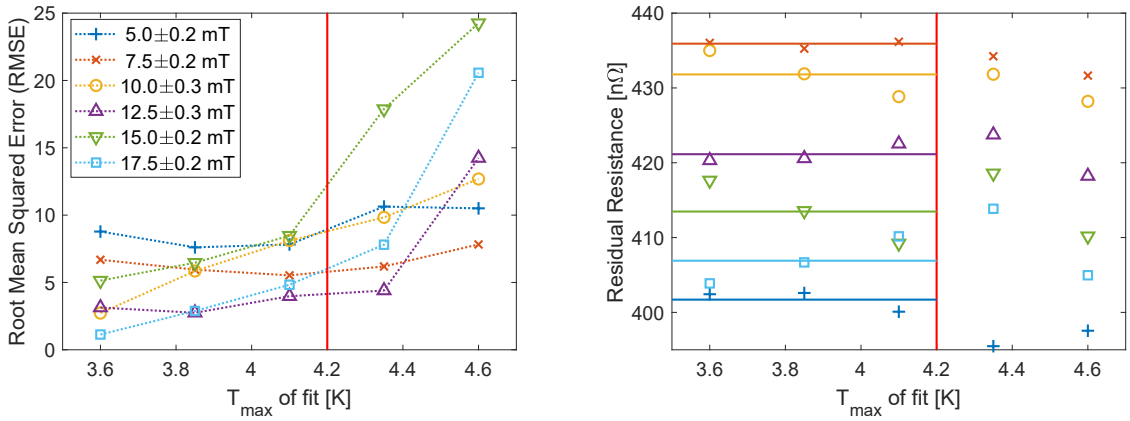

Figure A.12: *S-I-S′ residual resistance fits, 845 MHz.*

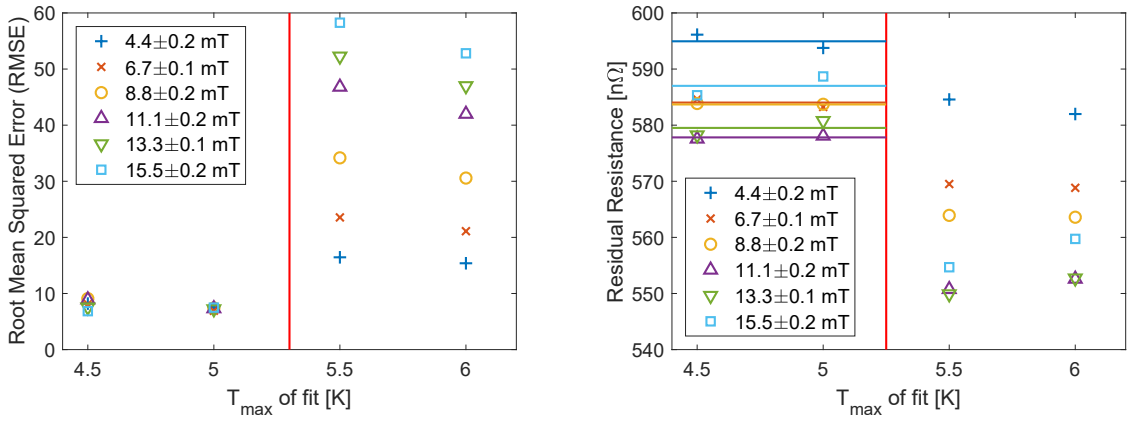

Figure A.13: *S-I-S′ residual resistance fits, 1286 MHz.*

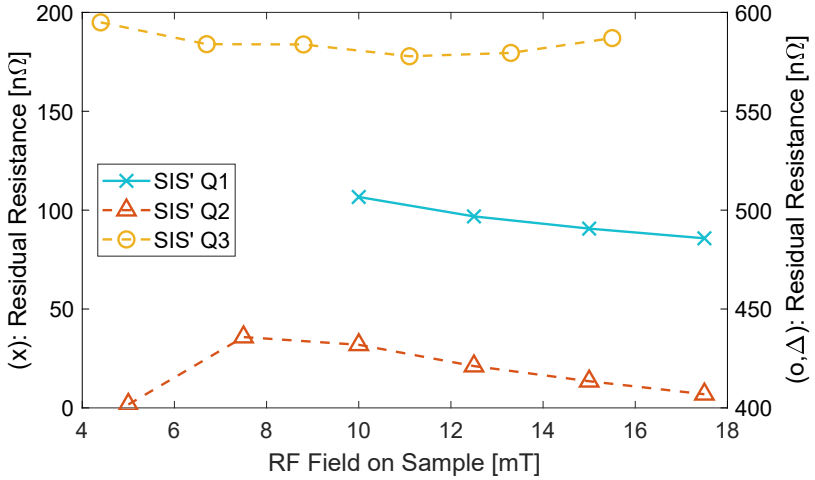

Figure A.14: *S-I-S′ temperature independent residual resistance as a function of RF field. The right-hand y-axis for data points at Q2 and Q3 is shifted but has the same steps as the left-hand axis.*

A.7 S-I-S′ Baseline Penetration Depth Measurement

During the baseline measurement of the niobium substrate prior to coating with AlN and NbTiN layers as discussed in Chapter 5, the penetration depth was determined using the VNA-based method as described in Section 3.6.2. All VNA scans were obtained during one thermal cycle. Reference points at low temperature before and after the cycle are used to derive the pressure sensitivity of each mode and to correct the systematic drift due to the decreasing level of liquid helium with time (see Section 3.2.3). Fig. A.15 shows measurement data and fits according to Eq. 3.29. Fit results are given in Tab. A.2.
All fit results are consistent within their uncertainties. While T_c is close to the literature value of 9.25 K [120], the obtained RRR is surprisingly low. From the used sheet material RRR ≈ 300 was expected. After baseline measurement and shipping to JLab, the substrate was prepared for the deposition process using EP. During that, unexpected structures appeared, requiring a total removal of 100 µm to restore a clean surface. This might be an explanation for the observed low RRR or long $\lambda(0\,\mathrm{K})$.

Table A.2: *Penetration depth measurement of the niobium substrate prior to the deposition of S-I coatings. Error bars give the statistical fit uncertainty.*

Frequency	414 MHz	846 MHz	1286 MHz
T_c	(9.29 ± 0.01) K	(9.33 ± 0.01) K	(9.39 ± 0.09) K
$\lambda(0\,\mathrm{K})$	(58 ± 4) nm	(67 ± 6) nm	(57 ± 7) nm
λ_L		32 nm (fixed)	[29]
ξ_0		39 nm (fixed)	[29]
ℓ	(27 ± 6) nm	(18 ± 5) nm	(27 ± 14) nm
RRR	10 ± 2	7 ± 2	10 ± 5

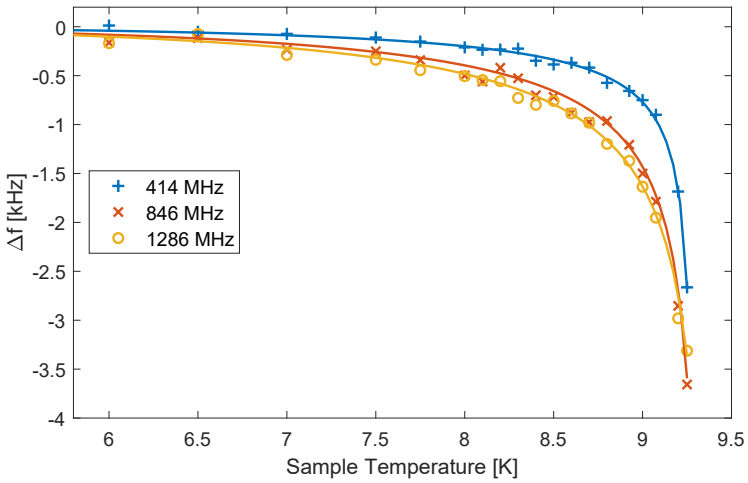

Figure A.15: *Baseline penetration depth measurement of the niobium substrate.*

A.8 Technical Details on Computer Simulations

As addendum to the discussion of computer simulations in Sections 3.2.1, 3.3.2, 3.3.3 and 3.5.2, technical details concerning software and hardware are provided here.

Computer Hardware

Two workstation computers with Microsoft Windows operation system were used for simulations with hardware parameters listed in Tab. A.3.

Table A.3: *Hardware parameters of simulations computers.*

Parameter	Computer A	Computer B
CPU	Intel® Core™ i7-6700 3.4 GHz	Intel® Xeon® E5-2630 v4 2.2 GHz
Memory	32 GB	256 GB

Electromagnetic Simulations

Electromagnetic simulations on the RF field distribution inside the QPR and on the coupling (Q_{ext}) of input and pickup antenna were done using CST Microwave Studio® (MWS), Release Version 2016.07, Nov 11 2016 [82]. Within this work, three electromagnetic simulations were computed which are listed in Tab. A.4. All simulations used tetrahedral mesh and the eigenmode solver with default accuracy setting of 10^{-9}.

Table A.4: *Summary of electromagnetic simulations.*

Model	Short description	Tetrahedra	Time	CPU	References
EM-1a	Input coupling	174300	16 min	A	Sections 3.2.1 and A.2
EM-1b	Pickup coupling	381100	23 min	A	Sections 3.2.1 and A.2
EM-2	Sample fields and coaxial damping	1964424	7 h	B	Sections 3.3.2, 3.3.3 and 3.5.2

Note: Technically, the simulations EM-1a/b are parameter scans for the rotational angle which were repeated for each port location (A, B). Since the number of tetrahedra and the computing time did not differ significantly, average numbers are listed in Tab. A.4. The given computing time applies to each parameter setting.

Thermodynamic Simulations

For simulations of static and dynamic temperature distributions COMSOL Multiphysics® Version 5.4.0.388 [87] was used. For licensing reasons Computer B was used only. Especially in case of static simulations with rotational symmetry a computer with much less memory would be sufficient. Within this work, three thermodynamic simulations were computed which are listed in Tab. A.5. All simulations were calculated using tetrahedral mesh and default accuracy settings of the solvers. The physics module "Heat Transfer in Solids" is already part of the core package of COMSOL, additionally the CAD import module was used for defining the simulation geometry.

Table A.5: *Summary of thermodynamic simulations.*

Model	Short description	DFE	Time	References
TD-1	Static 2D w/ rot. symmetry	41022	< 1 min	Section 3.3.2
TD-2	Static 3D	583058	4 min	Section 3.3.3
TD-3	Transient simplified 3D	252603 – 841374	6 h 12 min	Section 3.5.2

In order to simulate RF heating of the sample surface, the squared RF magnetic field of EM-3 is used as boundary heat source. The normalization of input data is done within COMSOL by calculating the integral on the sample surface. The number of degrees of freedom (DFE) for TD-3 strongly depends on the sample thickness, hence minimum and maximum numbers are given in Tab. A.5.

Bibliography

[1] J.-P. Labrie and H. Euteneuer. "Power handling capability of water cooled cw linac structures". In: *Nuclear Instruments and Methods in Physics Research Section A: Accelerators, Spectrometers, Detectors and Associated Equipment* 247 (1986), pp. 281–287. DOI: 10.1016/0168-9002(86)91308-2.

[2] *The European X-Ray Free-Electron Laser – Technical Design Report*. 2007. URL: http://xfel.desy.de/technical_information/tdr/tdr/.

[3] *LCLS-II Conceptual Design Report*. 2014. URL: http://slac.stanford.edu/pubs/slacreports/reports09/slac-r-1092.pdf.

[4] *ESS Technical Design Report*. 2013. URL: http://eval.esss.lu.se/cgi-bin/public/DocDB/ShowDocument?docid=274.

[5] J. Wei et al. "The FRIB SC-Linac - Installation and Phased Commissioning". In: *Proc. of the 19th International Conference on RF Superconductivity (SRF'19), Dresden, Germany*. 2019. DOI: 10.18429/JACoW-SRF2019-MOFAA3.

[6] J. L. A. Fernandez et al. "A Large Hadron Electron Collider at CERN Report on the Physics and Design Concepts for Machine and Detector". In: *Journal of Physics G: Nuclear and Particle Physics* 39 (2012), p. 075001. DOI: 10.1088/0954-3899/39/7/075001.

[7] F. Willeke. *Electron-Ion Collider eRHIC Pre-Conceptual Design Report*. 2019. DOI: 10.2172/1547019.

[8] H. Padamsee, J. Knobloch, and T. Hays. *RF Superconductivity for Accelerators*. 2nd edition. Wiley, 2008.

[9] R. L. Geng et al. "High gradient studies for ILC with single-cell re-entrant shape and elliptical shape cavities made of fine-grain and large-grain niobium". In: *Proc. of the 22nd Particle Accelerator Conference (PAC'07), Albuquerque, New Mexico, USA*. 2007, pp. 2337–2339. URL: http://accelconf.web.cern.ch/AccelConf/p07/PAPERS/WEPMS006.PDF.

[10] A. Grassellino et al. "Accelerating fields up to 49 MV/m in TESLA-shape superconducting RF niobium cavities via 75C vacuum bake". 2018. arXiv: 1806.09824.

[11] A. Romanenko et al. "Ultra-high quality factors in superconducting niobium cavities in ambient magnetic fields up to 190 mG". In: *Applied Physics Letters* 105 (2014), p. 234103. DOI: 10.1063/1.4903808.

[12] P. Goudket, T. Junginger, and B. P. Xiao. "Devices for SRF material characterization". In: *Superconductor Science and Technology* 30 (2016), p. 013001. DOI: 10.1088/0953-2048/30/1/013001.

[13] R. Kleindienst, O. Kugeler, and J. Knobloch. "Development of an Optimized Quadrupole Resonator at HZB". In: *Proc. of the 16th International Conference on RF Superconductivity (SRF'13), Paris, France*. 2013, pp. 614–616. URL: http://accelconf.web.cern.ch/AccelConf/SRF2013/papers/tup074.pdf.

[14] R. Kleindienst et al. "Commissioning Results of the HZB Quadrupole Resonator". In: *Proc. of the 17th International Conference on RF Superconductivity (SRF'15), Whistler, BC, Canada*. 2015, pp. 930–936. DOI: 10.18429/JACoW-SRF2015-WEA1A04.

[15] E. Mahner et al. "A new instrument to measure the surface resistance of superconducting samples at 400 MHz". In: *Review of Scientific Instruments* 74 (2003), pp. 3390–3394. DOI: 10.1063/1.1578157.

[16] A.-M. Valente-Feliciano. "Superconducting RF materials other than bulk niobium: a review". In: *Superconductor Science and Technology* 29 (2016), p. 113002. DOI: 10.1088/0953-2048/29/11/113002.

[17] K. Hübner. "The LEP superconducting RF system". In: *Proceedings, APS / DPF / DPB Summer Study on the Future of Particle Physics (Snowmass 2001), Snowmass, Colorado, USA*. 2001. URL: http://cds.cern.ch/record/523666.

[18] D. Boussard et al. "The LHC superconducting cavities". In: *Proc. of the 18th Particle Accelerator Conference (PAC'99), New York, USA*. 1999, pp. 946–948. URL: http://accelconf.web.cern.ch/AccelConf/p99/PAPERS/MOP120.PDF.

[19] A. Gurevich. "Enhancement of rf breakdown field of superconductors by multilayer coating". In: *Applied Physics Letters* 88 (2006), p. 012511. DOI: 10.1063/1.2162264.

[20] A. Gurevich. "Maximum screening fields of superconducting multilayer structures". In: *AIP Advances* 5 (2015), p. 017112. DOI: 10.1063/1.4905711.

[21] T. Kubo. "Multilayer coating for higher accelerating fields in superconducting radio-frequency cavities: a review of theoretical aspects". In: *Superconductor Science and Technology* 30 (2016), p. 023001. DOI: 10.1088/1361-6668/30/2/023001.

[22] M. Tinkham. *Introduction to Superconductivity*. 2nd edition, McGraw-Hill Inc., 1996.

[23] H. Kamerlingh Onnes. "Further experiments with liquid helium. C. On the change of electric resistance of pure metals at very low temperatures etc. IV. The resistance of pure mercury at helium temperatures." In: *Proc. KNAW 13 II* (1911). [Comm. Leiden 120b (1911)], pp. 1274–1276.

[24] W. Meissner and R. Ochsenfeld. "Ein neuer Effekt bei Eintritt der Supraleitfähigkeit". In: *Naturwissenschaften* 21 (1933), pp. 787–788. DOI: 10.1007/BF01504252.

[25] F. London and H. London. “The Electromagnetic Equations of the Supraconductor”. In: *Proceedings of the Royal Society of London. Series A - Mathematical and Physical Sciences* 149 (1935), pp. 71–88. DOI: 10.1098/rspa.1935.0048.

[26] C. J. Gorter and H. Casimir. “The Thermodynamics of the Superconducting State”. In: *Zeitschrift für Technische Physik* 15 (1934), pp. 539–542.

[27] C. Gorter and H. Casimir. “On supraconductivity I”. In: *Physica* 1 (1934), pp. 306–320. DOI: 10.1016/S0031-8914(34)90037-9.

[28] A. B. Pippard. “An experimental and theoretical study of the relation between magnetic field and current in a superconductor”. In: *Proceedings of the Royal Society of London. Series A - Mathematical and Physical Sciences* 216 (1953), pp. 547–568. DOI: 10.1098/rspa.1953.0040.

[29] J. P. Turneaure, J. Halbritter, and H. A. Schwettman. “The surface impedance of superconductors and normal conductors: The Mattis-Bardeen theory”. In: *Journal of Superconductivity* 4 (1991), pp. 341–355. DOI: 10.1007/BF00618215.

[30] V. L. Ginzburg and L. D. Landau. *On the Theory of Superconductivity.* Zh. Eksp. Teor. Fiz. 20 (1950) pp. 1064-1082, English Translation in: V. L. Ginzburg, On Superconductivity and Superfluidity, Springer-Verlag Berlin Heidelberg, 2009, pp. 113-137.

[31] A. A. Abrikosov. “On the Magnetic Properties of Superconductors of the Second Group”. In: *Sov. Phys. JETP* 5 (1957). [Zh. Eksp. Teor. Fiz. 32, 1442 (1957)], pp. 1174–1182. URL: http://www.jetp.ac.ru/cgi-bin/dn/e_005_06_1174.pdf.

[32] L. P. Gor’kov. “Microscopic Derivation of the Ginzburg-Landau Equations in the Theory of Superconductivity”. In: *Sov. Phys. JETP* 9 (1959). [Zh. Eksp. Teor. Fiz. 36, 1918 (1959)], pp. 1364–1367. URL: http://www.jetp.ac.ru/cgi-bin/dn/e_009_06_1364.pdf.

[33] J. Bardeen, L. N. Cooper, and J. R. Schrieffer. “Microscopic Theory of Superconductivity”. In: *Phys. Rev.* 106 (1957), pp. 162–164. DOI: 10.1103/PhysRev.106.162.

[34] J. Bardeen, L. N. Cooper, and J. R. Schrieffer. “Theory of Superconductivity”. In: *Phys. Rev.* 108 (1957), pp. 1175–1204. DOI: 10.1103/PhysRev.108.1175.

[35] E. Maxwell. “Isotope Effect in the Superconductivity of Mercury”. In: *Phys. Rev.* 78 (1950), pp. 477–477. DOI: 10.1103/PhysRev.78.477.

[36] C. A. Reynolds et al. “Superconductivity of Isotopes of Mercury”. In: *Phys. Rev.* 78 (1950), pp. 487–487. DOI: 10.1103/PhysRev.78.487.

[37] D. C. Mattis and J. Bardeen. “Theory of the Anomalous Skin Effect in Normal and Superconducting Metals”. In: *Phys. Rev.* 111 (1958), pp. 412–417. DOI: 10.1103/PhysRev.111.412.

[38] A. Gurevich. “Theory of RF superconductivity for resonant cavities”. In: *Superconductor Science and Technology* 30 (2017), p. 034004. DOI: 10.1088/1361-6668/30/3/034004.

[39] A. Gurevich and T. Kubo. "Surface impedance and optimum surface resistance of a superconductor with an imperfect surface". In: *Phys. Rev. B* 96 (2017), p. 184515. DOI: 10.1103/PhysRevB.96.184515.

[40] B. Aune et al. "Superconducting TESLA cavities". In: *Phys. Rev. ST Accel. Beams* 3 (2000), p. 092001. DOI: 10.1103/PhysRevSTAB.3.092001.

[41] H. Padamsee. *RF Superconductivity: Science, Technology and Applications*. Wiley, 2009.

[42] G. E. H. Reuter and E. H. Sondheimer. "The theory of the anomalous skin effect in metals". In: *Proceedings of the Royal Society of London. Series A - Mathematical and Physical Sciences* 195 (1948), pp. 336–364. DOI: 10.1098/rspa.1948.0123.

[43] J. Halbritter. *FORTRAN-program for the computation of the Surface Impedance of Superconductors*. Tech. rep. KFK EXT 3/70-6. 1970. DOI: 10.5445/IR/270004230.

[44] J. P. Turneaure and I. Weissman. "Microwave Surface Resistance of Superconducting Niobium". In: *Journal of Applied Physics* 39 (1968), pp. 4417–4427. DOI: 10.1063/1.1656986.

[45] B. Bonin. "Materials for superconducting cavities". In: *CAS - CERN Accelerator School, Hamburg, Germany*. 1995. DOI: 10.5170/CERN-1996-003.191.

[46] J.-M. Vogt, O. Kugeler, and J. Knobloch. "High-Q operation of superconducting rf cavities: Potential impact of thermocurrents on the rf surface resistance". In: *Phys. Rev. ST Accel. Beams* 18 (2015), p. 042001. DOI: 10.1103/PhysRevSTAB.18.042001.

[47] M. Peiniger et al. "Work on Nb3Sn Cavities at Wuppertal". In: *Proc. of the 3rd Workshop on RF Superconductivity (SRF'87), Argonne National Laboratory, Illinois, USA*. 1987, pp. 503–532. URL: http://accelconf.web.cern.ch/AccelConf/srf87/papers/srf87e04.pdf.

[48] A. Grassellino et al. "Nitrogen and argon doping of niobium for superconducting radio frequency cavities: a pathway to highly efficient accelerating structures". In: *Superconductor Science and Technology* 26 (2013), p. 102001. DOI: 10.1088/0953-2048/26/10/102001.

[49] P. Dhakal et al. "Enhancement in Quality Factor of SRF Niobium Cavities by Material Diffusion". In: *IEEE Transactions on Applied Superconductivity* 25 (2015), pp. 1–4. DOI: 10.1109/TASC.2014.2359640.

[50] A. Gurevich. "Reduction of Dissipative Nonlinear Conductivity of Superconductors by Static and Microwave Magnetic Fields". In: *Phys. Rev. Lett.* 113 (2014), p. 087001. DOI: 10.1103/PhysRevLett.113.087001.

[51] G. Müller. "Microwave Properties of High-Tc Oxide Superconductors". In: *Proc. of the 4th Workshop on RF Superconductivity (SRF'89), KEK, Tsukuba, Japan*. 1989, pp. 267–304. URL: http://accelconf.web.cern.ch/AccelConf/SRF89/papers/srf89d01.pdf.

[52] J. Halbritter. “rf residual losses, surface impedance, and granularity in superconducting cuprates”. In: *Journal of Applied Physics* 68 (1990), pp. 6315–6326. DOI: 10.1063/1.346875.

[53] J. Halbritter. “Transport in superconducting niobium films for radio frequency applications”. In: *Journal of Applied Physics* 97 (2005), p. 083904. DOI: 10.1063/1.1874292.

[54] M. Becks et al. “Superconducting Cavities and their Applications – Recent Work at the University of Wuppertal”. In: *Proc. of the 4th Workshop on RF Superconductivity (SRF’89), KEK, Tsukuba, Japan*. 1989, pp. 109–138. URL: http://accelconf.web.cern.ch/AccelConf/SRF89/papers/srf89b01.pdf.

[55] S. Posen and D. L. Hall. “Nb3Sn superconducting radiofrequency cavities: fabrication, results, properties, and prospects”. In: *Superconductor Science and Technology* 30 (2017), p. 033004. DOI: 10.1088/1361-6668/30/3/033004.

[56] V. Palmieri and R. Vaglio. “Thermal contact resistance at the Nb/Cu interface as a limiting factor for sputtered thin film RF superconducting cavities”. In: *Superconductor Science and Technology* 29 (2015), p. 015004. DOI: 10.1088/0953-2048/29/1/015004.

[57] D. E. Mapother. “Thermodynamic Consistency of Critical Field and Specific Heat Data for Superconducting Sn and In”. In: *Phys. Rev.* 126 (1962), pp. 2021–2029. DOI: 10.1103/PhysRev.126.2021.

[58] M. Hein. *High-Temperature-Superconductor Thin Films at Microwave Frequencies*. Springer, New York, 1999.

[59] J. L. Harden and V. Arp. “The lower critical field in the Ginzburg-Landau theory of superconductivity”. In: *Cryogenics* 3 (1963), pp. 105–108. DOI: 10.1016/0011-2275(63)90029-8.

[60] G. Stejic et al. “Effect of geometry on the critical currents of thin films”. In: *Phys. Rev. B* 49 (1994), pp. 1274–1288. DOI: 10.1103/PhysRevB.49.1274.

[61] M. K. Transtrum, G. Catelani, and J. P. Sethna. “Superheating field of superconductors within Ginzburg-Landau theory”. In: *Phys. Rev. B* 83 (2011), p. 094505. DOI: 10.1103/PhysRevB.83.094505.

[62] A. J. Dolgert, S. J. Di Bartolo, and A. T. Dorsey. “Superheating fields of superconductors: Asymptotic analysis and numerical results”. In: *Phys. Rev. B* 53 (1996), pp. 5650–5660. DOI: 10.1103/PhysRevB.53.5650.

[63] A. J. Dolgert, S. J. Di Bartolo, and A. T. Dorsey. “Erratum: Superheating fields of superconductors: Asymptotic analysis and numerical results [Phys. Rev. B 53, 5650 (1996)]”. In: *Phys. Rev. B* 56 (1997), pp. 2883–2883. DOI: 10.1103/PhysRevB.56.2883.

[64] G. Catelani and J. P. Sethna. “Temperature dependence of the superheating field for superconductors in the high-κ London limit”. In: *Phys. Rev. B* 78 (2008), p. 224509. DOI: 10.1103/PhysRevB.78.224509.

[65] K. Saito. "Theoretical Critical Field in RF Application". In: *Proc. of the 11th International Conference on RF Superconductivity (SRF'03), Lübeck/Travemünde, Germany.* 2003, pp. 1–16. URL: http://accelconf.web.cern.ch/AccelConf/SRF2003/papers/moo02.pdf.

[66] S. Posen, N. Valles, and M. Liepe. "Radio Frequency Magnetic Field Limits of Nb and Nb_3Sn". In: *Phys. Rev. Lett.* 115 (2015), p. 047001. DOI: 10.1103/PhysRevLett.115.047001.

[67] T. Yogi, G. J. Dick, and J. E. Mercereau. "Critical rf Magnetic Fields for Some Type-I and Type-II Superconductors". In: *Phys. Rev. Lett.* 39 (1977), pp. 826–829. DOI: 10.1103/PhysRevLett.39.826.

[68] T. Junginger, W. Weingarten, and C. Welsch. "Extension of the measurement capabilities of the quadrupole resonator". In: *Review of Scientific Instruments* 83 (2012), p. 063902. DOI: 10.1063/1.4725521.

[69] T. Kubo. "Models of the Magnetic Field Enhancement at Pits". In: *Proc. of the 16th International Conference on RF Superconductivity (SRF'13), Paris, France.* 2013, pp. 433–437. URL: http://accelconf.web.cern.ch/AccelConf/SRF2013/papers/tup008.pdf.

[70] T. Kubo. "Two-Dimensional Models of the Magnetic-Field Enhancement at Pit and Bumps". In: *Proc. of the 5th International Particle Accelerator Conference (IPAC'14), Dresden, Germany.* 2014, pp. 2525–2527. DOI: 10.18429/JACoW-IPAC2014-WEPRI024.

[71] J. Knobloch et al. "High-Field Q Slope in Superconducting Cavities Due to Magnetic Field Enhancements at Grain Boundaries". In: *Proc. of the 9th International Workshop on RF Superconductivity (SRF'99), Santa Fe, NM, USA.* 1999, pp. 77–91. URL: http://accelconf.web.cern.ch/AccelConf/SRF99/papers/tua004.pdf.

[72] R. Porter et al. "Surface Roughness Effect on the Performance of Nb3Sn Cavities". In: *Proc. of the 28th Linear Accelerator Conference (LINAC'16), East Lansing, MI, USA.* 2016, pp. 129–132. DOI: 10.18429/JACoW-LINAC2016-MOPRC027.

[73] S. Posen et al. "Theoretical Field Limits for Multi-Layer Superconductors". In: *Proc. of the 16th International Conference on RF Superconductivity (SRF'13), Paris, France.* 2013, pp. 794–799. URL: http://accelconf.web.cern.ch/AccelConf/SRF2013/papers/weioc04.pdf.

[74] S. Posen et al. "Shielding Superconductors with Thin Films as Applied to rf Cavities for Particle Accelerators". In: *Phys. Rev. Applied* 4 (2015), p. 044019. DOI: 10.1103/PhysRevApplied.4.044019.

[75] T. Junginger et al. "Critical Fields of SRF Materials". In: *Proc. of the 9th International Particle Accelerator Conference (IPAC'18), Vancouver, BC, Canada.* 2018, pp. 3921–3924. DOI: 10.18429/JACoW-IPAC2018-THPAL118.

[76] S. Keckert et al. “Critical fields of Nb3Sn prepared for superconducting cavities”. In: *Superconductor Science and Technology* 32 (2019), p. 075004. DOI: 10.1088/1361-6668/ab119e.

[77] E. Brigant and E. Haebel. *Numerical Simulations in the Design of a Quadripolar Resonator*. Technical Note, EDMS 1178982, 1997.

[78] E. Brigant, E. Haebel, and E. Mahner. “The Quadrupole Resonator, Design Considerations and Layout of a New Instrument for the RF Characterization of Superconducting Samples”. In: *Proc. of the 6th European Particle Accelerator Conference (EPAC'98), Stockholm, Sweden*. 1998, pp. 1855–1857. URL: http://accelconf.web.cern.ch/AccelConf/e98/PAPERS/TUP042B.PDF.

[79] E. Chiaveri et al. “The Quadrupole Resonator, Construction, RF System, Field Calculations and First Applications”. In: *Proc. of the 6th European Particle Accelerator Conference (EPAC'98), Stockholm, Sweden*. 1998, pp. 1852–1854. URL: http://accelconf.web.cern.ch/AccelConf/e98/PAPERS/TUP041B.PDF.

[80] R. Kleindienst. *Radio Frequency Characterization of Superconductors for Particle Accelerators*. Dissertation. Universität Siegen, 2017. URL: http://dokumentix.ub.uni-siegen.de/opus/volltexte/2018/1329/.

[81] S. Keckert. *Optimizing a Calorimetry Chamber for the RF Characterization of Superconductors*. Master thesis. Universität Siegen, 2015. URL: https://cds.cern.ch/record/2156188.

[82] Computer Simulation Technology AG. *CST Microwave Studio®*. Release Version 2016.07, Nov 11 2016.

[83] S. Keckert et al. “The Challenge to Measure nΩ Surface Resistance on SRF Samples”. In: *Proc. of the 9th International Particle Accelerator Conference (IPAC'18), Vancouver, BC, Canada*. 2018, pp. 2812–2815. DOI: 10.18429/JACoW-IPAC2018-WEPML049.

[84] D. Alesini. “Power coupling”. In: *Proceedings, CAS - CERN Accelerator School: RF for Accelerators, Ebeltoft, Denmark*. 2010. arXiv: 1112.3201 [physics.acc-ph].

[85] J. Linn. *Analysis and Reduction of Microphonic Detuning in the HZB Superconducting Quadrupole Resonator*. Bachelor thesis. Universität Siegen, 2017.

[86] Cryodata Inc. *HEPAK*.

[87] COMSOL Inc. *COMSOL Multiphysics®*. Version 5.4.0.388.

[88] R. P. Reed and A. F. Clark. *Materials at low temperatures*. American Society for Metals, 1983. ISBN: 0-87170-146-4.

[89] C. Y. Ho, R. W. Powell, and P. E. Liley. “Thermal Conductivity of the Elements”. In: *Journal of Physical and Chemical Reference Data* (1974).

[90] F. Koechlin and B. Bonin. "Parametrization of the niobium thermal conductivity in the superconducting state". In: *Superconductor Science and Technology* 9 (1996), pp. 453–460. DOI: 10.1088/0953-2048/9/6/003.

[91] H. M. Rosenberg. "The thermal conductivity of metals at low temperatures". In: *Philosophical Transactions of the Royal Society of London A: Mathematical, Physical and Engineering Sciences* 247 (1955), pp. 441–497. DOI: 10.1098/rsta.1955.0003.

[92] D. Gall. "Electron mean free path in elemental metals". In: *Journal of Applied Physics* 119 (2016), p. 085101. DOI: 10.1063/1.4942216.

[93] M. Fouaidy and N. Hammoudi. "RRR of copper coating and low temperature electrical resistivity of material for TTF couplers". In: *Physica C: Superconductivity* 441 (2006). Proceedings of the 12th International Workshop on RF Superconductivity, pp. 137–144. DOI: 10.1016/j.physc.2006.03.049.

[94] X. Singer et al. "Properties and Structure of Electrodeposited Copper Layers in Parts of the TTF Main Coupler". In: *Proc. of the 11th Workshop on RF Superconductivity (SRF'03), Lübeck/Travemünde, Germany*. 2003, pp. 652–654. URL: http://accelconf.web.cern.ch/AccelConf/SRF2003/papers/thp18.pdf.

[95] T. Powers. "Theory and Practice of Cavity RF Test Systems". In: *Proc. of the 12th International Workshop on RF Superconductivity (SRF'05), Ithaca, New York, USA*. 2005, pp. 40–70. URL: http://accelconf.web.cern.ch/AccelConf/SRF2005/papers/sup02.pdf.

[96] S. Keckert, J. Knobloch, and O. Kugeler. "Error Analysis of Surface Resistance Fits to Experimental Data". In: *Proc. of the 18th International Conference on RF Superconductivity (SRF'17), Lanzhou, China*. 2017, pp. 859–862. DOI: 10.18429/JACoW-SRF2017-THPB052.

[97] R. Kleindienst et al. "Advanced Method to Extract the Surface Resistance From Q0 Measurements". In: *Proc. of the 18th International Conference on RF Superconductivity (SRF'17), Lanzhou, China*. 2017, pp. 867–869. DOI: 10.18429/JACoW-SRF2017-THPB054.

[98] J. R. Delayen et al. "Determination of the magnetic field dependence of the surface resistance of superconductors from cavity tests". In: *Phys. Rev. Accel. Beams* 21 (2018), p. 122001. DOI: 10.1103/PhysRevAccelBeams.21.122001.

[99] S. Keckert et al. "Design and First Measurements of an Alternative Calorimetry Chamber for the HZB Quadrupole Resonator". In: *Proc. of the 17th International Conference on RF Superconductivity (SRF'15), Whistler, BC, Canada*. 2015, pp. 739–743. DOI: 10.18429/JACoW-SRF2015-TUPB067.

[100] S. Keckert et al. "Surface Resistance Characterization of Nb3Sn Using the HZB Quadrupole Resonator". In: *Proc. of the 18th International Conference on RF Superconductivity (SRF'17), Lanzhou, China*. 2017, pp. 863–866. DOI: 10.18429/JACoW-SRF2017-THPB053.

[101] T. Hays, H. Padamsee, and R. W. Röth. "Determining HcRF for Nb and Nb3Sn through HPP and Transient Q Analysis". In: *Proc. of the 7th Workshop on RF Superconductivity (SRF'95), Gif-sur-Yvette, France*. 1995, pp. 437–440. URL: http://accelconf.web.cern.ch/AccelConf/SRF95/papers/srf95c14.pdf.

[102] T. Hays and H. Padamsee. "Measuring the RF Critical Field of Pb, Nb and Nb3Sn". In: *Proc. of the 8th Workshop on RF Superconductivity (SRF'97), Padova, Italy*. 1997, pp. 789–794. URL: http://accelconf.web.cern.ch/AccelConf/SRF97/papers/srf97d01.pdf.

[103] A. T. Hirshfeld, H. A. Leupold, and H. A. Boorse. "Superconducting and Normal Specific Heats of Niobium". In: *Phys. Rev.* 127 (1962), pp. 1501–1507. DOI: 10.1103/PhysRev.127.1501.

[104] J. C. Slater. "Microwave Electronics". In: *Rev. Mod. Phys.* 18 (1946), pp. 441–512. DOI: 10.1103/RevModPhys.18.441.

[105] L. C. Maier and J. C. Slater. "Field Strength Measurements in Resonant Cavities". In: *Journal of Applied Physics* 23 (1952), pp. 68–77. DOI: 10.1063/1.1701980.

[106] J. Halbritter. "On Electric Surface Impedance". In: *Zeitschrift für Physik B Condensed Matter* 31 (1978), pp. 19–37. DOI: 10.1007/BF01320123.

[107] J. Halbritter. "Change of Eigenstate in a Superconducting rf Cavity Due to a Nonlinear Response". In: *Journal of Applied Physics* 41 (1970), pp. 4581–4588. DOI: 10.1063/1.1658500.

[108] P. Kneisel, O. Stoltz, and J. Halbritter. "On surface preparation and measurement of niobium used in high-frequency cavities". In: *Journal of Applied Physics* 45 (1974), pp. 2296–2301. DOI: 10.1063/1.1663580.

[109] A. Godeke. *Nb3Sn for Radio Frequency Cavities*. Tech. rep. 62140. LBNL, 2006. URL: https://escholarship.org/uc/item/6d3753q7.

[110] S. Posen, M. Liepe, and D. L. Hall. "Proof-of-principle demonstration of Nb3Sn superconducting radiofrequency cavities for high Q0 applications". In: *Applied Physics Letters* 106 (2015), p. 082601. DOI: 10.1063/1.4913247.

[111] I. Campisi. "High field RF superconductivity: To pulse or not to pulse?" In: *IEEE Transactions on Magnetics* 21 (1985), pp. 134–141. DOI: 10.1109/TMAG.1985.1063638.

[112] S. Posen and M. Liepe. "Advances in development of Nb_3Sn superconducting radiofrequency cavities". In: *Phys. Rev. ST Accel. Beams* 17 (2014), p. 112001. DOI: 10.1103/PhysRevSTAB.17.112001.

[113] D. Hall et al. "First Results From New Single-Cell Nb3Sn Cavities Coated at Cornell University". In: *Proc. of the 8th International Particle Accelerator Conference (IPAC'17), Copenhagen, Denmark*. 2017, pp. 40–43. DOI: 10.18429/JACoW-IPAC2017-MOOCA2.

[114] A. Godeke. "A review of the properties of Nb3Sn and their variation with A15 composition, morphology and strain state". In: *Superconductor Science and Technology* 19 (2006), R68–R80. DOI: 10.1088/0953-2048/19/8/r02.

[115] Y. Trenikhina et al. "Performance-defining properties of Nb3Sn coating in SRF cavities". In: *Superconductor Science and Technology* 31 (2018), p. 015004. DOI: 10.1088/1361-6668/aa9694.

[116] A.-M. Valente-Feliciano. *Private Communication.*

[117] D. F. Moore et al. "Energy gaps of the $A-15$ superconductors Nb_3Sn, V_3Si, and Nb_3Ge measured by tunneling". In: *Phys. Rev. B* 20 (1979), pp. 2721–2738. DOI: 10.1103/PhysRevB.20.2721.

[118] P. Kneisel, O. Stoltz, and J. Halbritter. "Investigation of the Surface Resistance of a Niobium-Cavity at S-Band". In: *IEEE Transactions on Nuclear Science* 18 (1971), pp. 158–159. DOI: 10.1109/TNS.1971.4325993.

[119] P. Kneisel. "Radio-frequency superconductivity technology: Its sensitivity to surface conditions". In: *Journal of Vacuum Science & Technology A: Vacuum, Surfaces, and Films* 11 (1993), pp. 1575–1583. DOI: 10.1116/1.578507.

[120] C. P. Poole Jr. et al. *Superconductivity.* Academic Press, Elsevier Ltd., 2007.

[121] Y. M. Habib et al. "Measurements and modeling of the microwave impedance in high-T_c grain-boundary Josephson junctions: Fluxon generation and rf Josephson-vortex dynamics". In: *Phys. Rev. B* 57 (1998), pp. 13833–13844. DOI: 10.1103/PhysRevB.57.13833.

[122] Z. Zhai, P. V. Parimi, and S. Sridhar. "Nonlinear microwave impedance of short and long Josephson junctions". In: *Phys. Rev. B* 59 (1999), pp. 9573–9580. DOI: 10.1103/PhysRevB.59.9573.

[123] D. A. Bonn et al. "Evidence for rapid suppression of quasiparticle scattering below T_c in $YBa_2Cu_3O_{7-\delta}$". In: *Phys. Rev. Lett.* 68 (1992), pp. 2390–2393. DOI: 10.1103/PhysRevLett.68.2390.

[124] N. Newman et al. "Double gun off-axis sputtering of large area $YBa_2Cu_3O_{7-\delta}$ superconducting films for microwave applications". In: *IEEE Transactions on Magnetics* 27 (1991), pp. 1276–1279. DOI: 10.1109/20.133417.

[125] D. A. Bonn et al. "Microwave surface impedance as a probe of unconventional superconductivity in $YBa_2Cu_3O_{6.95}$". In: *Journal of Physics and Chemistry of Solids* 54 (1993). Special Issue Spectroscopies in Novel Superconductors, pp. 1297–1305. DOI: 10.1016/0022-3697(93)90183-R.

[126] D. R. Lide, ed. *CRC Handbook of Chemistry and Physics.* CRC Press, Boca Raton, FL, 2005.

[127] P. Dhakal et al. “Effect of low temperature baking in nitrogen on the performance of a niobium superconducting radio frequency cavity”. In: *Phys. Rev. Accel. Beams* 21 (2018), p. 032001. DOI: 10.1103/PhysRevAccelBeams.21.032001.

[128] P. Bosland et al. “NbTiN Superconducting Thin Films Prepared by Magnetron Sputtering”. In: *Proc. of the 5th Workshop on RF Superconductivity (SRF'91), DESY, Hamburg, Germany*. 1991, pp. 497–508. URL: http://accelconf.web.cern.ch/AccelConf/SRF91/papers/srf91e13.pdf.

[129] A.-M. Valente-Feliciano et al. “NbTiN based SIS Multilayer Structures for SRF Applications”. In: *Proc. of the 16th International Conference on RF Superconductivity (SRF'13), Paris, France*. 2013, pp. 670–673. URL: http://accelconf.web.cern.ch/AccelConf/SRF2013/papers/tup088.pdf.

[130] A.-M. Valente-Feliciano et al. “Growth and Characterization of Multilayer NbTiN Films”. In: *Proc. of the 17th International Conference on RF Superconductivity (SRF'15), Whistler, BC, Canada*. 2015, pp. 516–520. DOI: 10.18429/JACoW-SRF2015-TUBA08.

[131] S. N. Simrock. “Lorentz Force Compensation of Pulsed SRF Cavities”. In: *Proc. of the 21st Linear Accelerator Conference (LINAC'02), Gyeongju, Korea*. 2002, pp. 554–558. URL: http://accelconf.web.cern.ch/AccelConf/l02/papers/WE204.pdf.

Acknowledgements

This last page of my thesis is dedicated to acknowledge the enormous support I received during the last years and without which this thesis would not have been possible.

In the first place, I would like to thank my advisor Jens Knobloch for giving me the opportunity to carry out this thesis and for his support and guidance. A big thank you also to my second referee Ursula van Rienen.

I extend my thanks to my supervisor Oliver Kugeler for always having an open door, useful ideas and help. Thank you to Raphael Kleindienst for his spadework prior to and during commissioning of the quadrupole resonator. That brought me into the comfortable position that sample tests were possible right from the beginning of my thesis work. I extend my thanks to the other physicists of the SRF group, in particular Julia Köszegi and Axel Neumann, for helpful discussions and support.

This work heavily relied on collaborations to other labs. I am very grateful to Anne-Marie Valente-Feliciano for preparation of the multilayer sample, SEM analysis of the Nb_3Sn sample and many hours of video conferences. I extend my thanks to Ari Palczewski and Charlie Reece for sample production and helpful discussions. I would like to thank Daniel Hall, Matthias Liepe and Ryan Porter for Nb_3Sn sample preparation and coating.
Sarah Aull and Tobias Junginger provided many information about the CERN QPR, helped me understanding this special cavity and carrying out measurements, thank you for that.

Not one single test would have been possible without the support of our cryogenic group – Svenja Heling, Axel Hellwig, Karsten Janke and Stefan Rotterdam. I am also grateful for the engineering support concerning readout electronics, cabling, vacuum pumps and cleanroom work, especially by Sascha Klauke, Michael Schuster and Jan Ullrich.
I extend my thanks to all (former) office mates for help with data analysis, for lots of fruitful discussions and for an always very pleasant working environment – namely Eva Panofski, Martin Schmeißer, Dmitry Tikhonov and Jens Völker.

On a more personal level, a huge thank you to my family – especially to my parents Hildegard and Eberhard and to my wife Pia – for their support and encouragement through the years.

Thank you!